JAGIELLONIAN UNIVERSITY
IN KRAKOW

BACKGROUNDS IN THE GERDA AND DARKSIDE EXPERIMENTS

RADIOACTIVE IONS IN CRYOGENIC LIQUIDS

A DOCTORAL DISSERTATION BY

KRZYSZTOF PELCZAR

M. Smoluchowski Institute of Physics
Faculty of Physics, Astronomy and Applied Computer Science
Jagiellonian University Kraków
Poland

2015

Academic Advisor

Prof. dr hab. Marcin Wójcik
M. Smoluchowski Institute of Physics, Jagiellonian University Kraków, Poland

Secondary Academic Advisor

Dr Grzegorz Zuzel
M. Smoluchowski Institute of Physics, Jagiellonian University Kraków, Poland

Assessment committee

Prof. dr hab. Ewa Rondio
National Centre for Nuclear Research, Świerk, Poland

Prof. dr hab. Jerzy Mietelski
Institute of Nuclear Physics, Kraków, Poland

Contents

Preface

A central problem discussed in this thesis is the importance of the internal radioactive background sources for the ultra–sensitive experiments, searching for rare interactions at low energies, such as GERDA [1] and DARKSIDE [2]. The front–end neutrino and dark matter physics probed in these experiments, respectively, requires full understanding of processes accompanying the detection. One of the most challenging tasks is the characterization of the background sources in the active volume of a detector. An exact background model is fundamental to the interpretation of the experimental results, which are of great importance to science.

Cryogenic liquids, often used either as passive and active shields, or as the detector medium, have to be purified in order to achieve the expected detection sensitivities in these types of experiments. However, the remaining traces of radioactivity present a possible source of internal background, that has to be understood and further mitigated. The goal of this thesis is therefore to investigate the physical properties of ^{222}Rn and ^{42}Ar progenies in liquid nitrogen and argon, identified as possible sources of the background. Due to the presence of electric potentials in the active volumes of detectors (e.g. generated by the high voltage bias of germanium detectors or liquid argon time projection chambers), the research focuses on the charged states of ^{222}Rn and ^{42}Ar progenies.

The questions addressed in the thesis are:

- What is the probability of an ion being created? If the fraction of ions created in nuclear decays is negligible, then the problem of cations drifting in the electric fields is negligible, as the electric field would be unable to pre–concentrate the neutral atoms.
- What is the ionic life–time (and range) of ions in clean environments? How deeply the ions can penetrate the active volume of a detector, when drifted in ubiquitous electric fields? The question is of the utmost importance as the high–purity gases (by definition) are depleted with neutralizing agents (oxygen, nitrogen oxides, carbon dioxide etc.), thus the expected life–times are rather significant.
- What is the sign of a charged atom? I.e. what would be the efficiency of ion sweepers, if used? A possible (one would say obvious) way to deal with the radioactive ions is to redesign the experiment such as to reverse the polarity of the electric fields used. But if the ions are also formed as molecules of the opposite charge, then such an approach may be futile for experiments aiming at extremely low background indexes.

Thesis outline

The first chapter briefly describes the field of the physics focusing on the quest for neutrinoless double beta ($0\nu\beta\beta$) decay and dark matter searches. The ultra–low background experiments GERDA and DARKSIDE are presented. Basic information, characterising ions in liquids, is also provided. The second chapter focuses on the physics of the ^{222}Rn–chain radioactive ions, presenting techniques, methodology and measurement results conducted in a dedicated setup, filled with liquid nitrogen. The third chapter is devoted to the physics of ^{42}K (^{42}Ar daughter) ions in liquid argon, studied in the LArGe detector [3] (in the framework of the GERDA experiment). Interestingly, both families of the radioactive ions exhibited a similar behaviour of increasing yield (measured signal) over long periods of time. This feature of the ions in ultra–pure cryogenic liquids was studied in detail for ^{42}K. A general model of the ions, derived in that chapter, was then used for the interpretation of the experimental data from ^{42}K background measurements in GERDA. The computational framework, created and applied to the modelling of the ions in liquid argon and nitrogen, was also used to design a new online electrostatic radon monitor, described in the last chapter of the thesis. As a result, improved detection efficiency (up to 72 %), versatility (in types of examined gases) and simplified construction (low noise electronics, spurious signal vetoing, significantly lower high voltage bias) were achieved with respect to the previous designs. The radon monitor is currently used for ^{222}Rn background assessment in the DARKSIDE experiment, a liquid argon detector searching for interactions of dark matter in the form of Weakly Interacting Massive Particles (WIMPs).

Acknowledgements

First of all I would like to thank my supervisor, Prof. dr hab. Marcin Wójcik for taking me on a PhD. His advice, immense patience and positive attitude were always very encouraging. He provided me with an exceptional opportunity to develop my skills and knowledge in an unbound fashion. I would also like to thank Dr Grzegorz Zuzel for his insightful opinions, great ideas and plenty of time spent on tutoring me while working together on several interesting projects. Their help and assistance is inestimable, for their efforts I am deeply grateful.

I would like to thank all my friends and co–workers at Jagiellonian University, especially Eng. Marek Adamczyk for teaching me electronics (and patience), and Elżbieta Kotula for her instant and irreplaceable support.

I am also thankful for the continuous support provided by my beloved parents Sylwia and Michał, and my dear brother Grzegorz.

But without my wife Anna nothing would be possible – thank you so much!

I acknowledge the financial support by the MPD programme of Foundation for Polish Science through structural funds of the European Union.

I also acknowledge the financial support by the National Science Centre, grant No. UMO–2012/05/E/ST2/02333.

Dedicated to my loving family.

1

Searches for rare events at low energies

The reason why W. Pauli proposed a new particle in a letter sent to a group of physicists meeting in Tübingen in December 1930 is well known. Furthermore, he even expressed curiosity about a faint chance to register the new particle experimentally[i]. The history of experimental searches has proven neutrinos to be one of the most difficult particles to observe. The weak force neutrinos interact through is the true source of slowly accelerating progress in neutrino physics. The Savannah–River experiment [4] successfully showed the existence of electron antineutrinos through the inverse beta decay $p(\nu, e^+)n$ reaction in 1956, over two decades after W. Pauli proposed the solution to the problem of the observed continuous β–decay energy spectra.

Year 1957 brought a new discovery, made by C. Wu et al. [5], showing that weak interactions violate parity conservation law. Published a year after, was a discovery made by M. Goldhaber et al. [6] determining neutrino's helicity. As a final result it was shown that in general leptons (by convention) are left–handed, and antileptons are right–handed.

In the first experiment with an accelerator generated neutrino beam, it was shown in 1962 [7] (in the Brookhaven National Laboratory), that muons, like electrons, have their partner neutrinos ν_μ. The next flavour of neutrinos was therefore discovered. The search was suggested by the lack of observation of the muon decays into electrons and gammas. As a consequence, a new lepton number conservation law followed, distinguishing electron– and muon–like leptons (i.e. $e - \nu_e$ and $\mu - \nu_\mu$). The existence of the third, tau neutrino ν_τ, was confirmed experimentally by the DONUT collaboration, in 2001 [8]. Measurements of the cross section for the production of a Z^0 boson suggested, that in total 3 flavours of light neutrinos exist ($N_\nu = 2.984 \pm 0.008$ [9]). If more neutrinos exist, they must be heavier than a half of a Z^0 boson.

Parallel to the experimental discoveries, a theoretical model of interactions combining weak and electromagnetic forces was formulated. In the following years S. Glashow [10], A. Salam [11] and S. Weinberg [12] developed a new framework describing electric and weak forces as combined together into the one electro–weak interaction. Using the new theory it was possible to predict the existence of a neutral component to the weak interaction, confirmed experimentally in 1973 by the Gargamelle group [13], by observation of antineutrinos scattering on electrons: $\bar{\nu}_e + e^- \rightarrow \bar{\nu}_e + e^-$. The neutrino weak interactions are mediated in the model by two bosons: the charged $W^{+/-}$ and the neutral Z^0. Also, neutrinos were assumed to be massless particles.

Soon after the birth of Glashow–Salam–Weinberg model, R. Davies in his experiment conducted in the Homestake mine [14] (the 'Chlorine' experiment), showed the deficit in the measured flux of ν_e neutrinos from the Sun, coming from the ^{8}B production. The detection technique was based on counting decays of ^{37}Ar, extracted from the solution where it was produced in the $\nu_e + {}^{37}Cl \rightarrow e^- + {}^{37}Ar$ reaction. Less than half of the expected flux was observed. Other measurements followed and continued for over twenty years, confirming only the primary result. One third to one half of the predicted number of electron neutrinos were detected, in different ν_e energy regions (Kamiokande [15], SAGE [16] and GALLEX [17]). If neutrinos were massless, their type (flavour) should remain fixed when they were produced in the Sun. The resolution to the problem was proposed as the effect of neutrino flavour oscillation. However, this explanation would require neutrinos to be massive particles.

[i] *"Ich traue mich vorläufig aber nicht, etwas über diese Idee zu publizieren, und wende mich erst vertrauensvoll an Euch, liebe Radioaktive, mit der Frage, wie es um den experimentellen Nachweis eines solchen Neutrons stände, wenn dieses ebensolches oder etwas 10mal größeres Durchdringungsvermögen besitzen würde wie ein γ–Strahl."*

Three of the four fundamental forces are well–described by the Standard Model, showing that our understanding of physics is almost complete. Nevertheless there exist a number of open questions, especially in the non–accelerator physics, which are still pending a comprehensive explanation. One of the most active fields of interests spans neutrino and dark–matter physics. The two interests of modern physics are closely related with each other in the experimental manner, as in both cases scientists are searching for very rare processes occurring at low energies.

1.1 Neutrino Physics

Due to the fact that neutrinos oscillate, we know that they are massive particles [18]. Flavour states of neutrinos $\nu_{e,\,\mu,\,\tau}$ are not identical with mass eigenstates $\nu_{1,\,2,\,3}$ (with the corresponding mass eigenvalues m_i). They are related to each other through the unitary Pontecorvo–Maki–Nakagawa–Sakata (PMNS) matrix U. The matrix may be parametrized by three mixing angles θ_{12}, θ_{13}, θ_{23} and three CP–violating phases δ, α and β:

$$U = \begin{pmatrix} c_{12}c_{13} & s_{12}c_{13} & s_{13}\mathrm{e}^{-i\delta} \\ -s_{12}c_{23} - c_{12}s_{23}s_{13}\mathrm{e}^{i\delta} & c_{12}c_{23} - s_{12}s_{23}s_{13}\mathrm{e}^{i\delta} & s_{23}c_{13} \\ s_{12}s_{23} - c_{12}c_{23}s_{13}\mathrm{e}^{i\delta} & -c_{12}s_{23} - s_{12}c_{23}s_{13}\mathrm{e}^{i\delta} & c_{23}c_{13} \end{pmatrix} \times \mathrm{diag}\left(1,\, \mathrm{e}^{i\alpha},\, \mathrm{e}^{i\beta+i\delta}\right) \tag{1.1}$$

where $s_{ij} = \sin(\theta_{ij})$, $c_{ij} = \cos(\theta_{ij})$, and δ is the Dirac phase responsible for CP violation in neutrino oscillation experiments. The two Majorana phases, α and β, are relevant only if neutrinos are Majorana particles. Tab. 1.1 summarizes measured parameters of the U matrix. Neutrino interactions with charged leptons are always mediated by a charged weak boson W, e.g.:

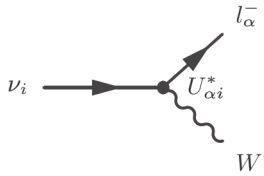

The probability of creating a neutrino mass eigenstate ν_i, corresponding to a lepton l_α of α flavour, is given by the PMNS matrix element $|U_{\alpha i}|^2$. Linear combination of the mass eigenstates yields a neutrino flavour state:

$$|\nu_\alpha\rangle = \sum_i U^*_{\alpha i} |\nu_i\rangle \tag{1.2}$$

Flavour neutrinos are created in a given state α and are registered as a superposition of mass eigenstates. Due to the differences in the masses, propagation of different mass eigenstates varies with energy. After passing a distance L, each mass state exhibits different phase $\Phi_i = m_i^2 \frac{L}{2E}$. Offsets in phases result in the effect of neutrino flavour oscillations. The final (registered) state β is also a superposition of mass eigenstates, thus probability of β state registration is:

$$P\left(\nu_\alpha \to \nu_\beta\right) = \sum_i U^*_{\alpha i} \mathrm{e}^{-i m_i^2 \frac{L}{2E}} U_{\beta i} \tag{1.3}$$

Experiments observing the neutrino flavour oscillations yield only differences in the phases, thus only the differences between the masses squared are known. What is not known, is therefore the hierarchy of neutrino masses and CP violation parameters. It is also possible, that mechanism responsible for the creation of neutrino masses differs from leptons (Dirac), i.e. neutrinos may be Majorana particles, being their own antiparticles. Consequently, lepton number conservation rule could be broken, allowing e.g. to explain the discrepancy in the observed amount of matter and antimatter.

Recent results from reactor experiments [20] have shown that all the mixing angles are different from zero, making the search for CP violation in the leptonic sector possible [21]. There are, however, very important

Parameter	Best fit ± 1σ	2σ range	3σ range
Δm^2_{21} [10^{-5}eV^2]	$7.60^{+0.19}_{-0.18}$	7.26–7.99	7.11–8.18
$\lvert\Delta m^2_{31}\rvert$ [10^{-3}eV^2] (NH)	$2.48^{+0.05}_{-0.07}$	2.35–2.59	2.30–2.65
$\lvert\Delta m^2_{31}\rvert$ [10^{-3}eV^2] (IH)	$2.38^{+0.05}_{-0.06}$	2.26–2.48	2.20-2.54
$\sin^2\theta_{12}/10^{-1}$	3.23±0.16	2.92–3.57	2.78–3.75
$\theta_{12}/^\circ$	34.6±1.0	32.7–36.7	31.8–37.8
$\sin^2\theta_{23}/10^{-1}$ (NH)	$5.67^{+0.32}_{-1.24}$	4.14–6.23	3.93–6.43
$\theta_{23}/^\circ$	$48.9^{+1.8}_{-7.2}$	40.0–52.1	38.8–53.3
$\sin^2\theta_{23}/10^{-1}$ (IH)	$5.73^{+0.25}_{-0.39}$	4.35–6.21	4.03–6.40
$\theta_{23}/^\circ$	$49.2^{+1.5}_{-2.3}$	41.3–52.0	39.4–53.1
$\sin^2\theta_{13}/10^{-2}$ (NH)	2.26±0.12	2.02–2.50	1.90–2.62
$\theta_{13}/^\circ$	$8.6^{+0.3}_{-0.2}$	8.2–9.1	7.9–9.3
$\sin^2\theta_{13}/10^{-2}$ (IH)	2.29±0.12	2.05–2.52	1.93–2.65
$\theta_{13}/^\circ$	8.7± 0.2	8.2–9.1	8.0–9.4
δ/π (NH)	$1.41^{+0.55}_{-0.40}$	0.0–2.0	0.0–2.0
$\delta/^\circ$	254^{+99}_{-72}	0–360	0–360
δ/π (IH)	1.48±0.31	0.00–0.09 & 0.86–2.0	0.0–2.0
$\delta/^\circ$	266±56	0–16 & 155–360	0–360

Table 1.1: Neutrino oscillation parameters summary from the global analysis; values taken from [19]. IH stands for inverted hierarchy, $m_1 \simeq m_2 \gg m_3$, and NH – normal hierarchy, $m_3 \gg m_2 \gg m_1$.

neutrino properties, which are still to be clarified: the nature of neutrino (Dirac or Majorana particle) [22], the absolute scale of its mass [23] and the oscillations with a mass difference of the order of 1 eV (possible oscillations to sterile neutrinos) [24]. One possible way to solve the first two issues is to investigate the neutrinoless double beta ($0\nu\beta\beta$) decay. Neutrinoless double beta decay experiments are well recognized as the most powerful tool not only to probe the Majorana nature of the neutrino (verification of lepton number conservation [25]) and its mass, but also to investigate the neutrino mass hierarchy [26]. If positively verified, observation of the $0\nu\beta\beta$ decay would require physics beyond the Standard Model and, as the only one process, it would allow to experimentally probe neutrino masses down to the meV level.

Double beta decay ($2\nu\beta\beta$) is an extremely rare process occurring in the even–even nuclei. Such a transition is possible when a single β–decay is highly prohibited (e.g. due to the energy conservation law). In consequence, the atomic number A is conserved, but the proton number Z alters by ± 2[ii], i.e. for double β^- decay:

$$(A,\, Z) \rightarrow (A,\, Z+2) + 2e^- + 2\bar{\nu}_e \tag{1.4}$$

Fig. 1.1 shows the energy diagram for ^{76}Ge, ^{76}As and ^{76}Se. Decays with emission of two neutrinos were observed for several isotopes, as it is summarized in Tab. 1.2.

Decays non–preserving the lepton number, thus non foreseen by the Standard Model, are also considered. One of the decay modes is the neutrinoless double beta decay, where two electrons are not accompanied by respective anti–neutrinos:

$$(A,\, Z) \rightarrow (A,\, Z+2) + 2e^- \tag{1.5}$$

If neutrinos are Majorana particles, then the virtual Majorana neutrino ν_{ee} created in the W^- decay could annihilate with its counterpart. Observation of such a neutrinoless process (with a specific half–life $T^{0\nu}_{1/2}$) is

[ii] Other decay processes are also possible, i.e. $2\beta^-$, $2\beta^+$ and electron capture 2ε decays.

Nuclide	Process	$T_{1/2}^{2\nu}$ y	$T_{1/2}^{0\nu+2\nu}$ y
^{48}Ca	$2\beta^-$	$4.39 \pm 0.58 \times 10^{19}$	
^{76}Ge	$2\beta^-$	$1.43 \pm 0.53 \times 10^{21}$	
^{82}Se	$2\beta^-$	$9.19 \pm 0.76 \times 10^{19}$	
^{96}Zr	$2\beta^-$	$2.16 \pm 0.26 \times 10^{19}$	
^{100}Mo	$2\beta^-$	$6.98 \pm 0.44 \times 10^{18}$	
^{100}Mo	$2\beta^-$	$5.70 \pm 1.36 \times 10^{20}$	
^{100}Mo	$2\beta^-$		$6.12 \pm 0.20 \times 10^{20}$
^{116}Cd	$2\beta^-$	$2.89 \pm 0.25 \times 10^{19}$	
^{128}Te	$2\beta^-$		$3.49 \pm 1.99 \times 10^{24}$
^{130}Te	$2\beta^-$	$7.14 \pm 1.04 \times 10^{20}$	
^{136}Xe	$2\beta^-$	$2.34 \pm 0.13 \times 10^{21}$	
^{130}Ba	2ε		$1.40 \pm 0.80 \times 10^{21}$
^{150}Nd	$2\beta^-$	$8.37 \pm 0.45 \times 10^{18}$	
^{150}Nd	$2\beta^-$		$1.33 \pm 0.40 \times 10^{20}$
^{238}U	$2\beta^-$		$2.00 \pm 0.60 \times 10^{21}$

Table 1.2: Double beta decay (or double electron capture) half–lives for several even–even isotopes. The half–life data for the combined $0\nu + 2\nu$ decay mode comes mainly from the geochemical measurements. Data taken from [27].

related to the effective mass of the Majorana neutrino m_{ee}:

$$\left[T_{1/2}^{0\nu}\right]^{-1} - G_{0\nu}(Q, Z)|M_{0\nu}|^2|m_{ee}|^2 \tag{1.6}$$

where $G_{0\nu}(Q, Z)$ is the kinematic factor (depending on the decay heat Q), $M_{0\nu}$ is the matrix element of the decay, and the Majorana effective mass is defined as:

$$m_{ee} = \sum_i U_{ei}^2 m_i \tag{1.7}$$

Consequently, by measuring the half–life of the $0\nu\beta\beta$ decay (or setting a limit), it is possible to tackle the problem of neutrino mass hierarchy (see Fig. 1.2).

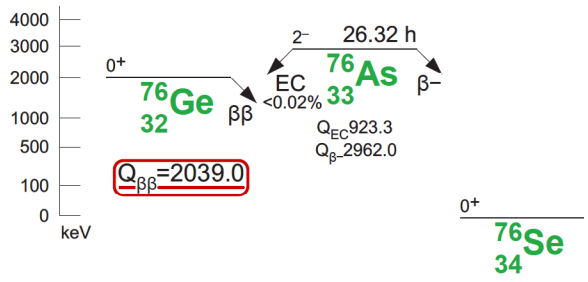

Figure 1.1: Double beta decay in ^{76}Ge. Beta decay to ^{76}As is energetically forbidden, while $2\nu\beta\beta$ decay to ^{76}Se is not.

Among the potential double beta emitters, Ge shows very good characteristics and up to date the best officially published limit for the half–life of the $0\nu\beta\beta$ process comes from the Ge–based GERDA experiment: $T_{1/2} > 2.1 \times 10^{25}$ y [28][iii]. This result can be further improved by considering combined analysis of the data available from the GERDA, Heidelberg–Moscow [29] and IGEX [30] experiments: $T_{1/2} > 3 \times 10^{25}$ y, corresponding to a limit on the effective Majorana neutrino mass of 0.2 eV to 0.4 eV [28]. The next generation projects (like GERDA Phase II) need to push the limit for the $0\nu\beta\beta$ decay half–life into the range of 10^{26} – 10^{27} y. This goal can be reached by increasing the target masses along with simultaneous reduction of background by another one–to–two orders of magnitude at $Q_{\beta\beta}$, while preserving high energy resolution.

Several experiments searching for the $0\nu\beta\beta$ decay have been performed in the past, going back for at least half a century with increasing sensitivities. Many candidate isotopes were/are being considered in experimental and R&D programs, notably ^{76}Ge, ^{130}Te, ^{136}Xe, ^{82}Se, ^{150}Nd, ^{100}Mo, ^{48}Ca and ^{116}Cd. These

[iii] From now on, $T_{1/2}$ denotes the $0\nu\beta\beta$ decay half life.

nuclei are characterized by their own $Q_{\beta\beta}$–values and nuclear matrix elements. It has been shown [31–33] that the phase–space and the NME effects nearly compensate, so that the specific decay rates are the same within a factor of two for all candidates listed above. In particular, an effective neutrino mass of a few tens of meV would yield a decay rate of approximately $1\,\mathrm{cts\,t^{-1}\,y^{-1}}$ for all isotopes.

The two most sensitive past experiments, which used ^{76}Ge were Heidelberg–Moscow (HdM) [35] and the International Germanium Experiment (IGEX) [30]. There was no evidence for the peak at $Q_{\beta\beta}$ (signature of the $0\nu\beta\beta$ decay) and set lower limits on the half–life of $T_{1/2} > 1.9 \times 10^{25}$ y and $T_{1/2} > 1.6 \times 10^{25}$ y at 90 % C.L., respectively. A part of the HdM collaboration published a claim about positive observation (with significance of 4.2σ) of the $0\nu\beta\beta$ decay and reported $T_{1/2} = (1.19^{+0.37}_{-0.23}) \times 10^{25}$ y [29]. Later, by applying a pulse shape discrimination (PSD) analysis, the claim was strengthened to about 6σ [36], but due to some inconsistencies in the analysis pointed out in [31], the comparison of the GERDA result is restricted (by the GERDA collaboration) to the result reported in [29].

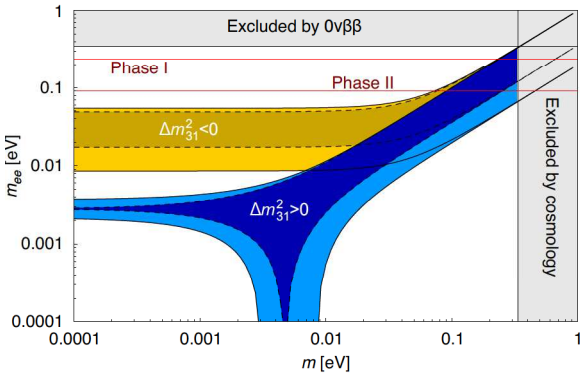

Figure 1.2: GERDA experimental limits (the two phases of the experiment) imposed on the diagram of neutrino mass hierarchy, assuming $U_{e3} = 0$ [34]. m – the lightest neutrino mass.

The most important and presently running $0\nu\beta\beta$ decay experiments are: GERDA, KamLAND–Zen, EXO–200, CUORE–0 (CUORE), CANDLES III, and Majorana Demonstrator. Under preparation or during commissioning are e.g. CUORE, SNO+, SuperNEMO. The status and the results obtained so far by GERDA will be discussed later.

The KamLAND–Zen experiment is based on a modification of the existing KamLAND detector [37] carried out in 2011. Its core is 13 tons of Xe–loaded liquid scintillator contained inside a spherical inner balloon (3.08 m diameter). The isotopic abundance of the enriched xenon has been measured to be about 90.9 % of ^{136}Xe and 8.9 % of ^{134}Xe. The limit for $T_{1/2}(0\nu\beta\beta)$ achieved so far in the experiment is $T_{1/2} > 1.9 \times 10^{25}$ y (90 % C.L.) [38]. After purification of the scintillator the level of radioactive impurities was reduced and a new data–taking phase started at the end of 2013. Preliminary analysis of both data sets improved the $0\nu\beta\beta$ limit to $T_{1/2} > 2.6 \times 10^{25}$ y (90 % C.L.) [39]. The second phase will end in fall 2015, and the next phase will start in 2016 with sensitivity goal of 2×10^{26} y after a 2–year exposure [40].

The EXO–200 experiment is built around a large liquid xenon Time Projection Chamber filled with ∼200 kg of liquid xenon enriched to about 80.6 % in ^{136}Xe. In June 2012 the collaboration reported the first results on the $0\nu\beta\beta$ decay, analysing the exposure of 32.5 kg y: $T_{1/2} > 1.6 \times 10^{25}$ y (90 % C.L.) [41]. The measurement has been updated with a higher exposure (100 kg y). No statistically significant evidence for the $0\nu\beta\beta$ decay has been found, and the obtained half–life limit is $T_{1/2} > 1.1 \times 10^{25}$ y (90 % C.L.) [42].

Assembly of CUORE–0, based on ^{130}Te, is the first step of CUORE as the proof of concept. It is operated since March 2013, and achieved its energy resolution and background level objectives (the energy resolution of the 2615 keV ^{208}Tl γ–line is 4.9 keV). The CUORE–0 background measured from the initial 9.8 kg y exposure is $0.06\,\mathrm{cts\,keV^{-1}\,kg^{-1}\,y^{-1}}$ [43]. Combination of the CUORE–0 result with the existing 19.75 kg y of ^{130}Te exposure from Cuoricino yields limit on $T_{1/2} > 4 \times 10^{24}$ y (90 % C.L.). CUORE will deploy 988 crystals of TeO_2 (741 kg in total, 206 kg of ^{130}Te), arranged in a large array made of 19 *towers*. Assembly of the 19 CUORE towers was completed, and the completion of the cryogenic system commissioning will be followed by the detector installation [44]. The full operation is expected early in 2016. The sensitivity of the full–scale experiment after 5 y of data taking and with a background index of $0.01\,\mathrm{cts\,keV^{-1}\,kg^{-1}\,y^{-1}}$ is about 10^{26} y (90 % C.L.) [45].

CANDLES is a project which aims to look for the $0\nu\beta\beta$ decay of ^{48}Ca by using CaF_2 detectors. The CANDLES III experiment has been taking data since Spring 2013 at the Kamioka underground laboratory in Japan. It is operating 96 CaF_2 detectors (305 kg of total mass, natural ^{48}Ca abundance) immersed in

liquid scintillator [46]. The CANDLES III setup was scheduled to take data in 2014 and 2015, before the transition to the next upgrades (CANDLES IV/V) with detectors enriched in ^{48}Ca will be deployed.

SNO+ is based on the SNO neutrino experiment [47] at SNOLAB. The candidate $0\nu\beta\beta$ isotope is ^{130}Te, which will be deployed in the detector in the form of 0.3 % loading of the liquid scintillator. The total mass of ^{130}Te in the fiducial volume would be 800 kg. The SNO+ collaboration is to fill the SNO detector with liquid scintillator by the end of 2016. Pure scintillator commissioning phase is scheduled for the beginning of 2017, followed by the tellurium–loaded phase.

The Majorana Demonstrator (MJD) project is operating large modular arrays of HPGe detectors for the search of the $0\nu\beta\beta$ decay of ^{76}Ge [48]. The setup is located underground at the 1480 m level of the SURF Laboratory in the USA. The first step of the commissioning was performed in 2013 with a prototype vacuum cryostat. Commissioning of the Module 1 completed in July 2015 with 23 out of 29 detectors operating (16.8 kg of ^{enr}Ge in form of 20 detectors and 5.7 kg of ^{nat}Ge – 7 detectors). From assays, the background budget is projected to be less than 0.88 cts keV^{-1} t^{-1} y^{-1} (goal of 0.75 cts keV^{-1} t^{-1} y^{-1}). Start of the operations was planned for 2015 after completion of fabrication and assembly of Module 2 [49].

The SuperNEMO project [50] is based on the same design and technology as NEMO3 [51]. The goal is to deploy up to 100 kg of target isotope within 20 identical modules at the Modane underground Laboratory in France. ^{82}Se is the primary choice as the target but ^{150}Nd and ^{48}Ca are also considered, depending on the development of viable enrichment procedures. The SuperNEMO collaboration will firstly operate one module (7 kg of ^{82}Se) as a demonstrator, which is presently under construction (25 % of the source foil produced for the demonstrator). Commissioning of the detector is scheduled at the end of 2016.

A detailed review of the experimental situation in the field of $0\nu\beta\beta$ searches, including not discussed here future project like nEXO, NEXT or MAGIC can be found e.g. in [52–54].

1.2 The GERDA Experiment

The GERmanium Detector Array, GERDA [1], was designed to search for neutrinoless double beta decay of ^{76}Ge. The importance of such a search is emphasized by the evidence of a non–zero neutrino mass from flavour oscillations and by the claim [29], based on the data of the Heidelberg–Moscow experiment. The experiment was designed to check this claim in the first Phase, ended in 2013. GERDA is installed in Hall A of the Gran Sasso National Laboratory (LNGS) of INFN, Italy. In the second Phase, being currently prepared, an exposure of about 100 kg y is expected, with a requirement of the background index of the order of 10^{-3} cts keV^{-1} kg^{-1} y^{-1} at the $Q_{\beta\beta}$–value of 2039 keV. Due to numerous technical and practical aspects the search for $0\nu\beta\beta$ decay in ^{76}Ge is carried out by using germanium as both a source and a detector for the decays. The energy resolution (0.2 % at $Q_{\beta\beta}$), high intrinsic purity of the Ge crystals, scalability, cost, and well established and studied technology are the main advantages of the high purity germanium–based approach.

In the Gerda setup, high purity detectors (HPGe) made out of isotopically enriched germanium ($^{\text{enr}}$Ge) are operated bare inside a cryogenic bath (Fig. 1.3). In the original proposal, it was foreseen to use liquid nitrogen (LN_2), but due to the higher density (better passive shielding properties) of liquid argon (LAr), and its scintillation abilities, LAr was finally selected as the coolant, passive (Phase I) and active (Phase II) shield. A novel concept of a combination of shields was chosen for cost and space reasons. The large volume cryostat (65 m^3, 4.2 m diameter), internally lined with copper, is contained in the container (10 m diameter) filled with high–purity water. The cryostat is vacuum insulated, and equipped with an active cooling system to avoid LAr losses. The water tank serves also as a neutron shield and an active Cherenkov muon veto (the water tank is instrumented with 66 PMTs). A muon veto system (plastic scintillator) shielding the neck region of the cryostat is placed on top of the water tank.

Access to the cryostat volume is possible through a lock system. The lock allows to deploy, manipulate or assemble the detectors. All procedures are carried out in a glove box, in dry nitrogen atmosphere. The detectors are organized in closely spaced strings, maximizing the background rejection by anti–coincidence between the detectors. The strings form a detector array, suspended from the top of the cryostat on a twin lock system. The lock system is located on top of the water tank, in a clean room. All applied joints and valves are metal sealed; with a slight overpressure radon leakage from the atmosphere into the cryostat is mitigated. The cryostat was primarily designed to be made of low radioactivity copper (<20 µBq kg^{-1} of ^{228}Th [55]). Due to the safety reasons and cost increase, the cryostat was manufactured out of stainless steel. It is internally lined with a shield, made out of 16 t of high purity oxygen free radiopure (OFRP) copper.

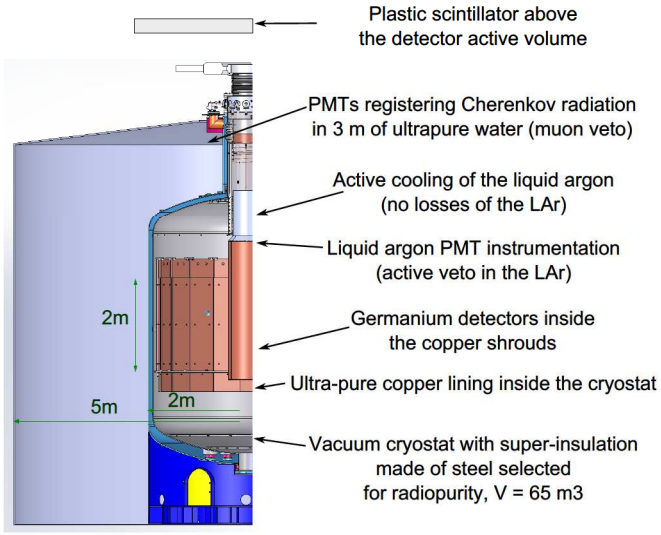

Figure 1.3: The multilayer design concept of the GERDA detector (Phase II). Passive and active shielding, with graded (increasing) material radio–purity towards the active volume of the detector is necessary to achieve the desired background index, by suppressing external and internal sources of background.

The main goal of the GERDA design was to minimize the amount of material close to the germanium crystals (e.g. crystal holders, cabling, electronics). Also, all components were selected for their radiopurity. In Phase I, the detectors were mounted in low–mass copper holders. They were deployed bare in the liquid argon, serving both as the cooling medium and the passive shield for the crystals against external radiation sources. In the second Phase of the experiment, the liquid argon was equipped with the scintillation light readout system. The scintillation signal associated with the background events is then used as an active veto. The main background sources at $Q_{\beta\beta}$ are ^{42}K, ^{214}Bi, ^{228}Th, ^{60}Co. Isotopes from the ^{226}Ra decay chain emitting alphas, are located close to the detectors [56].

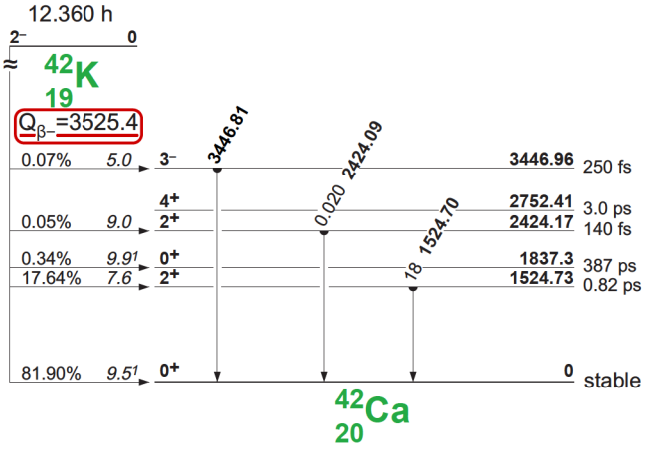

Figure 1.4: A simplified diagram of ^{42}K decay to ^{42}Ca. Highly energetic beta decay of ^{42}K ($Q_{\beta-}$ = 3525 keV) may be accompanied by a series of gammas with energies up to 3447 keV, well above the ^{76}Ge $Q_{\beta\beta}$ value. Both energy emission channels are important for the background index. The most prominent gamma line of 1525 keV is used to identify ^{42}K.

The use of liquid argon as the cryogenic liquid in the GERDA experiment resulted in an unexpected source of radioactive background. Contribution to the background due to the presence of naturally abundant ^{42}Ar isotope in natural argon, producing ^{42}K (Q_β of ^{42}K is above $Q_{\beta\beta}$, see Fig. 1.4), was assessed in the original proposal under the assumption of homogenic distribution of ^{42}Ar. Monte Carlo simulations yielded the background index to be less than 10^{-4} cts keV^{-1} kg^{-1} y^{-1}. Beta decays

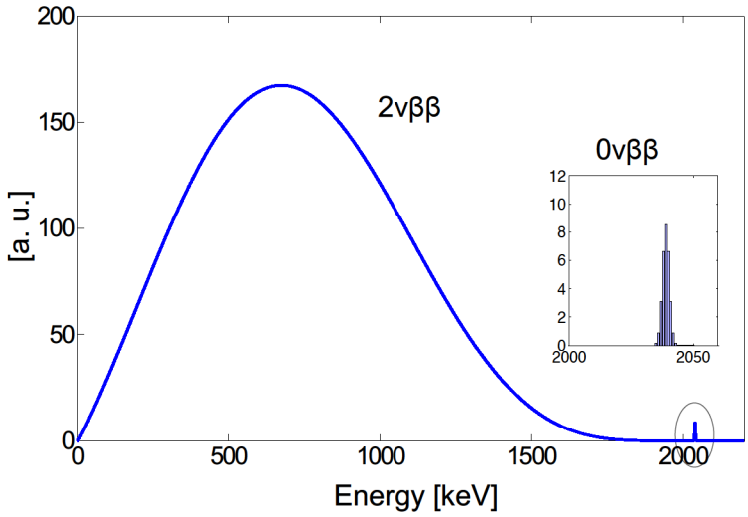

Figure 1.5: Energy spectrum of electrons emitted in $2\nu\beta\beta$ and $0\nu\beta\beta$ decays of ^{76}Ge, computed for 3 keV energy resolution at 2 MeV, assuming $T^{0\nu}_{1/2} = 1.2 \times 10^{25}$ y and $T^{2\nu}_{1/2} = 1.7 \times 10^{21}$ y [57].

of ^{39}Ar have a Q value of 0.6 MeV and do not contribute to the background for neutrinoless double beta decay. As such, the contribution from ^{42}Ar to the background was negligible. Also, simulations of the liquid argon scintillation veto showed factor 100 background reduction in the $Q_{\beta\beta}$ region, therefore ^{42}Ar was never considered as a major source of background for any phase of the GERDA experiment.

The assumption about homogeneous distribution of ^{42}Ar does not hold for ^{42}K ions however. Behaviour of the ions in pure cryogenic liquid, in the presence of the electric field produced by the high voltage bias (up to 5 kV) of the HPGe detectors, led to the altered spatial distribution of ^{42}K radioactivity.

1.2.1 Background problem in the $\beta\beta$ searches

The expected signal of $2\nu\beta\beta$ accompanied by $0\nu\beta\beta$ decays, as registered by a germanium detector, is shown in Fig. 1.5 in an idealized case of no background and the energy resolution of $\Delta E = 3$ keV. The difference in energy spectra shapes of $0\nu\beta\beta$ and $2\nu\beta\beta$ decays stems from the fact, that the full heat released in $0\nu\beta\beta$ decay may be registered in a detector at $Q_{\beta\beta}$, while in the case of $2\nu\beta\beta$ two neutrinos carry away some part of the energy undetected, hence the spectrum is continuous (similar in shape to a single β–decay case) up to $Q_{\beta\beta}$. Experimental signature of the $0\nu\beta\beta$ is therefore a sharp peak at $Q_{\beta\beta}$.

A Bayesian analysis applied to Monte Carlo event samples was used to determine the sensitivity of GERDA. Experimental spectra were simulated for different assumed background indexes of 10^{-2} cts kg^{-1} keV^{-1} y^{-1} – 10^{-4} cts kg^{-1} keV^{-1} y^{-1} and no background, respectively. Next, 90 % probability lower limit on the $T_{1/2}$ ($0\nu\beta\beta$) was evaluated as a function of exposures, assuming only background processes. Results of the calculations are shown in Fig. 1.6. The analysis assumed a prior probability for background only of 50 %, an uncertainty on the background rate of 50 %, and a flat probability for the number of signal events up to a maximum corresponding to $T_{1/2} = 5 \times 10^{24}$ y. For the setting of upper limits, spectra were simulated with background events only. The analysis of the resulting spectra assumed that double beta decay processes exist in addition to the background processes, and a 90 % upper limit on the possible number of signal events was evaluated.

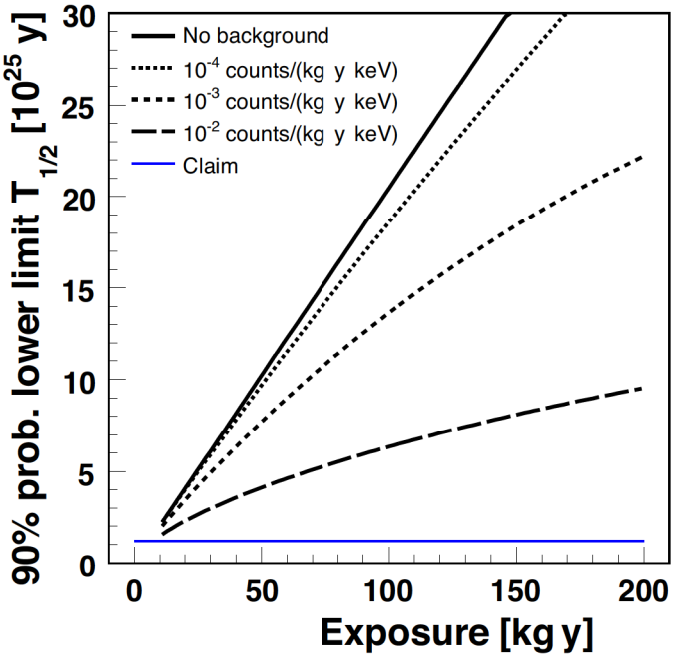

Figure 1.6: The plot shows the expected 90 % probability lower limit on the half life for neutrinoless double beta decay versus the exposure under different experimental background conditions. Also shown is the half–life for the claimed observation [29].

In reality, i.e. in the case of non–zero background index B, the sensitivity scales as:

$$T_{1/2} \propto \varepsilon a \sqrt{\frac{MT}{B\Delta E}} \tag{1.8}$$

where ε is the detection efficiency, a is the abundance of the isotope of interest, M is the total active mass observed in time T, and ΔE is the energy resolution. However, in the ideal case of no background ($MTB\Delta E \ll 1$), the sensitivity scales linearly with the exposure MT:

$$T_{1/2} \propto \varepsilon a MT \tag{1.9}$$

It is clearly seen from the plot shown in Fig. 1.6 and the above expressions, that in order to improve the detection limits by an order of magnitude in the case of no background, the exposure has to be increased by an order of magnitude as well. In turn, in the case of non–negligible background present, the improvement in sensitivity may be achieved by increasing the exposure by two orders of magnitude, or achieved by lowering the background index, or both. Increase in the exposure is limited by the available active mass and reasonable measurement time. Therefore the problem of the ultra–low background is emphasized, as it is possible to achieve nearly linear increase in sensitivity for extremely low background indexes. The limiting factor would be the background from $2\nu\beta\beta$ decay, which can be mitigated by improving the energy resolution of a detector.

1.3 The DarkSide Experiment

For over a century, astronomical observations and calculations based on models have been indicating, that more than 80 % of the mass of the Universe is dark, meaning that it is impossible to observe dark matter

with e.g. telescopes as it neither emits nor absorbs radiation on the detectable level. The presence of dark matter can only be ascertained indirectly by astronomical observations of the gravitational effects.

It is commonly believed that dark matter constituents are neutral and do not belong to the family of standard model particles. Some of the hypothetical candidate particles were already ruled out as possible dark matter particles (e.g. heavy neutrinos, $m_\nu \approx 17$ keV). Currently, the leading candidate for the dark matter particle, explaining elusive nature of dark matter, is a Weakly Interacting Massive (1 GeV – 1000 GeV) Particle, WIMP. WIMPs may have been formed in the early Universe, and then gravitationally clustered with the baryonic matter to form complex, large scale structures. Direct searches of WIMPs present a very challenging experimental task, based on the presumption about their weak interactions with matter.

Numerous astrophysical observations led to the conclusion, that masses of galaxies deduced from the gravitational interactions (dynamics) are inconsistent with the mass estimation based on the visible matter. Already in 1933 the term 'Dark Matter' was coined by F. Zwicky [58], who was observing rotational curves of galaxies.

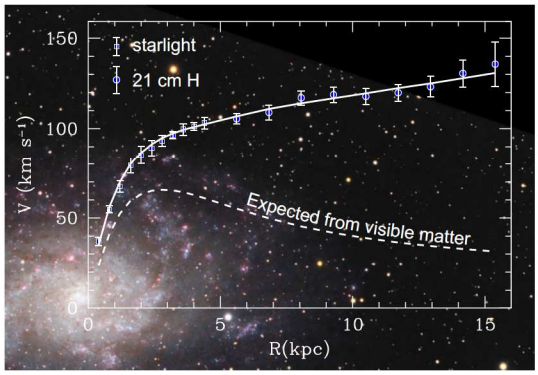

Figure 1.7: Messier 33 galaxy measured rotation curve (points) compared with the best fit model (continuous line). Also shown is the stellar disk contribution (dashed line). Data taken from [59].

Star and galaxy rotation curves Rotational velocity of a star depends on the distance from the galaxy centre. The velocity–radius relation is driven by the total mass contained within the specific radius. Inconsistency between the observed star velocity and the theoretical value (estimated from the observed mass) may be explained by the additional, invisible component of the galaxy mass. The first historical observations of the motions of stars in the Milky Way were performed by Jan Oort in 1932. These observations, followed by e.g. F. Zwicky (1933) for galaxies, were the earliest and the most convincing hints leading to the conclusion about the presence of an additional, invisible component of the galactic matter. In the late '60s Vera Rubin [60], analysed the star velocities in the Andromeda Galaxy using Doppler shift technique. She concluded that the galaxy extends far beyond the observable range, and consists mostly of dark matter. Dark matter is factor 10 to 100 more abundant in the galaxy than the visible baryonic matter. In the regions beyond the concentrated visible matter, the velocity v of a star should be inversely proportional to the square root of its distance r to the galaxy centre:

$$v(r) \sim r^{-1/2} \tag{1.10}$$

Fig. 1.7 shows the measured star rotational velocity as a function of star distance to the centre in the Messier 33 galaxy. It is clearly visible that the observed velocities are different from the expected velocity distribution, calculated assuming only the visible mass distribution. The mass distribution in centres of galaxies still holds some uncertainty, but the overall mass distribution may be deduced from the observed star velocities and is well described by the Navarro–Frenk–White (NFW) distribution [61]. Numerous galaxies were analysed for the rotational velocity distributions vs visible mass distribution, showing the same pattern of missing mass (e.g. NGC 2403, NGC 2841, NGC 2903, NGC 3196, NGC 6503, NGC 6603, NGC 7331). In 1933 F. Zwicky reported that some galaxies in the Coma Cluster exhibited unexpectedly high radial velocities. He proposed to explain the phenomenon by supplementing the visible mass by an additional dark matter[iv].

[iv] "Um, wie beobachtet, einen mittleren Dopplereffekt von 1000 km s^{-1} oder mehr zu erhalten, müsste also die mittlere Dichte im Comasystem mindestens 400 mal grösser sein als die auf Grund von Beobachtungen an leuchtender Materie abgeleitete." [58]

Another interesting observation is the Bullet Cluster, located 3.5 billion light years from the Earth. It is the proof for the existence of the inter–galactic dark matter. Collision of two galactic clusters led to separation of the baryonic matter and the dark matter. Dark matter, not interacting electromagnetically, passed the collision area without disorder, and within 200 million years moved away from the central collision area, leaving the baryonic matter behind. Fig. 1.8 shows the Bullet Cluster in visible light with superimposed mass distribution deduced from the weak gravitational lensing.

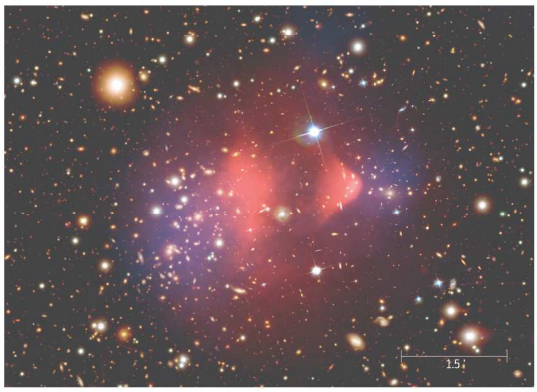

Figure 1.8: Composite image showing the Bullet galaxy cluster 1E 0657-56. The background image shows the visible spectrum of light (Magellan and Hubble Space Telescope images). The pink overlay shows the X–ray emission (recorded by the Chandra Telescope) of the colliding clusters, the blue one represents the mass distribution of the clusters calculated from gravitational lensing effects. Image taken from [62].

The other hints or evidences for existence of dark matter come from e.g. the primordial nucleosynthesis. Precise measurements, combined with the calculations involving the cross sections for numerous possible processes, the density and temperature evolution in time, Friedmann equations and general relativity, lead to the total density of the (visible) baryonic matter $\Omega_b \approx 4.0\,\%$. This result is consistent with the results obtained in observations of the cosmic microwave background radiation.

Cosmic Microwave Background Radiation (CMB) is the strongest indication for existence of the non–baryonic dark matter. The investigation of CMB was carried out in the space by several experiments: Wilkinson Microwave Anisotropy Probe (WMAP) [63], Sloan Digital Sky Survey (SDSS) [64] and Planck [65]. The radiation decoupled from the matter around 380 000 years after the Big Bang, and it has been propagating freely since then. The anisotropy of the radiation power spectrum carries the information about the state of the baryonic matter directly before the decoupling. The radiation power spectrum, registered with increasing accuracy in the WMAP, SDSS and Planck experiments, has a characteristic structure. Its properties are governed by the 6–parameter cosmological model. An extremely good agreement between the observational data and the model yields relative densities of baryonic matter, dark matter and dark energy as $\Omega_b = 4.6\,\%$, $\Omega_{CDM} = 24.0\,\%$, and $\Omega_\Lambda = 71.4\,\%$, respectively.

Weakly Interacting Massive Particles (WIMP) are considered as the constituents of dark matter in our Galaxy, where their interaction with baryonic matter via elastic scattering may be detected. The expected signal from the interactions is below or at the level of weak interactions for the typical WIMP mass range between 1 GeV and 1 TeV. It is assumed that the WIMPs bound in the gravitational potential of the Galaxy are cold, non–interacting and form spherically symmetric halo. If one considers argon as a target, the expected WIMP–nuclei interaction rate is at the level of $10^{-4}\,\mathrm{kg}^{-1}\mathrm{d}^{-1}$. This result is obtained under several assumptions: velocity distribution of WIMPs is Gaussian (the distribution is cut at the escape velocity of $544\,\mathrm{km\,s}^{-1}$), Sun rotational velocity of $250\,\mathrm{km\,s}^{-1}$, WIMP mass equal 100 GeV, elastic cross–section $10^{-45}\,\mathrm{cm}^2$ and WIMP density near the Sun equal $0.3\,\mathrm{GeV/cm}^3$. The interaction rate is high enough that the WIMP detection on Earth is feasible. The main obstacle for the observation is the identification of the particular interactions in the presence of the experimental background.

Most of the experiments searching for the dark matter interactions focus on the detection of the energy deposited by the dark matter particles scattered on target nuclei. WIMPs appearing in terrestrial detectors would primarily be those gravitationally bound to our Galaxy with the escape velocity of a few hundred $\mathrm{km\,s}^{-1}$ [66]. Therefore the maximum energy transfer (E_{rmax}) from a light WIMP to an atomic nucleus would be in the range of single keV. The expected interaction rate is also very low, so the experiments should exhibit an ultra–low background, at most comparable to the expected WIMP signal.

One of the most well known dark matter experiments is DAMA (Dark Matter Search). For several years the experiment had been collecting data using 9 NaI(Tl) scintillators, after 2003 extended to 25 crystals (DAMA/LIBRA). The PMTs worked in the coincidence mode, eliminating spurious events, generated by the

traces of radioactive contaminants in the PMTs or coming from the electronic noise. The increased distance between the crystals and the PMTs, low noise and the ultra–low background materials allowed registering of single photons and events down to 2 keV of the deposited energy. In total, the construction allowed reaching extremely low radioactive background.

Over 14 years of data taking by DAMA/LIBRA the model–independent annual signal modulation was observed. The modulation was energy dependent — only events in the 2 keV – 6 keV energy range excessed modulation in proper phase, amplitude and period, as deduced from the galactic halo model. The registered signal amplitude model, depending on the Earth's motion (and therefore on the time–dependent WIMP flux):

$$A = A_0 \cos \omega(t - t_0) \tag{1.11}$$

was fitted to the collected data in the 2 keV – 6 keV energy range, and yielded the following set of parameters: modulation amplitude $A_0 = (0.0112 \pm 0.0012)\,\mathrm{cts\,d^{-1}\,kg^{-1}\,keV^{-1}}$, amplitude's maximum (phase) $t_0 = (144 \pm 7)\,\mathrm{d}$, modulation period $T = 2\pi/\omega = (0.998 \pm 0.002)\,\mathrm{y}$, at the $9.3\,\sigma$ C.L. [67].

Possible sources of such modulated signal were taken into account. Firstly, the observed signal modulation was compared to the signal registered in the 6 keV – 14 keV range, where no modulation was asserted. This result excluded the neutron flux variable over a year as a source of modulation. Also, there was no modulation for multi–hit events in the 2 keV – 6 keV energy range, produced by thermal or fast neutrons. Finally, it was shown that not more than 0.5 % of A_0 might originate from the time–variable neutron flux. Also, variable muon flux can only be responsible for 0.3 % of the A_0 modulation. Other known sources were also excluded (detection efficiency changes, combined with calibration uncertainties account only for 2 % of A_0; electronic noise – 1 %; annual temperature shifts – 0.5 %; annual radon concentration changes – less than 0.2 % of A_0).

DarkSide is a multi–stage program aiming at development background–free detectors, deployed at the Gran Sasso underground laboratory (LNGS), searching for direct dark matter interactions. It is based on an advanced, low–radioactivity two–phase argon Time Projection Chamber (TPC). The choice of argon allowed for an extremely effective pulse shape discrimination (PSD) between different types of radiation (electronic recoils vs nuclear/WIMP–like recoils) and a possibility of a very efficient purification. The TPC filled with atmospheric argon, was operated in the DarkSide–50 detector since November 2013. The first results of a dark matter search for an exposure of $(1422 \pm 67)\,\mathrm{kg\,d}$ have proven truly background–free operation of the detector [68], for which the ultra–low background design was combined with the active suppression of residual backgrounds. Besides the very low intrinsic background levels, possibility of electron recoils discrimination and active suppression of the neutron background were demonstrated. The obtained result may be translated into a 90 % C.L. upper limit on the WIMP–nucleon spin–independent cross–section of $6.1 \times 10^{-44}\,\mathrm{cm}$, being also the strongest limit obtained with the argon target (for a WIMP mass of 100 GeV).

Fig. 1.9 shows the multi–layer design of the DarkSide–50 detector. The outermost water Cherenkov–veto (Water Cherenkov Detector – WCD) serves as passive and active shielding against cosmic muons and external gammas. The Liquid Scintillator Veto (LSV) is installed inside the water tank. The LSV, containing 50 % pseudocumene and 50 % trimethyl borate (TMB) scintillator, is serving as shielding and as anti–coincidence for radiogenic and cosmogenic neutrons (as a novelty in the dark matter searches), γ–rays, and muons. The independent trigger capabilities of the LSV allow for an in–situ measurements of the neutron background. The central part of the DarkSide–50 experiment is the double–phase TPC, filled with ∼46.7 kg of liquid argon (active mass). Photomultipliers, carefully selected for low–radioactivity, are installed in two arrays, registering the scintillation (in the liquid phase at the bottom) and ionization (in the gas phase) light. A uniform electric field ($200\,\mathrm{V\,m^{-1}}$) is maintained along the vertical axis of the cryostat, and a stronger electric field is used for the extraction of ionization electrons in the gas phase ($2800\,\mathrm{V\,m^{-1}}$). All internal surfaces of the TPC are reflective and coated with tetraphenyl butadiene (TPB), a wavelength–shifter required to convert the 128 nm LAr scintillation light to match the sensitivity of the PMT photocathodes. The TPC allows for event position reconstruction in 3D, it has also a very low intrinsic background (construction took place in a ^{222}Rn–suppressed clean room).

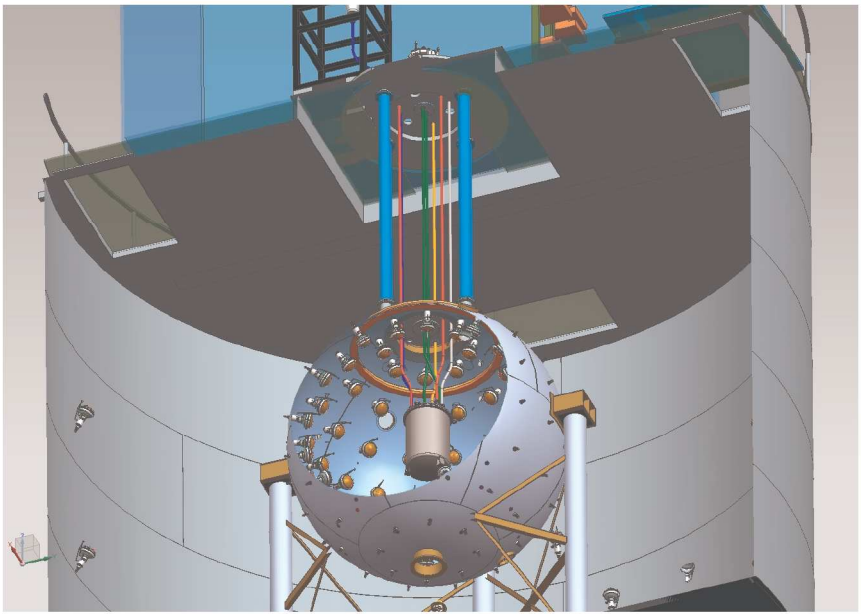

Figure 1.9: The nested detectors of the DarkSide–50 experiment. The innermost cylinder (grey) is the TPC, immersed in the LSV (central sphere), enclosed in the outermost WCD (grey cylinder).

The size of a liquid argon–based detector is limited by the the natural abundance of ^{39}Ar ($\sim$1 Bq kg^{-1}) in atmospheric argon, yielding a significant dead–time of the data acquisition systems. Therefore in order to overcome this limitation, DarkSide has decided to use argon depleted with ^{39}Ar, extracted from the underground gas deposit in Cortez (Colorado, USA). ^{39}Ar isotopic depletion of $< 1/300$ was achieved for the underground argon (UAr).

The first results from the DarkSide–50 detector are presented in Fig. 1.10. The distribution of events, obtained with the atmospheric argon is shown in the scatter plot of a prompt scintillation signal, called S1, and the PSD parameter, f_{90}, defined as the fraction of the signal occurring in the first 90 ns of the S1 pulse. f_{90} is typically $\sim$0.3 for β/γ–events and $\sim$0.7 for nuclear recoils. Events which showed a coincident energy deposition in the LSV (neutron detector) were vetoed. The PSD electron background discrimination achieved was $> 1.5 \times 10^7$ (as compared to the factor 10^2, available for liquid xenon). The exposure contains at least as many ^{39}Ar events as 0.6 t y of running with the underground argon. This means that DarkSide–50 could run for two decades with the UAr being free of ^{39}Ar background, solving the problem of the dead–time in a multi–tonne (future) detector.

LAr–TPC operation with UAr started on April 8, 2015. The goal is to acquire 0.08 t y exposure (within $\sim$3 y) to demonstrate the full background control (muon and neutron). A new approach to the light readout for multi–tonne detector, employing ultra–low background silicon photomultipliers (SiPM), is also under investigation. The SiPMs exhibit also an improved photon detection yield.

1.4 Radioactive ions in cryogenic liquids

Several experiments searching for rare nuclear processes at low energies are based on liquefied gases, profiting from the high purity levels achievable in the cryogenic liquids, serving as a coolant, a passive or active shield (Gerda [1]), or as a target, like in the XENON100 [69], LUX [70], or the DarkSide [2] experiments, to name a few. Isotopes produced in radioactive decays are usually charged, what in the presence of electric

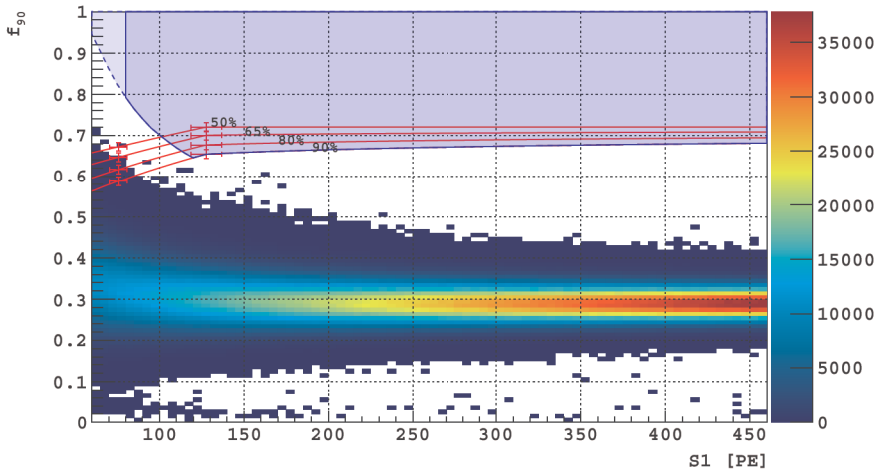

Figure 1.10: Distribution of the events in the scatter plot of S1 vs f_{90} after all quality and physics cuts. Signal from dark matter is expected in the shaded blue region with solid blue outline. The f_{90} acceptance contours for nuclear recoils are labelled (shown with error bars) and were determined in dedicated measurements [68].

fields (time projection chambers, germanium detectors) may significantly increase the background rate above the expectations, derived from the assumption about homogeneous distribution of the isotopes. After the thermalisation, atoms remain ionized for a significantly long time (neutralization in a high–purity liquid is naturally suppressed by the absence of impurities) to be drifted by the electric fields towards the active volume of a detector.

Better understanding of the ions' physical properties, like charged life–time in the cryogenic liquids, mobility and mechanisms of their creation, would lead to improvements in construction of new experiments and modification of the existing ones. Obtained results may be crucial for the better background estimation and predictions, considering spatial and temporal distribution of the ion–induced background. It would also be possible to employ the gained knowledge in designing more efficient ion traps, better shape the electric field around the detectors or shield them against the drifted activity.

The results of theoretical and experimental efforts devoted to understanding of the ions' properties are all relevant to the low–background experiments. Theoretical description of mobility treats positive and negative ions separately, as effects of their very different natures should be considered (see Chap. 2). For negative ions the repulsive exchange interaction along with the attractive polarisation interaction are the most important. Mobility of positive ions depends mainly on the electrostriction [71]. Fig. 1.11 depicts a comparison between the positive and negative ions in a liquid, forming different types of structures. The positive ion is closely surrounded by the liquid atoms. The bounding is caused by electrostriction forces: induced atomic dipoles are interacting with a non–uniform electric field of the ion. Size and mass of the formed cluster directly affects mobility of the cation. Anions are formed by an attachment of an extra electron, and the emerging exchange interaction between the lone electron and the electronic shells of surrounding atoms is, on average, repelling. A repulsion sphere is formed, outside of which the effect of electrostriction is weaker compared to the case of positive ions.

In Tab. 1.3 mobility of selected ions and electrons is compared. The mobility measurements and calculations of the theoretical values are referenced to the cryogenic liquid conditions, under which they were taken, like pressure, temperature or the external electric field strength.

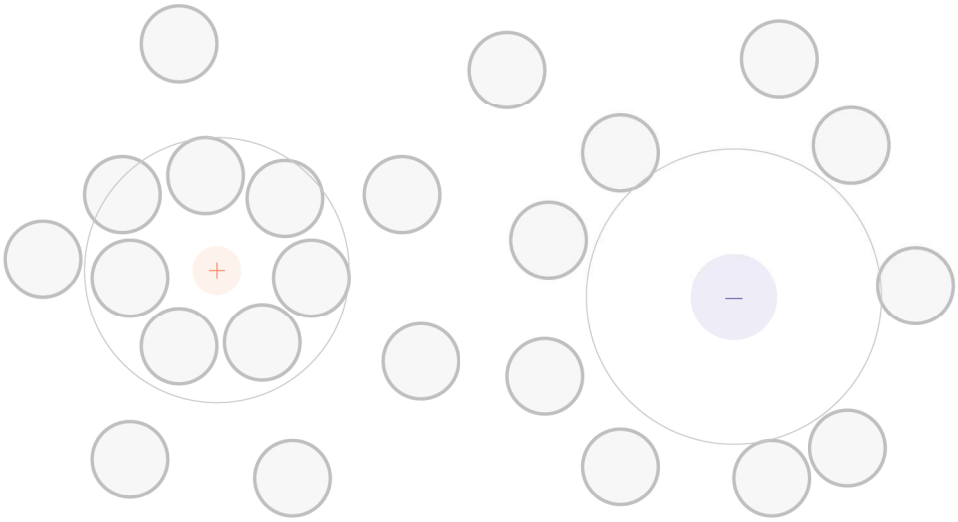

Figure 1.11: A concept view of a positive (left) and negative (right) ions surrounded by atoms in a liquid. The boundary between the positive cluster and the liquid is shown in grey. The anions have, on average, a smaller radius. Repulsion forces of the negative ion (bigger due to the extra electron) create a cavity around the anion.

Isotope	Mobility [$cm^2\,V^{-1}\,s^{-1}$]	Physical conditions	Ref.
Tl^+	$1.67^{+0.19}_{-0.09}\times10^{-4}$	Liquid xenon at 168 K and 1.2 bar	[72]
Sr^+	$2.73^{+0.33}_{-0.17}\times10^{-4}$	Liquid xenon at 168 K and 1.2 bar	[72]
Ba^+	$2.11^{+0.20}_{-0.12}\times10^{-4}$	Liquid xenon at 168 K and 1.2 bar	[72]
$^{226}Th^+$	$(2.40 \pm 0.16) \times 10^{-4}$	Liquid xenon (5.0) at 163 K and 0.9 bar	[73]
Ar_2^+	5.93×10^{-4}	theoretical prediction in liquid argon (STP)	[74]
Ar_2^+, O_2^-	2×10^{-4}	E-field strength up to 10 $kV\,cm^{-1}$, liquid argon (STP)	[75]
$^{208}Tl^+$	$(1.33 \pm 0.04) \times 10^{-4}$	$E = 4\,kV\,cm^{-1}$ to 10 $kV\,cm^{-1}$, drift distances up to 50 mm, liquid xenon (STP)	[76]
electron	>210	theoretical value, $E < 1\,keV\,cm^{-1}$ in liquid argon	[77]
electron	300	$E = 0.5\,keV\,cm^{-1}$ in liquid argon (STP, 15 ppt of oxygen equivalent impurity content)	[78]

Table 1.3: Theoretical and experimental mobility values, obtained for some ions of interest (and electrons) in cryogenic liquids, like xenon and argon. Physical conditions, under which the measurements or calculations were done, are also outlined.

2

Investigations of ^{222}Rn daughters in liquid nitrogen

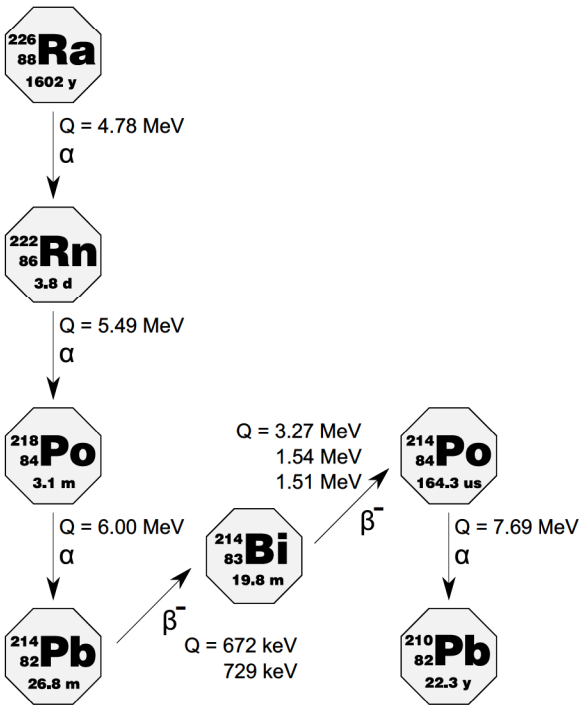

Figure 2.1: ^{222}Rn (^{226}Ra) decay chain.

^{226}Ra, present in almost all construction materials, is a constant source of easily diffusing noble gas ^{222}Rn (the decay chain is shown in Fig. 2.1). The long half–life and high mobility of ^{222}Rn allows the inert atoms to enter active volumes of detectors. Moreover, ^{222}Rn easily solutes in large volumes of cryogenic liquids. Together with impurities of ^{232}Th and ^{238}U, it is a possible source of background for the double beta decay signal, as gamma interactions in a germanium detector may easily mimic $0\nu\beta\beta$ events. Tab. 2.1 summarizes the most prominent (above 0.05 %) gamma lines with energies excessing $Q_{\beta\beta}$ of ^{76}Ge, accompanying the ^{214}Bi beta decay. Surface events, i.e. decays of atoms located right at the surface of a germanium detector, may also contribute to the background continuum around $Q_{\beta\beta}$.

According to the GERDA proposal [79], an upper limit of 200 µBq m^{-3} for the internal ^{222}Rn contamination was assumed for the liquid supply. This corresponds to 95 atoms/m^3. If the contamination does not decay with $T_{1/2} = 3.8$ d, but stays constant (due to permanent emanation), 6300 decays/m^3 have to be taken into account per year. A simulation showed that even this very conservative assumption leads to an upper limit of 0.1×10^{-3} cts keV^{-1} kg^{-1} y^{-1} for the background index, if the spatial distribution of ^{222}Rn and its progenies is homogeneous. The additional background from ^{42}Ar decays was also taken into account. The upper limit of the activity from ^{42}Ar is 40 µBq kg^{-1} [80]. A simulation showed that this results in a background of $< 10^{-4}$ cts keV^{-1} kg^{-1} y^{-1}, also for homogeneously distributed ^{42}K atoms, which was a strong assumption. According to our expertise in handling ^{222}Rn, investigations of ^{222}Rn activity dispersed in liquid nitrogen showed that ^{222}Rn and it's daughters may agglomerate on electrically polarized surfaces (in presence of an electric field) [81]. Until that moment, the homogeneous distribution of radioactive contamination was not questioned. These first observations needed further investigation, which is described in this chapter, as liquid nitrogen was considered as an alternative for liquid argon in the GERDA experiment. Moreover, liquid nitrogen may find an application in future ultra–low background experiments, as the high internal purity is relatively easy to achieve for this gas [82]. Strong interest in ^{222}Rn is also still relevant for GERDA, where backgrounds as low as 10^{-3} cts keV^{-1} kg^{-1} y^{-1} are desirable. As it will be shown in Chap. 3, devoted to ^{42}Ar/^{42}K problem, the cleaner the cryogenic bath is, the more inhomogeneous the distribution of radioactive ions exhibited will be. The simple explanation of this observable is that the ultra–pure environment naturally

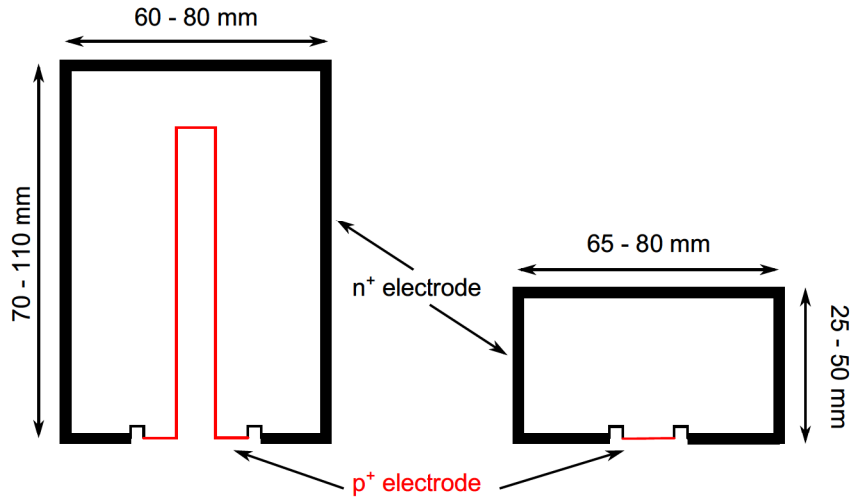

Figure 2.2: Schematic sketch of a coaxial HPGe detector (left) and a BEGe detector (right) with their different surfaces and dead layers (drawings not to scale). The p^+ read–out contact is at ground potential, while the detector bias of 3 kV to 4 kV is applied to the n^+ electrode.

lacks neutralizing agents, that might prevent drifting of radioactive ions under an electric field, induced by germanium detectors high voltage bias.

The sources of radioactive background may be grouped by the type of radiation or the place of their origin, relative to the active volume of a detector (e.g. germanium diodes). Close sources, including also surface contamination, emit α and β particles, that are able to penetrate dead layers of the detectors and deposit energy in single site–like interactions. Additionally, γ radiation is a concern for medium distance sources. All types of the α, β and γ radiation emitters can be found in the ^{222}Rn decay chain.

If the concentration of ^{214}Bi or other α–emitters close to the Ge detectors is enhanced, e.g. due to the shift in initially homogeneous distribution of the radioactive contamination, then the induced background increases. Geometrical effect plays a significant role: doubling the concentration close to the detector (due to the electrostatic shift) intensifies the background four times (as r^{-2} of the solid angle), while the overall (absolute) amount of radioactivity is constant.

Energy [keV]	Intensity [%]
2204	5.08
2448	1.57
2119	1.14
2293	0.305
2110	0.088
2053	0.069
2090	0.050

Table 2.1: Gamma lines of ^{214}Bi with intensities higher than 0.05 % and energies above $Q_{\beta\beta}$ of ^{76}Ge (2039 keV).

The range of alpha particles in cryogenic liquids and germanium is short (less than 100 µm). Therefore surface contamination of the germanium detectors has to be taken into account. ^{222}Rn, ^{218}Po and ^{214}Po are high energetic α–emitters (Fig. 2.1). Thickness of the p^+ surface dead layer (~300 nm) is not enough for stopping the alphas (compared to approximately 1 mm of the dead layer of the n^+ contact, see Fig. 2.2).

2.1 Radioactive ions in cryogenic liquids

Atoms, that undergo energetic alpha and beta (β^-) decays, form multiply charged cations. Heat released in the decays, Q, is dissipated mainly via electronic interactions and collisions between the decaying atom, released α or β^- particles, and the surrounding atoms, resulting in electron–ion pairs formed along the

tracks of the particles. The energy Q is expended in the production of a number of electron–cation pairs, N_i, excitation of atoms and sub–excitation electrons, and in atomic kinetic energy, E_k

$$Q = E + E_k \tag{2.1}$$

where E, being an average energy transfer to the electrons, is defined as

$$E = N_i E_i + N_{ex} E_{ex} + N_i \varepsilon \tag{2.2}$$

and N_i is the number of electron–cation pairs produced with an average energy E_i, N_{ex} is the number of medium excited atoms with an average energy E_{ex}, and ε is the average kinetic energy of the sub–excitation electrons (electrons unable to ionize or excite atoms, considered as heat). Excitation energy W, is the average energy needed to create a single electron–ion pair, including the three modes of the energy dissipation (Eq. 2.2). It is defined as

$$W = \frac{E}{N_i} = E_i + E_{ex}\frac{N_{ex}}{N_i} + \varepsilon \tag{2.3}$$

A typical value of W in liquid argon is (23.6 ± 0.3) eV [83], which is small compared to the typical deposited Q values.

The recoiling atom becomes positively charged after the decays as well. In a β^- decay, a nucleus emits an electron, and as a consequence of the charge conservation rule, the atom remains positively charged. In addition, during the thermalisation, valence electrons are stripped off in subsequent collisions with the surrounding atoms. A multiply–charged cation eventually slows down, and another process is possible, leading to a single positive charge carried by the atom. The first ionization energy (I.E.) is the energy required to remove a bound shell electron from a neutral atom or a molecule. The second I.E. is the energy associated with the removal of a second electron from a singly ionized particle, and so further for higher I.Es. Due to the significant differences between the first and the second ionization energies of the elements and environment atoms or molecules (in form of the cryogenic liquids), a multiply ionized atom is able to acquire electrons only until it is singularly ionized. Also, the 1^{st} I.E. are lower for the radioactive (heavier) elements and potassium (see Chap. 3), thus their cations remain singularly charged, unable to capture electrons from the neutral atoms of the liquid. Tab. 2.2 reports the ionizing energies of the considered elements.

In the case of an α–decay, the initially negatively charged atom (due to the emission of +2e charge), has a fair chance of becoming a cation. The recoil energy of the atom, in the order of 100 keV, is high enough to strip off extra electrons during the thermalisation, along with the shell electrons. Then the process of recombination leads the atom to the singularly charged cation state, as previously described.

2.1.1 Mobility

The electric force, acting on an ion present in a liquid, is compensated by the friction force. In such assumption, ions are considered as spheres experiencing friction force following Stokes' law. A modified Walden's Rule is used to describe the relation between the mobility μ and the liquid viscosity η:

$$\mu\eta^{\kappa} = \text{const} \tag{2.4}$$

where experimentally determined κ varies between 1 and 1.5. This model fails to explain the observed difference between the positive ($\kappa \approx 1.5$) and negative ions ($\kappa \approx 1$).

In a general theoretical model, the ion's mobility depends on the structure formed by the surrounding atoms of the liquid. The structure is a consequence of the sign of the charge. A positive ion exerts an electric force on the neighbouring atoms, inducing dipoles. The energy of interaction between the ion and a polarized atom is

$$W_{\text{pol}} = \frac{\alpha_{\text{pol}} e^2}{32\pi^2 \varepsilon_0^2 \varepsilon_1^2 r^4} \tag{2.5}$$

Property	unit	N_2	Ar	Xe	Rn	Po	Bi	Pb	K
polarizability	$Å^3$	1.7	1.6	4.0	5.3	6.8	7.4	6.8	43.4
dielectric constant, ε_l		1.43	1.50	1.87	—	—	—	—	—
dielectric constant, ε_s		1.52	1.59	*1.96*	—	—	—	—	—
atomic radius[ii]	Å	1.55	1.88	2.16	2.20	1.97	2.07	2.02	2.31
boiling point, T_{bp}	K	77.4	87.3	165	—	—	—	—	—
viscosity at T_{bp}[iii]	$\mu g\,cm^{-1}\,s$	1660	2700	4700	—	—	—	—	—
electron affinity	$kJ\,mol^{-1}$	-7	-35	-41	-41	183	91.3	35.1	48.4
1st I.E.[iv]	$kJ\,mol^{-1}$	1503	1520	1170	1037	812	703	716	419
2nd I.E.	$kJ\,mol^{-1}$	2615	2665	2046	1930	*1800*	1610	1450	3051

[ii] van der Waals
[iii] $p = 1000\,mbar$
[iv] I.E. – ionization energy

Table 2.2: Atomic properties of elements used in the study. For some elements only relevant or known properties are listed. Numbers in italics are uncertain or estimated.
$1\,kJ\,mol^{-1} = 1.04 \times 10^{-2}\,eV$ per particle. For reference see [84].

where α_{pol} is the polarizability of the liquid, e is an electron charge, ε_l is the dielectric constant of the liquid, ε_0 is the vacuum permittivity and r is the distance between the two atoms. At nitrogen boiling point temperature ($T = 77\,K$) equating W_{pol} to kT yields $r_{kT} = 5.5\,Å$ (liquid nitrogen and other gases atomic parameters are summarized in Tab. 2.2). This value may be considered as an average radius of the cluster formed by the liquid nitrogen particles (N_2) around the positive ion, made of approximately two to three layers of N_2 molecules. In the case of liquid argon $r_{kT} = 5.1\,Å$.

In a more detailed approach, additional energy terms affecting formation of the ion cluster would have to be considered. Solidification of the atoms requires volume work W_{vol}, expended on the phase transition. The cluster is separated from the liquid by a surface, created with the surface energy W_{sur}. Total energy in the system is conserved, i.e. in the equilibrium point (for a given cluster radius r):

$$W_{est} + W_{vol} + W_{sur} = 0 \tag{2.6}$$

where W_{est} is the work of the electrostatic field during the phase transition, originating from the difference in dielectric constants of solid (ε_s) and liquid (ε_l) phases of the surrounding atoms:

$$W_{est} = \frac{e^2}{8\pi\varepsilon_0 r}\left(\frac{1}{\varepsilon_s} - \frac{1}{\varepsilon_l}\right) \tag{2.7}$$

The surface energy W_{sur} may be neglected (at higher temperatures) and Eq. 2.6 yields the radius r of the ionic cluster in the equilibrium. It is a better approximation of r than given by Eq. 2.5. The volume work may be calculated as $W_{vol} = p\Delta V$, where $\Delta V = \frac{n_s - n_l}{n_l}\frac{4\pi r^3}{3}$, n_s and n_l are density numbers of solid and liquid phases, respectively[i]. The radius r is then used to calculate the ion's mobility in a liquid:

$$\mu = \frac{e}{6\pi\eta r} \tag{2.8}$$

where η is the liquid's viscosity. The resulting ionic cluster radius depends also on dimensions of the foundational ion (here approximated by the van der Waals atomic radius). The theoretical value of mobility, calculated using Eq. 2.5 and 2.8, ranges from $0.025\,mm^2\,V^{-1}\,s^{-1}$ (radon atom in liquid xenon) to $0.069\,mm^2\,V^{-1}\,s^{-1}$ (polonium in liquid nitrogen). A bismuth atom surrounded by a three–layer structure of nitrogen molecules would exhibit theoretical mobility of $0.028\,mm^2\,V^{-1}\,s^{-1}$. These results may be compared with e.g. the measured value of μ for ^{226}Th ions in liquid xenon at 163 K and 0.9 bar: $0.024\,mm^2\,V^{-1}\,s^{-1}$ [73] (see also Tab. 1.3).

[i] Volume number density is the number of particles N per unit volume V, $n = N/V$.

2.1.2 Ionic life–time

The life–time of an atom in the ionized state strongly depends on the chance of neutralization with an electron. Depending on the electron origin, two of the neutralization processes will be described here. The germinate neutralization follows the ionization immediately after the ion thermalises, and strongly depends on the ionization density caused by the recoiled ion. The bulk recombination is caused by the non–zero impurity concentration in the cryogenic liquid, and occurs on the course of the ion.

Germinate (primordial) recombination In the presence of an external electric field, particles of the opposite signs become separated, as electrons exhibit much higher mobilities (see Tab. 1.3) compared to the typical mobilities of heavy ions. In the described model of germinate recombination, ions are considered motionless (electron mobility is approximately 6 orders of magnitude higher). In such conditions the chance of an ion recombining with one of the electrons freed during the thermalisation is a function of the electron density, i.e. ionization density. The model proposed by J. Thomas [83] gives an estimation of the charge fraction $\varepsilon = C/C_0$, surviving the primordial recombination, as a function of ionization density:

$$\varepsilon = \frac{C}{C_0} = \frac{\ln(1+\xi)}{\xi} \tag{2.9}$$

where C_0 is the initial charge produced by the thermalisation, and ξ is defined as

$$\xi \cdot E = \frac{N_i \alpha}{4a^2 \mu_-} \tag{2.10}$$

where N_i is, as previously, the number of electron–cation pairs produced within a box of dimensions a, α is the recombination coefficient, μ_- is the electron mobility, and E is the external electric field strength.

Values of $\xi \cdot E$ for different interactions in dense materials are obtained experimentally. 364 keV electrons yielded in liquids the value of $\xi_\beta \cdot E = 840\,\mathrm{V\,cm^{-1}}$, while 5.64 MeV α's yielded $\xi_\alpha \cdot E = 470\,\mathrm{kV\,cm^{-1}}$ [83]. The significant difference is hence clearly visible in the fractions of the cation–electron pairs surviving germinate recombination: in e.g. electric field of $30\,\mathrm{V\,mm^{-1}}$, the fraction C/C_0 for β–particles is 48 %, while for the α–particles the fraction is only 0.47 %, over 100 times less. This result is relevant to understanding the observed difference in the amounts of radioactive ions of the same elements, but produced in the different radioactive decays.

Bulk recombination On their way in the electric field, Y^+ cations may be neutralized by charge exchange with electronegative Z^- impurities:

$$Y^+ + Z^- \rightarrow Y + Z \tag{2.11}$$

If the concentration of impurities is much higher than the amount of cations, then it might be considered constant. Then the neutralization rate is

$$\frac{\mathrm{d}[Y^+]}{\mathrm{d}t} = -k_{Z^-}[Y^+][Z^-] \tag{2.12}$$

where quantities in square brackets denote concentrations, and k_{Z^-} is a (constant) rate of neutralization. As a result, concentration of the cations decreases with a characteristic time constant τ:

$$[Y^+](t) = [Y^+]_0 e^{-k_{Z^-}[Z^-]t} = [Y^+]_0 e^{-t/\tau} \tag{2.13}$$

The time $\tau = (k_{Z^-}[Z^-])^{-1}$ is called the cation (ionic) life–time.

Cations moving along the electric field lines with a constant velocity v, travel the distance λ in the time τ equal:

$$\lambda = v\tau \tag{2.14}$$

defining the cation charge attenuation length (range).

Another possible way to neutralize the cations is by free electrons. But as the (electronegative) impurity content supersedes that of free electrons, this mechanism is negligible. Yet another aspect is the high electron mobility, resulting in quick removal of electrons in presence of the electric field. The obvious ion life–time limiting factor is the cation radioactive decay, with characteristic nuclear half–life. Obviously, if the ionic life–time is short compared to the nuclear $T_{1/2}$, then this mechanism is also negligible.

It is worth noting, that the differences in the ionizing potentials of the ^{222}Rn daughters and the considered liquefied gases (see Tab. 2.2) enable a recharge mechanism. If the difference in ionizing potentials of two different elements exceeds 190 kJ mol^{-1} (2 eV), then electron exchange is possible between the neutral ^{222}Rn daughter and the cation:

$$Y + Z^{+} \rightarrow Y^{+} + Z \tag{2.15}$$

In consequence, the radioactive atom may be recharged in such certain circumstances, and its ionic life–time may extend. Higher values of the second ionizing potentials of the elements disallow multiple ionization.

2.2 ^{222}Rn daughters in liquid nitrogen

^{222}Rn is constantly produced by naturally abundant ^{226}Ra. ^{222}Rn as a noble gas, easily dissolves in cryogenic liquids and enters active volumes of detectors. Ions produced in the ^{222}Rn decay chain reach the vicinity of an electrically polarized detector by means of convection flows and electrostatic drift. Behaviour of ^{222}Rn and its daughters in liquid nitrogen was investigated in more details. A simple cryogenic setup described in this section was constructed to study different ionic properties of ^{222}Rn daughters, such as charge survival probability (depending on the type of radioactive decay producing an ion), expected ionic life–time or negative ion yield. A versatile method of direct α–decays registration in cryogenic liquids is also presented, developed in the frame pf this PhD.

For the purposes of data analysis and interpretation, a set of dedicated computer programs was developed. They were used to model the electric field lines (estimation of the detection efficiency), to compute the mean charge survival probability (as a function of the local electric field strength E) and ion trajectories towards the detector (for a given ionic mobility μ).

2.2.1 Principle of the measurements

Radioactive decays in the ^{222}Rn chain are governed by the set of Bateman's equations. A general algebraic form of the solution to these equations is shown in Eq. 2.16 [85]. Vector $\boldsymbol{N}(t)$ represents the exact amounts of the isotopes (i–th component), while $N_{i,0}$ are the initial amounts of each of the isotopes. The matrix coefficients F, S, and T are defined in Eq. 2.17, where customarily λ are decay constants of consecutive isotopes in the decay chain, i.e. ^{218}Po, ^{214}Pb, ^{214}Bi, and ^{214}Po. Exact solutions for the isotopes can be found in the reference [85]. Decay constant of ^{214}Po is significantly higher than the other three (radioactive half–life is only 164.3 µs). This nuclide undergoes immediate decay in the experimental time–scale, thus it's activity corresponds exactly to the activity of it's parent ^{214}Bi. In consequence, it is enough to consider the ^{222}Rn decay chain down to ^{214}Bi only.

$$\boldsymbol{N}(t) = \begin{pmatrix} N_1(t) \\ N_2(t) \\ N_3(t) \\ N_4(t) \end{pmatrix} = \begin{pmatrix} 1 & 0 & 0 & 0 \\ S_{2,1} & 1 & 0 & 0 \\ S_{3,1} & S_{3,2} & 1 & 0 \\ S_{4,1} & S_{4,2} & S_{4,3} & 1 \end{pmatrix} \times \\ \mathrm{diag}(\mathrm{e}^{-\lambda_1 t}, \mathrm{e}^{-\lambda_2 t}, \mathrm{e}^{-\lambda_3 t}, \mathrm{e}^{-\lambda_4 t}) \times \begin{pmatrix} 1 & 0 & 0 & 0 \\ T_{2,1} & 1 & 0 & 0 \\ T_{3,1} & T_{3,2} & 1 & 0 \\ T_{4,1} & T_{4,2} & T_{4,3} & 1 \end{pmatrix} \times \begin{pmatrix} N_{1,0} \\ N_{2,0} \\ N_{3,0} \\ N_{4,0} \end{pmatrix} \tag{2.16}$$

$$F^p_{q,r} = \frac{\lambda_r}{\lambda_q - \lambda_p}, \qquad S_{i,j} = F^j_{i,i-1} F^j_{i-1,i-2} \cdots F^j_{j+1,j}, \qquad T_{i,j} = F^i_{j,j} F^i_{j+1,j+1} \cdots F^i_{i-1,i-1} \tag{2.17}$$

A dedicated setup was developed to investigate the behaviour of radioactive ions in the liquid nitrogen. First of all, a set of measurements was performed to show that the Si–PIN diodes can be used to directly observe the α–activity in liquid nitrogen. Next, the research focused on the registration of time–varying signal of ^{214}Po and ^{218}Po α–decays. The signal was expected to depend on amplitude and polarity of the applied high voltage bias, responsible for drifting the charged products of α and β–decays in ^{222}Rn chain, occurring in liquid nitrogen.

The experience gained during the measurements with use of stainless steel plates immersed in the ^{222}Rn–doped liquid nitrogen, was here adapted to improve the detection efficiency and provide a real–time signal readout [86][v]. A new technique was proposed to directly detect α–decays of ^{218}Po and ^{214}Po on the surface of a Si–PIN diode, used as the α–decay detector.

2.2.2 The measurement setup

A sketch of the measurement setup is shown in Fig. 2.3. A liquid nitrogen cryostat (32 l) was placed on a weight scale, used to register the liquid losses due to free evapouration (boil–off process). A bare silicon–PIN diode (Hamamatsu model S1223–01 without a glass window) was immersed in the liquid, hanging on a stiff signal cable, in a fixed position inside the dewar. The housing of the diode was grounded and wired to the cable shield. The cryostat was electrically isolated from the ground, allowing its conductive internal surface to be biased. The reference ground potential was applied to the shield of the signal cable. The electrical configuration of the setup worked as a drifting chamber for positive or negative ions. By applying a positive bias to the housing, cations were repelled towards the

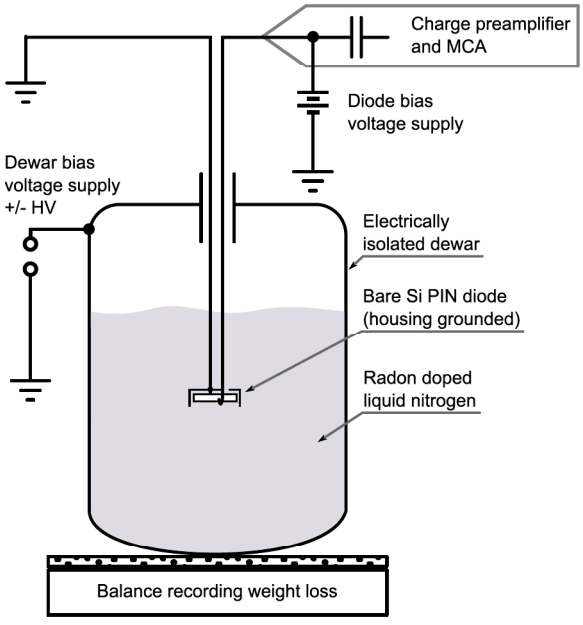

Figure 2.3: A schematic view of the measurement setup. The cryostat is electrically isolated, and may be biased to bipolar high voltage. The detector (Si–PIN diode) is kept at the ground potential (the diode bias is only 27 V). The ground reference is applied to the signal cable shield. Radon concentration changes in time as the liquid freely evaporates. To account for that effect, the loss of liquid is recorded during the measurements.

[v] The plates were polarized to collect positive or negative ions from the liquid volume. Next, they were placed in an α spectrometer for measurements of the deposited activity.

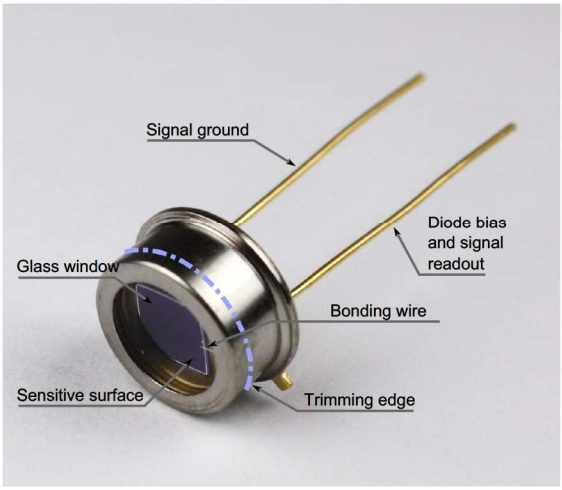

Figure 2.4: The Hamamatsu S1223–01 Si–PIN diode used in the study. The diode housing was trimmed in order to remove the glass window and partially the metal housing for better exposition of the active surface to α radiation. The active surface of the diode was directly exposed to the liquid. Since the diode is light–sensitive, the cryostat volume was light–tight.

Bias [kV]	$V_{av}^{6.5}$ [cm^3]	$V_{av}^{12.5}$ [cm^3]	V_{av}^{15} [cm^3]
0.5	27	138	210
1.0	29	151	270
2.0	30	158	290
σ_{sys}	$^{+2}/_{-3}$	$^{+4}/_{-4}$	$^{+15}/_{-19}$

Table 2.3: Available volume V_{av} for three distances of the Si–PIN detector to the bottom of the cryostat, 6.5 cm, 12.5 cm and 15 cm, respectively. The systematic error is also given in the table (the maximum values are quoted). It was estimated by varying the computation accuracy of the electric field lines and the detector position.

Si–PIN detector, being on a lower (ground) potential. By applying a negative bias, anions were transported by electric forces towards the diode, therefore the drifted ion polarity could be studied.

Si–PIN diodes were chosen for their ability to work at liquid nitrogen temperatures, and in a direct contact with the liquid. A typical diode used during the measurements is shown in Fig. 2.4. Such units are normally used as visible– to near– infrared precision photometers. In order to protect the sensitive semiconductor surface, they are equipped with glass windows (the semiconductor surface in this type of Si–PIN diodes in not covered with transparent coatings). The windows had to be removed as the range of α–particles exhibit a very limited range in dense materials, therefore the diode housing was trimmed. The exposed semiconductor surface is very sensitive to mechanical stresses, so special handling was required afterwards, but several cycles of cooling in liquid nitrogen had no negative impact on the properties of the detector. The trimmed diode was cooled down in cold vapour prior to immersion in the liquid. The temperature of vapours (in the gas above the liquid) was estimated to be higher by less than 15 K above the liquid nitrogen boiling point. Thanks to the slow heat exchange between the vapour and the diode, the semiconductor structure was never exposed to abrupt mechanical stresses (especially, the most sensitive bonded wires). Also, this procedure prevented moist from freezing out on the semiconductor surface.

A three–dimensional model of the cryostat geometry was worked–out. Basing on it, a geometrical mesh was generated for E–field calculations. The configuration of the electric field distribution in the dewar was next modelled in detail. Fig. 2.5 shows a cross–section of the electric field distribution calculated for the typical bias of 2 kV applied to the cryostat walls. Similar computations were also performed for the reversed polarity and different magnitudes of the applied bias (the diode bias was always 27 V). Fig. 2.6 depicts a cross–section of the cryostat volume below the Si–PIN detector. The cryostat bias is 2 kV, while the diode bias is 27 V, all with respect to the signal cable ground. The E–field lines closing on the diode active surface guide positively charged ions.

The E–field calculations were used to estimate the average electric field strength, experienced by the ions. Also, the active volume of the liquid was computed, from which ions may be effectively drifted and, consequently, detected. The software used for the study is Gmsh [87] (geometry definition, volume mesh generation, post–processing and visualisation), and GetDP [88] (finite–element solver, used for E–field computations) and a simple custom–made code to compute the active volume.

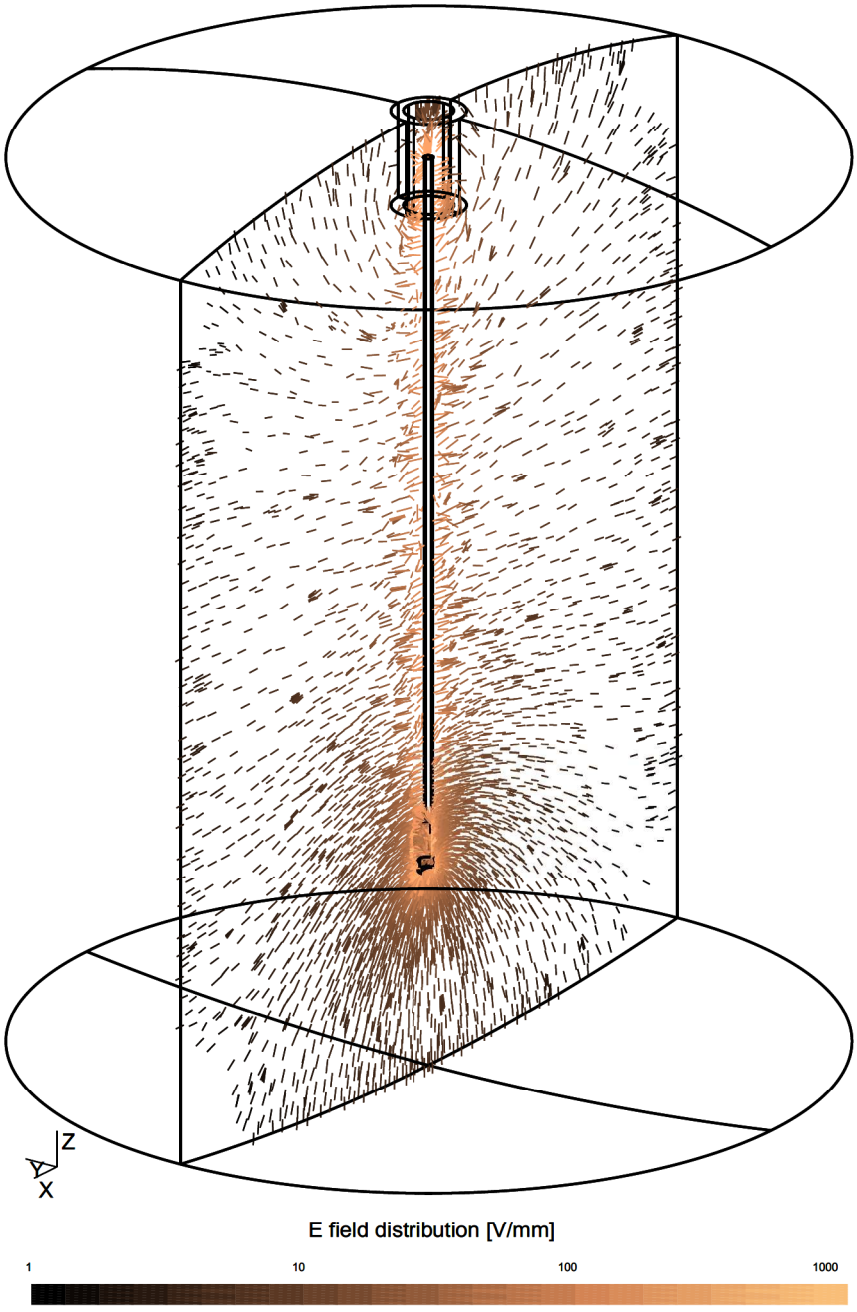

Figure 2.5: Results of a detailed computation of the three–dimensional electric field distribution. 3D geometrical model was developed and used to compute the E–field. The electric field strength is given in V mm^{-1}. Only the cross–section through the E–filed is shown for clarity.

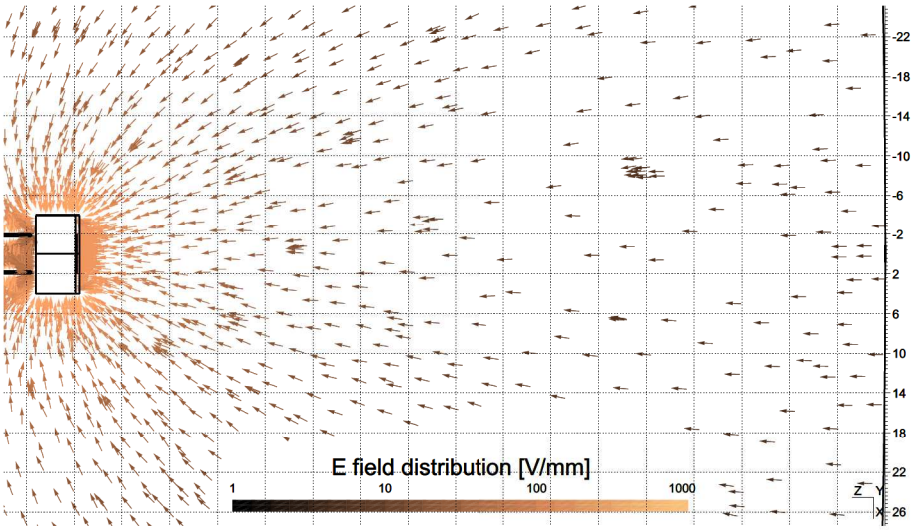

Figure 2.6: A close–up of the E–field distribution between the Si–PIN detector and the bottom of the cryostat. The electric field strength is given in $\mathrm{V\,mm^{-1}}$. The physical dimensions are in mm. The cryostat is biased to 2 kV, the reverse diode bias is 27 V. The distance between the diode and the bottom of the cryostat is 68 mm. Relative permittivity of the liquid (nitrogen) was taken into account in the computation. The average E–field strength in the volume below the Si–PIN detector is $30\,\mathrm{V\,mm^{-1}}$.

The shape of the electric field determines the liquid volume, from which radioactive ions may reach the detector, following the electric field lines and reaching the active surface of the Si–PIN detector. The computation procedure is based on Monte Carlo sampling starting points in a given volume V, located below the detector[vi]. Next, the trajectories of trial charges were computed down to 0.1 mm accuracy (yielding the electric field lines). From the known initial amount N_{tot} of sampled particles (trial charges) only a fraction N_{det} reaches the detector. The fraction is then used to compute the available volume $V_{av} = N_{det}/N_{tot} \cdot V$. Depending on the distance between the Si–PIN diode and the bottom of the cryostat, the volume varies significantly (see Tab. 2.3). The available volume V_{av} is then used to calculate the specific ^{222}Rn activity for a given geometry.

Each measurement cycle started with dissolving an amount of radon activity on the order of 16 kBq from a ^{222}Rn source[vii] (Fig. 2.7). The volume of the ^{222}Rn source was flushed with nitrogen, and a cold trap was applied to remove traces of humidity in the gas (the trap temperature range was −70 °C to −60 °C), as it could degrade it's purity. Moreover, significant concentrations of electronegative ions (e.g. oxygen, carbon dioxide, water) would limit the life–time of the radioactive ions and a thin film of moisture, that may form on the sensitive surface of the diode, would degrade the energy resolution. The gas outlet was placed in the liquid nitrogen cryostat. Bubbles of the carrier gas ascended to the surface, partially dissolving in the cryogenic liquid. The entire ^{222}Rn activity was transferred to the cryoliquid. Efficiency of this process was also monitored using a ZnS(Ag) scintillation chamber, detecting the residual radon activity at the system exhaust. The procedure lasted for 30 min at carrier flow of about $0.5\,\mathrm{l\,min^{-1}}$ to fully flush the ^{222}Rn source volume.

Measurements were started at least three hours after the doping procedure. This time is required to reach secular equilibrium in the ^{222}Rn decay chain, present inside the cryostat.

[vi] Inspection of the electric field allows to optimize the computation by limiting the sampled volume to the space below the diode.

[vii] The radon source consists of ^{226}Ra solution (18 kBq of activity), enclosed in a silicon pipe placed in a small metal vessel. Ca. 90 % of radon diffuses through the pipe and accumulates in the vessel. The vessel is flushed with nitrogen gas to extract the activity.

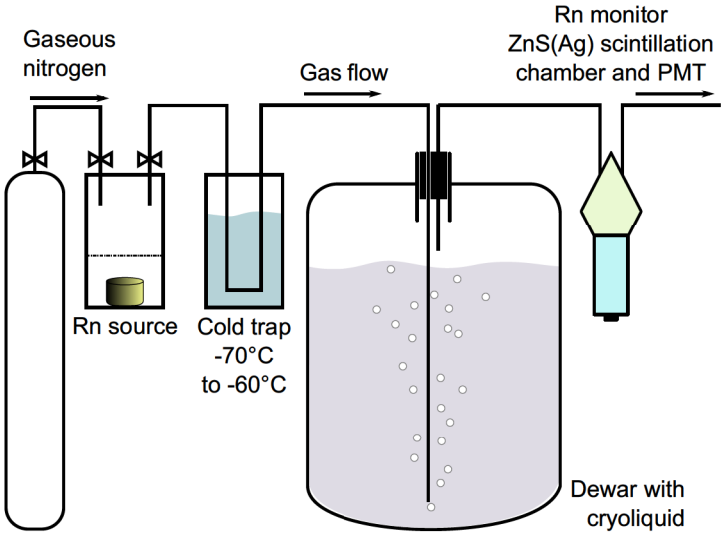

Figure 2.7: The setup used to dissolve ^{222}Rn in liquid nitrogen. A custom–made ^{222}Rn source is flushed with gaseous (warm) nitrogen. The carrier gas passes through a low temperature moisture trap (cold methanol bath). Exhaust gas is monitored for the remnants of radon activity and since no signal is detected at the outlet, all ^{222}Rn is expected to remain in the liquid.

High voltage bias is applied to the cryostat housing only to drive the radioactive ions towards the detector. Magnitude and polarity of the bias is controlled by the HV power supply installed in a NIM crate, along with the spectrometry electronics chain. This configuration ensures noiseless operation of the setup thanks to the short interconnections and no ground loops.

Signal readout is performed with a standard spectrometry electronics chain, composed of a charge sensitive preamplifier and a shaping amplifier. The conditioned signal is registered with a multi–channel analyser (MCA, Ortec TRUMP–PCI–8k) used to register the alpha–energy spectrum. The MCA is installed in a PC–computer, and is operated with a dedicated software (Ortec MAESTRO–32). In order to evaluate the time–dependant ionic flux the energy spectra are recorded in 15 min time–windows. The data–taking in time–windows is fully automated in the MAESTRO software (a dedicated script was written), allowing reduction of dead–time between the consecutive measurements to zero (the MCA has a double–buffered structure). Duration of the window was chosen experimentally to ensure statistically satisfactory signal from alpha decays of ^{218}Po (statistical error below 30 %) and ^{214}Po (statistical error below 3 %). A typical energy spectrum of Rn–doped liquid nitrogen is shown in Fig. 2.8, with 2 kV applied to the cryostat.

An example of the entire data–taking period, called a *run*, is presented in Fig. 2.9. This is an ensemble of the energy spectra stored every 15 min (Fig. 2.8) in consecutive time order. In total over 14 days of data–taking is shown with various values of high voltage bias applied (vertical bands). Inspection of such plots proves that the data–taking was stable (especially the energy scale stability), the high voltage was not interfering with the signal path, and the system was noiseless (no spurious events registered).

The measurements allowed to estimate the ionic life–time under the assumption of fixed ion mobility. The mobility itself could not be determined in the performed experiments due to the setup limitations. These were: minimum time resolution of the MCA system registering integral energy spectra (in order to obtain reasonable statistics to perform fits), MCA lacking a precise event time–stamp information, and a uniform distribution of the ^{222}Rn activity over the volume of the cryostat. A dedicated setup was later (in 2015) designed to determine the mobility of radioactive ions in the cryogenic liquids (and gases, see Chap. 2.3). Nevertheless, ionic range may be easily extracted from the data, as it appears as combined average ionic life–time and mobility:

$$d = \mu E \tau \tag{2.18}$$

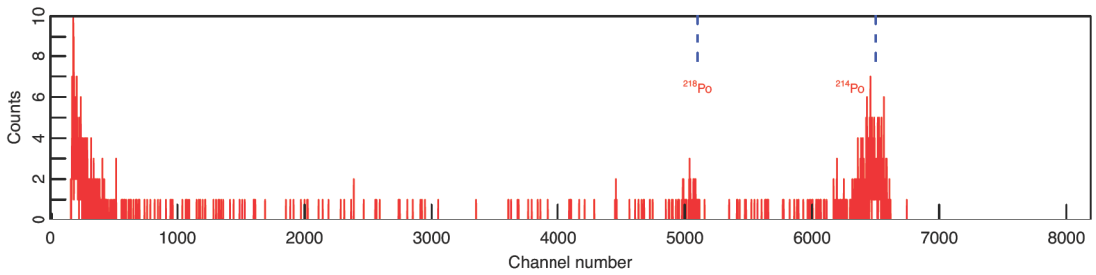

Figure 2.8: A typical energy spectrum registered in Rn–doped liquid nitrogen, contained in the described setup. Dashed lines indicate positions of ^{218}Po and ^{214}Po peaks, respectively. 2 kV was applied to the cryostat.

Run number	Duration [days]	HV bias [kV]	Remarks
1	6	+2	Air dissolving test
2	15	$0 \rightleftharpoons 2$	
3	15	0	Long–term system stability test
4	16	+2	Long–term system stability test
5	15	$-2 \rightleftharpoons +2$	
6	14	+2	Problems with electronics – discarded
7	9	$-1 \rightleftharpoons +1$	
		$+1 \rightarrow +2$	
		$+2 \rightleftharpoons -2$	
8	15	$+0.5 \rightleftharpoons +2$	
		$-0.5 \rightleftharpoons -2$	
		$+2 \rightleftharpoons -2$	
9	9	+2	Checked impact of short HV interrupts
10	15	+2, –2	Ion range tests

Table 2.4: Summary of the performed measurements. Behaviour of the ions was studied with different HV bias magnitudes and polarizations. Changes in the bias voltage allowed to investigate the composition of ions deposited on the detector.

Different biasing schemes were studied during the investigation, as it is summarized in Tab. 2.4 (in total 10 runs). The HV bias magnitude and polarization allowed to select between the opposite charges of the drifted ions. HV transients (e.g. changes between 2 kV and −2 kV) were used to estimate the composition of the ion flux, i.e. the amounts of different isotopes deposited on the Si–PIN detector, through the fits of Bateman equations to the (decaying) signal from ^{218}Po and ^{214}Po.

2.2.3 Experimental results

Most of the alpha activity registered by the detector is deposited directly on it's surface. Otherwise the short range of alpha particles in liquids renders decays of floating ions invisible to the detector. Only a thin layer of ions (less than a few tens of microns into the liquid volume) may contribute to the long background

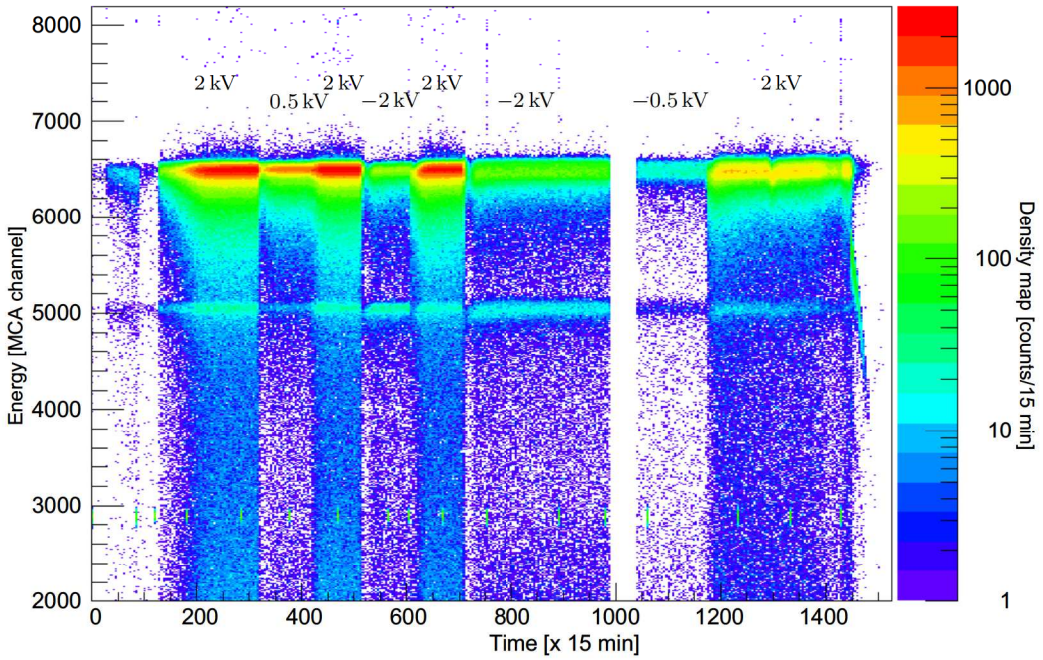

Figure 2.9: Colour–coded time evolution of the alpha particle energy spectrum. The clearly visible horizontal bands represent events from ^{214}Po (around MCA channel $\sim$ 6500) and ^{218}Po (MCA channel $\sim$ 5000). The signal chain stability was inspected on a regular basis with a pulse generator (separate stripes around channel 2900). Vertical bands stem from changes in the bias voltage driving different species of ions towards the detector. The horizontal scale is expressed in time–windows of 15 min each, the vertical scale is proportional to the event energy as an MCA channel number, while the counts are colour–coded (mapped). As an example, vertical cross–section of the plot is shown in Fig. 2.10.

tails of the alpha–peaks. Therefore the peak shapes should be modelled taking into account this fact [89]:

$$f(x) = A \cdot \exp\left(-\frac{(x-x_0)^2}{2\sigma^2}\right) + A\sigma\sqrt{\frac{\pi}{2}} \cdot \sum_i a_i \exp\left(\frac{2\varepsilon_i(x-x_0)+\sigma^2}{2\varepsilon_i^2}\right) \cdot \operatorname{erfc}\left(\frac{\varepsilon_i(x-x_0)+\sigma^2}{\sqrt{2}\varepsilon_i\sigma}\right) \tag{2.19}$$

where A is the height of the full energy peak at its position x_0, σ is the Gaussian width of the peak, a_i is the contribution of the i–th tail function relative to A, ε_i is the decay constant of the i–th tailing function, and erfc is the complementary error function. The ^{214}Po peak shape was best modelled using three tailing functions ($i = 1, 2, 3$). The ^{218}Po peak shape was modelled only by a Gaussian function (contribution of the peak tail is negligible for low activities of ^{218}Po and was often impossible to carry out convergent fitting procedure). Fig. 2.10 shows, as an example, results of simultaneous fitting of the ^{214}Po and ^{218}Po peak shapes to the data collected in 15 min. In the case of ^{214}Po line, the proposed α peak shape does not include the effect of the peak broadening towards higher energies. The broadening is caused by the accumulated energy from preceding ^{214}Bi beta–decay (see ^{222}Rn decay chain shown in Fig. 2.1), so called Bi–Po coincidence. As some of such coincident β–α decays occur within the shaping time of the spectroscopic amplifier, the registered energy of the alpha decay is higher, thus the peak is slightly broadened. In the case of the described experiment, the effect is visible but still negligible and does not affect the ^{214}Po peak statistics (less than 1 ‰).

Using the fit procedure (implemented in the ROOT environment to automatize it over the whole data set), count rates from ^{214}Po and ^{218}Po, collected on the Si–PIN diode, were extracted from each 15 min spectra.

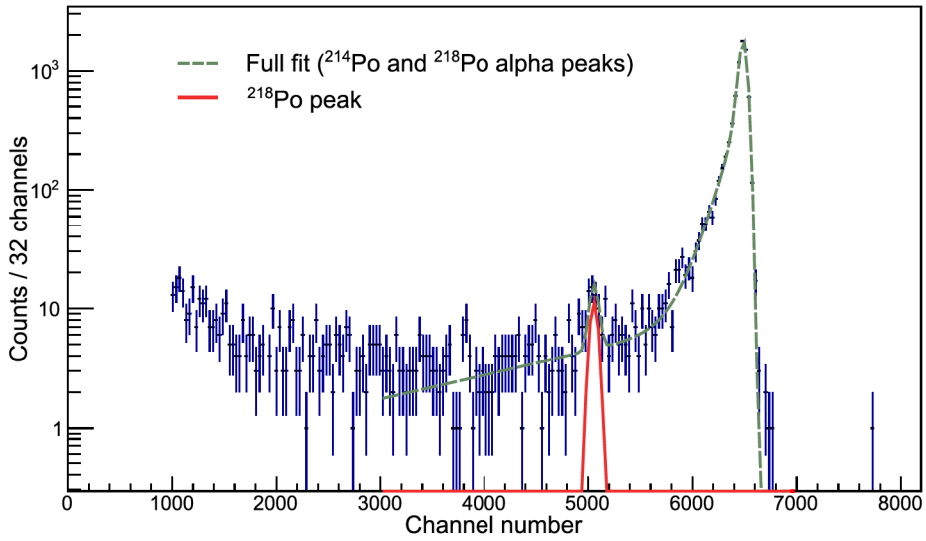

Figure 2.10: The alpha energy spectrum collected in a 15 min window, fitted with ^{214}Po and ^{218}Po peak shapes. The fit to the MCA channels 3000 – 7000 is shown in dashed grey line. The ^{218}Po energy peak, extracted from the fit, is shown separately in a solid red line. The fit range is limited to channel 3000 due to visible low energy background from beta decays. χ^2/ndof of the fit is 114.3/107.

Next, the count rates were corrected for ^{222}Rn decay (the measurements lasted much longer than the ^{222}Rn half–life) and liquid nitrogen boil–off (progressing concentration of the radioactivity due to liquid losses [viii]), which justified the use of the weight throughout the measurements.

The obtained time series of ^{214}Po and ^{218}Po alpha peak intensities, extracted from the data–sets (see Fig. 2.9), were then used to analyse the ionic properties relative to the applied electric field. The amount of collected ^{218}Po ions, visible directly as the registered signal in ^{218}Po peak, gives sole insight in the ^{218}Po ionic properties of α–decay origin. ^{214}Po activity, on the other hand, depends also on properties of ^{214}Pb and ^{214}Bi ions. The latter are not observed directly in the alpha detector (Si–PIN diode), while ^{214}Po short life–time prohibits drifting of the ions on any significant distances. Therefore ^{214}Po peak should rather be interpreted as originating from the collected ^{214}Bi and ^{214}Pb activities (^{214}Po decay following almost immediately the ^{214}Bi β^- decay).

2.2.4 Positive ^{218}Po ions produced in α–decays

^{218}Po cations are directly registered by the detector with positive high voltage bias applied to the housing of the cryostat. The electric field transports the cations towards the diode, being on the lowest (ground) potential relative to the housing. The transport starts immediately after they are created in ^{222}Rn decays. The geometrical efficiency of the detector (see Sec. 2.2.2) was used to estimate the collection efficiency of ^{218}Po ions. Fig. 2.11 depicts, as an example, ^{218}Po signal as registered after the removal of the high voltage bias (2 kV $\rightarrow$ 0 kV). Collection of the ions stops when the bias is removed, and remaining activity decays with characteristic ^{218}Po half–life time (3.1 min). Seven such observations were carried out throughout this study. The average registered signal from positive ^{218}Po ions (2 kV bias, 12.5 cm distance) was $A_{Po}^{218} = (128 \pm 6)$ mBq. Assuming the Si–PIN diode detection efficiency ε_{det} to be 50 % (what comes from a simple 2–π geometry), one can estimate the effective probability, at which ^{218}Po ions are created in the α decays of

[viii] It was shown during the ^{222}Rn doping procedure, that the boil–off nitrogen does not contain significant amounts of activity. Therefore no activity losses were expected to occur due to the boil off.

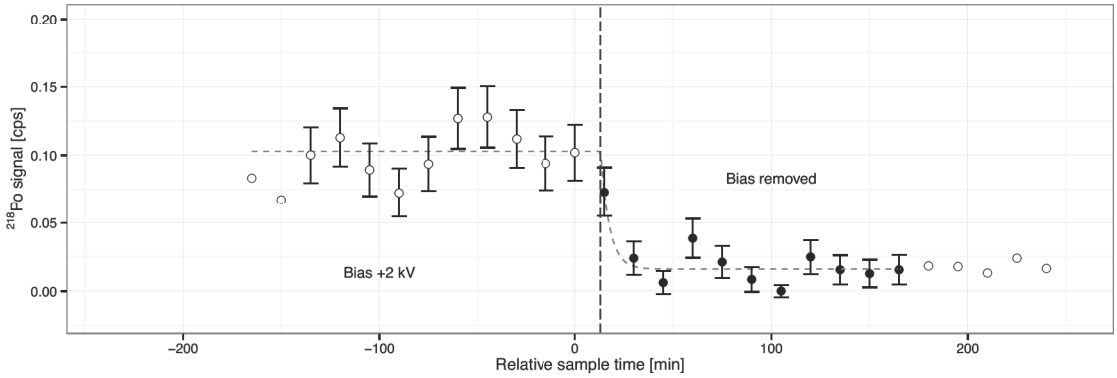

Figure 2.11: Fit to the ^{218}Po signal as registered on the Si–PIN detector in 15–minute samples. The vertical dashed line indicates the moment when the high voltage bias was removed (and the tank grounded). The moment of HV bias removal was not coincident with the time bins, therefore it was parametrized in the fitting (t_0). The curve parametrization was $y(t) = A_{218}\exp(-\lambda_{Po}t) + B$ for $t \geqslant t_0$ and $y(t) = A + B$ for $t < t_0$. The obtained values are $A_{218} = (87 \pm 6)\,\mathrm{mBq}$, $B = (16 \pm 4)\,\mathrm{mBq}$ and $t_0 = (13 \pm 1)\,\mathrm{min}$, for λ_{Po} being the ^{218}Po decay constant.

^{222}Rn:

$$\varepsilon_{218} = \frac{A^{218}_{Po}}{A} \cdot \frac{1}{\varepsilon_{col}\varepsilon_{det}} \approx 0.32 \pm 0.06\,\% \tag{2.20}$$

where A is the dissolved ^{222}Rn activity (16 kBq) in the tank volume V, and the estimated, E–field shape related, geometrical efficiency for collecting ions is $\varepsilon_{col} = V_{av}/V$. (The Si–PIN diode registration efficiency ε_{det} is related only to the ions decaying directly on its surface, while the geometrical efficiency V_{av}/V informs about the volume, from which the ions may reach the surface.) The uncertainty of ε_{218} (nearly 20 %) comes from the uncertainty of the dissolved ^{222}Rn activity A (10 %), and the systematic errors of the V_{av}.

This result indicates that ions produced in α–decays retain hardly any charge (very short ionic life–time) and thus do not contribute significantly to the total flux of charged ^{222}Rn daughters, drifted towards the detector. This observation is also supported by the analysis of ^{214}Po signal, presented in the following section.

2.2.5 Positive ^{214}Bi ions produced in β–decays

Range of ions and the maximum ionic life–time was determined in a dedicated measurement with the setup, where the maximum available distance for ions to travel was changed in several steps between 6.5 and 15 cm. For each diode position, no change in the registered ^{214}Po signal was observed. It means that the range of ions was shorter than the maximum available distance, and the ions were collected from the same volume, always smaller than V_{av} (thus the range of ions was not limited by the geometry). This observation led to the conclusion about the maximum life–time τ^{+}_{max} of the cations. The minimum available distance (range) of ions was $d = 6.5\,\mathrm{cm}$, in the average electric field $E = 300\,\mathrm{V\,cm^{-1}}$. Mobility of the ions, derived earlier for bismuth cations in liquid nitrogen ($\mu = 0.028\,\mathrm{mm^2\,V^{-1}\,s^{-1}}$), was used to estimate τ^{+}_{max} using Eq. 2.18:

$$\tau^{+}_{max} = \frac{d}{\mu E} < 77\,\mathrm{s} \tag{2.21}$$

The same result was obtained for ^{218}Po ions, but the signal was weaker and thus of smaller statistical significance.

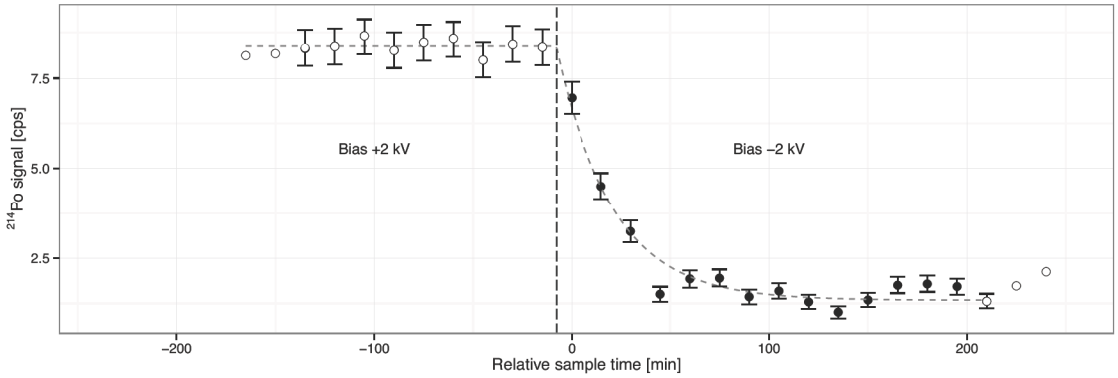

Figure 2.12: Fit to the ^{214}Po signal as registered on the Si–PIN detector in 15–minute samples. The vertical dashed line indicates the moment when the high voltage bias was reversed. The observed ^{214}Po signal is a direct measure of the collected ^{214}Bi activity (as the ^{214}Bi β–decay is followed immediately by the registered ^{214}Po α–decay). Time available for ^{214}Po cation collection is limited by it's short half–life (164 µs).

Collection efficiency of ^{214}Bi ions is more difficult to study, as the ion production and collection on the detector's surface is preceded by the two isotopes in the ^{222}Rn decay chain, i.e. ^{218}Po and ^{214}Pb. Knowing that only a small fraction of ^{218}Po atoms is accumulated from the liquid volume, it is reasonable to assume that the observed ^{214}Bi activity is supported at most by the ^{214}Pb ions, however these cations are also produced in α–decays of ^{218}Po. Therefore one expects similar, very low, yield of ^{214}Pb cations. Nevertheless ^{214}Pb activity was difficult to directly observe by the detector (β^- decays), and this channel was included in the following analysis.

Secular equilibrium of ^{222}Rn daughters gathered on the detector is reached after approximately 3 h, and the amounts of N^0_{Bi} and N^0_{Pb} will contribute to the registered ^{214}Po signal after the removal of ion drifting bias. Therefore the amount of ^{214}Bi ($N_{Bi}(t)$) may be modelled by a simple Bateman equation, relating observed ^{214}Bi signal to the initial amounts N^0_{Bi} and N^0_{Pb} (in secular equilibrium):

$$N_{Bi}(t) = \frac{\lambda_{Pb}}{\lambda_{Bi} - \lambda_{Pb}}(e^{-\lambda_{Pb}t} - e^{-\lambda_{Bi}t})N^0_{Pb} + e^{-\lambda_{Bi}t}N^0_{Bi} \tag{2.22}$$

where λ_{Pb} and λ_{Bi} are decay constants of ^{214}Pb and ^{214}Bi, respectively. The proposed function was fitted to the data to resolve composition of the ionic flux. Five measurements were carried out when the positive high voltage bias was removed (or the polarity reversed) after at least 3 h to observe the decaying ^{214}Bi activity. A fitting procedure returned (see Fig. 2.12), in each case, only upper limits on the ^{214}Pb abundances, while the average ^{214}Bi activity was $A^{214}_{Bi} = (7.1 \pm 0.1)$ Bq, hence

$$\varepsilon_{214} = \frac{A^{214}_{Po}}{A} \cdot \frac{1}{\varepsilon_{col}\varepsilon_{det}} \approx 17.8 \pm 1.8\,\%. \tag{2.23}$$

Relative amounts of ^{218}Po and ^{214}Bi observed on the detector reflect the predicted tendency, that cation production in β–decays is more efficient, compared to α–decays.

The limit on the amount of ^{214}Pb ions in the flux was also determined in the fitting procedures. The averaged upper limit is $A^{214}_{Pb} \leqslant 0.9$ Bq (with the mean value of $A^{214}_{Pb} = 0$ Bq). The outcome is therefore fully consistent with the result obtained for ^{218}Po ions, also created in α decays.

It is worth to make an attempt to link the collection efficiency estimated here, with the charge survival probability. The software written to compute the E–field lines closing on the detector surface (geometrical efficiency), was modified to compute the volume–averaged charge survival probability C/C_0 for a given $\xi \cdot E$ parameter introduced in Sec. 2.1.2. It was possible to find the corresponding $\xi \cdot E$ values for α–produced ^{218}Po and β–produced ^{214}Bi cations using the code. The respective values are $\xi_\alpha \cdot E = 121^{+13}_{-17}$ kV cm^{-1}

Distance [cm]	6.5	12.5	15
^{214}Po [mBq]	440 ± 50	800 ± 80	880 ± 100
V_{av} corrected [mBq cm^{-3}]	14.6 ± 0.7	5.1 ± 0.2	3.0 ± 0.1
V_{av} and mean E–field corrected [a.u.]	1.25 ± 0.06	1.46 ± 0.05	1.27 ± 0.06

Table 2.5: Maximum collected activity of ^{214}Po (^{214}Bi) as negative–like ions.

and $\xi_\beta \cdot E = 403^{+44}_{-55}$ V cm^{-1}, 26 % and 48 % of the values quoted before in Sec. 2.1.2 for similar energies released in α– and β–decays. The agreement is reasonable, also considering the fact that the cited values were obtained for different environmental conditions (i.e. different cryogenic liquids: in argon and in xenon, respectively).

2.2.6 Negative ions in the ^{222}Rn decay chain

Whether the ^{222}Rn progenies are negatively charged may be disputable. Isotopes in the ^{222}Rn decay chain do not exhibit significantly higher electronegativity values compared to e.g. oxygen (considered as the most abundant impurity component in the setup open to air). Also, the bulk of the cryogenic liquid is instantly depleted with, notably more mobile, electrons. However, observation of the α–activity of ^{218}Po and ^{214}Po on the diode indicated, that they were transported at least in the form of compounds with overall negative charge. Therefore the term 'negative–like' should be used.

The anion registration procedure was similar to the one used for observation of cations. Opposite polarization applied to the cryogenic container walls (typically -2 kV) repelled negative ions towards the detector. Activities of both ^{218}Po and ^{214}Po decays were clearly registered reaching, on average, (51 ± 1) mBq and (720 ± 10) mBq, respectively. That is 40 % and 10 % of the positive ions yield, respectively.

A dedicated measurement of the negative ion range was performed for three distances between the detector and the bottom of the cryostat. In such conditions clear dependence of the registered ^{214}Po signal (A^{214}_-) on the distance was observed (Tab. 2.5), contrary to the case of cations. To track the origin of the anions, Tab. 2.5 presents also the observed activities corrected for the available volumes (V_{av}) and the mean electric field strengths for the investigated detector — cryostat bottom distances. It is expected that the amount of the collected activity depends on the volume swept by the electric field (rather straightforward presumption), i.e. $A^{214}_- \propto V_{av}$. As the mechanism of negative–like ion creation is not determined here (most probably in a form of chemical compounds), the next assumption of A^{214}_- dependence on the mean electric field strength E emerges from the fact, that the speed of anion collection (efficiency) is proportional to the electric field, i.e. $A^{214}_- \propto E$. Once these corrections are applied, the registered activities agree within errors (given in arbitrary units). The lower limit on the negative–like ions is thus $\tau^-_{max} > 39$ s, assuming the mobility two times higher than the cation mobility. Along with such simple analysis, the activities of ^{214}Bi and ^{214}Pb in the anionic flux were extracted, taking advantage of the moments when the negative high voltage bias was switched off to move the detector. From the decay curves of ^{214}Bi (^{214}Po α's) the fitted values of ^{214}Pb in the ionic flux were extracted, and the mean value of ^{214}Pb activity is (470 ± 120) mBq, i.e. constitutes over 50 % of the total flux. This observation indicates, that the mechanism of negative–like ion production differs for the anions and cations, as in the former case (cations) ^{214}Pb was not observed (only the upper limit on the activity was found).

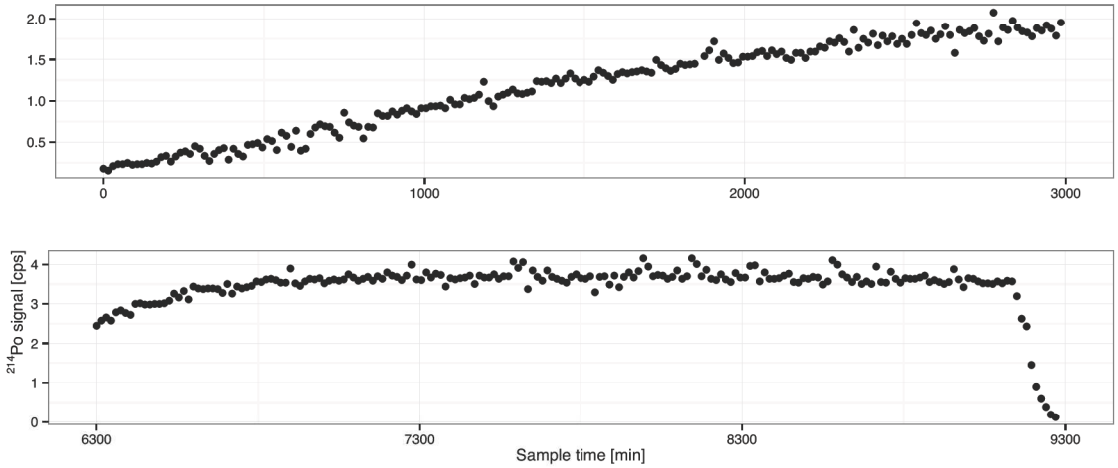

Figure 2.13: Long–term behaviour of the ^{214}Po signal (positive high voltage bias, cations collected), as observed at the beginning of each data–taking run. The two plots show two parts of the same measurement: the first 50 h, and 105 h to 155 h. All of the conclusions, presented earlier, are based on the data from the middle period of measurement time, when the registered signal saturates, i.e. when the registered signal reaches plateau (corrected for ^{222}Rn decay and LN_2 boil–off). E.g. the first measurement is signalled around 9000 min by a drop in the registered count rate (HV bias modification). A few outliers due to (rare) errors in automatic α peak shape fitting procedure (when the algorithm was unable to find reasonable fitting parameters) were excluded using the Mahalanobis distance criterion[ix].

2.2.7 Long–term properties – qualitative analysis

Apart from the determination of the basic ionic properties (both for the cations and the anions) the long–term behaviour of the signal from ^{218}Po and ^{214}Po (^{214}Bi) collected on the diode was studied. Already the first measurements were devoted to observe these long–term trends, as they were pronounced by the preceding measurements [86]. Over the several measurement periods, lasting at least 2 weeks, a constant increase of the registered signal was observed, with a maximum value of approximately 7 Bq for ^{214}Po α–activity. Fig. 2.13 presents this behaviour (as an exception, the dissolved activity of ^{222}Rn was half the usual amount). The observed long time constant can not be associated with any nuclear processes present in the ^{222}Rn decay chain.

Another possibility is that the impurity content of the cryogenic liquid was changing in time. While the cryostat was not pressurized, the chance of air impurities (oxygen, carbon dioxide, argon) dissolving in the liquid was not excluded. A very simple (qualitative) test was performed: using a low flow rate ($1\,l\,min^{-1}$) pump, air was introduced directly into the liquid, while the signal from ^{214}Po was constantly measured. As expected, after passing of 30 l of air through the cryogenic liquid (only a small fraction of air was dissolved, corresponding to approximately 10 ppm[x]), the registered signal immediately dropped (see Fig. 2.14). Next, it started to increase in the same fashion as observed in e.g. Fig. 2.13. It was concluded, that the charged impurity content, though high, in the presence of electric field operating for long periods of time, may be locally lowered.

An additional analysis, presented in [90], takes into account the long–term behaviour of the impurity content. It is assumed that the ionic life–time varies with the impurity concentration, which in turn obeys the limited growth law, as justified by the long–lasting measurements presented here. Over the long periods of time, the observed activity of ^{222}Rn was increasing after each high voltage bias change, while all other physical parameters of the measurement (including the bias potential and thermodynamic conditions) were ensured

[ix] http://www.encyclopediaofmath.org/index.php/Mahalanobis_distance
[x] ppm – parts per million.

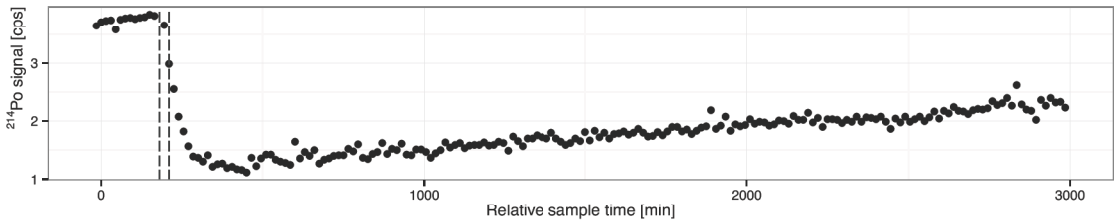

Figure 2.14: ^{214}Po signal behaviour after dissolving electronegative impurities (30 l of air pumped into the liquid in 30 min, as indicated by the dashed vertical lines). Increase of the signal is observed despite the additional impurities.

constant. The high voltage applied to the liquid nitrogen container acts like an ion sweeper not only for the radioactive cations. The distribution of electronegative impurities becomes also affected, resulting in a long–term effect of increasing ionic life–time of the ions (and decreasing impurity concentration). The impurities are drifted in the opposite direction to the cations. As they reach cryostat walls they remain attached to the surface. If there is no excess (external) source of impurities, equilibrium between the electro–induced cleaning drives to the equilibrium concentration of the impurities. Here the ionic life–time may be thus modelled by the limited growth function:

$$\tau(t) = \frac{\tau_0 \tau_{max} e^{rt}}{\tau_{max} + \tau_0 \left(e^{rt} - 1\right)} \tag{2.24}$$

where τ_0 is the minimum ionic life–time (initial maximum concentration of the impurities), τ_{max} is the maximum ionic life–time (minimal concentration of the impurities achievable in the setup), r is the change rate, the time–scale of the order of weeks. It was shown, that the ionic life–time varies from 0.1 s (τ_0) to 22 s (τ_{max}) for the ^{222}Rn progenies in liquid nitrogen. The change rate r is on the order of 10 d^{-1} [90].

2.2.8 Summary

An efficient method of direct ^{222}Rn daughters observation in liquid nitrogen was presented. The simple experimental setup allowed estimation of the **primordial charge recombination** probability for cations produced in α– and β–decays. As a consequence, $\xi_{\alpha,\beta} \cdot E$ parameters were estimated. It was also shown, that **negative–like ions may exist** in the cryogenic environment. Creation of such species is rather independent from the type of nuclear decay (α– and β–decays, producing ^{214}Pb and ^{214}Bi, respectively, are equally efficient in production of anions). It is important to note, that due to limitations of the experimental setup, some of the evaluated results present rather lower limits (like probabilities of cation production, minimum life–time of anions), or upper limits (maximum life–time of cations).

Some of these findings have been confirmed in the independent research focused on the ^{42}Ar/^{42}K background in the GERDA experiment (see Chap. 3).

2.3 Future studies of radioactive ions mobility

Due to some limitations of the used apparatus, it was not possible to investigate in detail the other properties of the ions in liquid nitrogen. It was necessary to design a new setup, suitable for studies of the single ions on their way in an electric field, from their origin to the surface of a detector.

The primary purpose of the setup was to investigate the deposition of various isotopes from the ^{222}Rn decay chain on different surfaces[xi]. Information about the temporal behaviour of ions was therefore irrelevant, and the setup was not optimized for such measurements. The new setup, developed later (in 2015) entirely in the frame of this PhD thesis, was intended for registration of the ionic flux in real–time versus changes of the drifting voltage (and polarity) and the distance. The main advantage of the setup was the uniformity of the electric field produced in the ion drifting chamber and significantly extended range, available to the ions (order of 1 m instead of 10 cm).

The drifting chamber allows investigation of the ion mobility μ (direct measurements) and the mean life–time of ions (through the mobility μ and the neutralization range λ). Neutralization range λ may be directly measured by varying the distance d to the detector:

$$\Phi = \lambda \Phi_i \exp\left(-d/\lambda\right) \tag{2.25}$$

where Φ is the surface density of specific ions (e.g. ^{218}Po or ^{214}Bi) surviving initial recombination and reaching the detector's surface. Such measurement yields also the fraction $\varepsilon_i = \Phi_i/\Phi_0$, namely the relative amount (density) of ions after initial recombination Φ_i, knowing Φ_0 – the activity of the ion source measured directly in an α spectrometer (in vacuum).

Mobility of the positive (negative) ions may be measured in the following procedure (see Fig. 2.15a): Positive ions are first removed from the drifting volume by applying negative (positive) potential, next the bias polarity is reversed. Positive (negative) ions are now drifted towards the detector. Depending on the applied bias U, the time ions require to drift towards the detector may be deduced from the registered activity build–up, starting when the first ion reaches the detector's surface. Knowing the distance, drift time Δt (interval between the bias polarity flip and the estimated beginning of the activity build–up) and the high voltage applied ($E = U/d$) the mobility may be estimated:

$$\mu = \frac{d^2}{\Delta t U} \tag{2.26}$$

The drifting chamber design concept is shown in Fig. 2.15a. The Teflon–made chamber is able to work in the cryogenic temperatures of the liquefied argon and nitrogen, and also in the gas phase. A set of electrodes coupled with a voltage divider on the outer surface of the chamber produces a uniform electric field. In the cryogenic environment, the localization of the resistors outside minimizes the impact of heat transfer from the divider on liquid stirring inside the chamber. The charge (sign) of the observed ions may be selected by the polarity of the high voltage bias applied. The bias potential (magnitude) influences the drift time t:

$$t = \frac{d}{v} = \frac{d}{\mu E} \tag{2.27}$$

where d is the drift distance (adjustable by the position of the ion source), μ is the ion mobility, and E – constant and uniform electric field strength. The inner volume of the drift chamber was isolated from the violent heat exchange or external liquid flows by construction, providing steady–state thermodynamic conditions. Depending on the neutralization time and mobility of the ions, different values of d (distance) and E (electric field strength) should be scanned to yield the value of ion mobility under investigation. Also, the total flux Φ of ions in a uniform E–field depends strongly on the neutralization time τ:

$$\Phi = \Phi_0 \exp\left(\frac{-t}{\tau}\right) = \Phi_0 \exp\left(\frac{-d}{\tau \mu E}\right) \tag{2.28}$$

where Φ_0 is the initial ion flux (of the produced ions). Therefore the registered signal is a function of the experimental geometry and the E–field strength. If the nuclear life–times of the investigated isotopes are longer than the expected neutralization times, they are not considered in the analysis (^{222}Rn daughters live on average longer than 180 s), while in the case of ^{220}Rn, the short nuclear life–time has to be taken into account (see Fig. 2.16).

[xi] See N. Frodyma doctoral thesis on ^{222}Rn daughters deposition on stainless steel, copper and germanium in liquid nitrogen and argon.

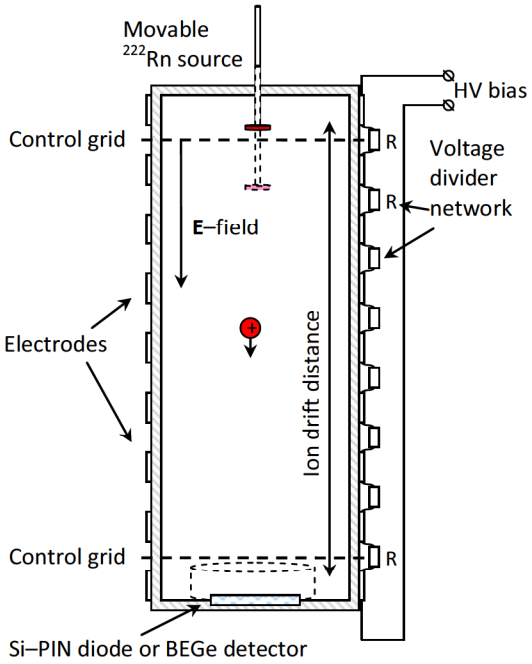

(a) A sketch of the drift chamber for radioactive ion investigation (not to scale). The chamber is made out of Teflon, height is 1 m, internal diameter 8 cm. The outer electrodes produce a uniform electric field inside the chamber, while the control grids allow to modify ion flux reaching the detector.

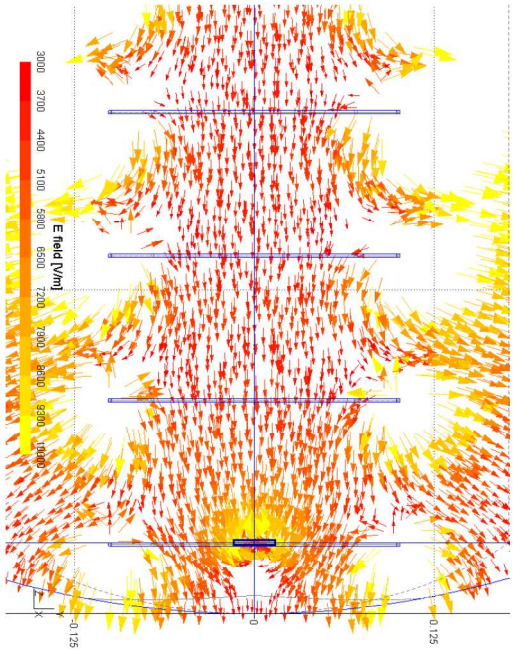

(b) A close–up of electric field calculation in vicinity of the Si PIN detector. The electric field lines are closing on the detector surface from the internal cylindrical volume of 5 cm in diameter. The ion source is facing the detector on the opposite end of the drifting chamber. E–field vectors displayed are limited to magnitude 10 kV m^{-1} for clarity.

Figure 2.15: The drifting chamber high voltage design and the respective electrical model.

In order to estimate the chamber geometric efficiency the shape of the internal electric field was studied (Fig. 2.15b). The electric field lines guide the ions, and those closing on the surface of the alpha particle detector determine the active volume of the chamber. Since the ion source is aligned to the detector, and its diameter does not exceed the active volume diameter (the central cylinder of 5 cm diameter), the geometrical efficiency of the chamber is 100 % in liquids [xii]. Combined with the known activity of the ion source, initial ion flux Φ_0 can be easily estimated in a fitting procedure.

The power supply used for the high voltage bias allows to apply up to ±30 kV. A new digital control module was also constructed to synchronize the data–taking with the (fully programmable via the USB interface) changes of the high voltage bias. The initial measurements showed that the setup is fully functional, and the energy calibration with large area Si–PIN diode (1 cm^2) was carried out with use of a ^{220}Rn source for future studies of the range and mobility of the short–lived ions (half–life of ^{220}Rn and ^{216}Po is 55.6 s and 145 ms, respectively). Fig. 2.17 shows the first α–energy spectra of the ^{220}Rn source in air, located 10 cm above the detector, as collected with −1.5 kV and 1.5 kV of the applied high voltage bias. The ion mobility in gases is high, therefore such low bias was sufficient to effectively drift the charged atoms, but the distance was short, as in air the ion life–time is highly suppressed by the presence of oxygen. The first observations indicated, that the ^{216}Po ions, produced in the α–decays of ^{220}Rn, are mostly positively charged (no ^{216}Po observed for the reversed polarity), and within their short life–time (145 ms), they are effectively drifted on significant distances (∼10 cm) in a relatively weak electric field (1.5 kV / 75 cm – 20 V cm^{-1}). The observed higher signal from ^{212}Bi and ^{212}Po α–decays (branching ratio of ^{212}Bi to ^{212}Po is 64 %, as observed in the presented energy spectrum) indicates, that at least ^{212}Pb or ^{212}Bi are also drifted towards the detector

[xii] The ions produced in liquids exhibit very limited range and thus their dispersion due to thermalisation may be neglected. In case of gases this effect has to be taken into account, affecting the overall geometrical efficiency.

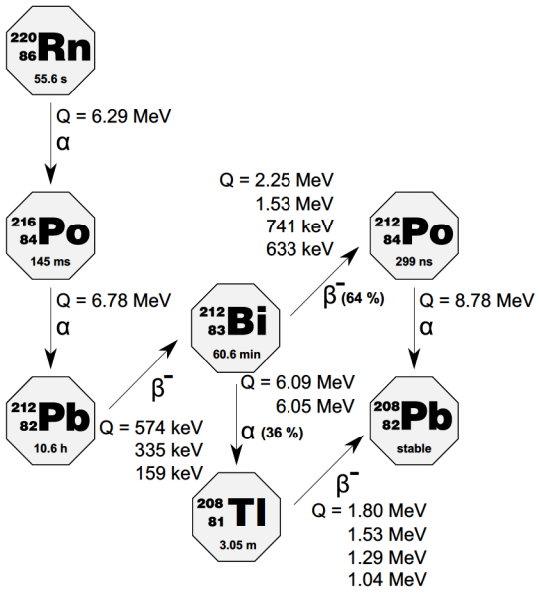

Figure 2.16: ^{220}Rn decay chain.

within their life–times.

The results obtained so–far may be considered as a 'proof of concept' and a good starting point for future measurements with the briefly presented setup.

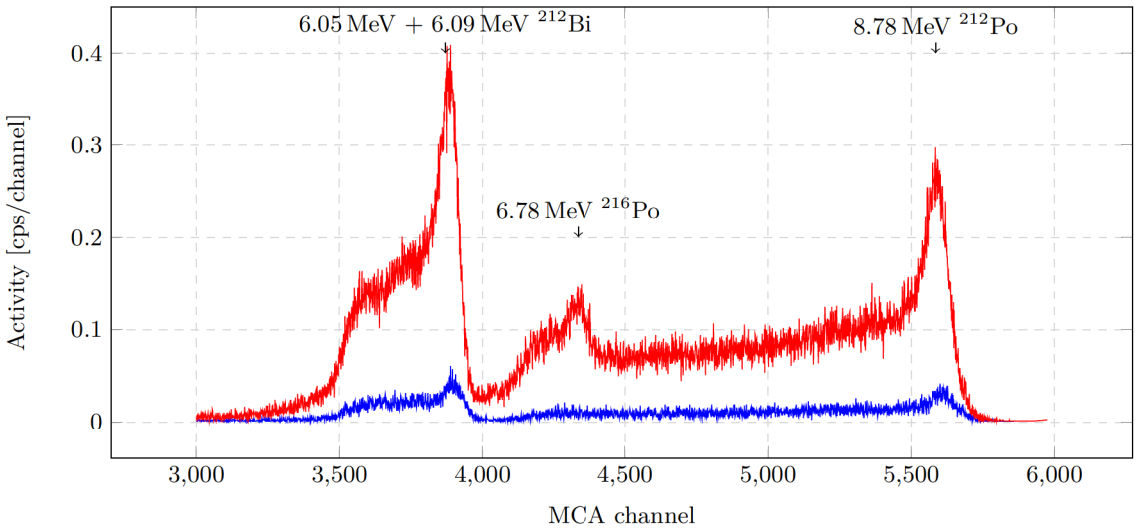

Figure 2.17: Upper part of the α–energy spectrum of the ^{220}Rn source, as registered for the two drifting voltages: −1.5 kV (blue) and 1.5 kV (red). The source was located 10 cm above the detector, in dry air (relative humidity 20 %) under ambient pressure (∼980 mbar). The α–peaks are broadened (Bi–Po coincidence) and exhibit low energy tails due to the experimental conditions. Registered were not only the decays occurring directly on the surface of the detector (main part of the peaks), but also some distant decays contributed with lower energies due to the α's stopping in the gas.

3

Radioactive ^{42}K in liquid argon – the Gerda experiment

3.1 LArGe

A dedicated setup (in the framework of Gerda) was used for studies of the background suppression methods for the Gerda experiment by means of liquid argon (LAr) scintillation detection or drifting of radioactive ions, induced by a high voltage bias.

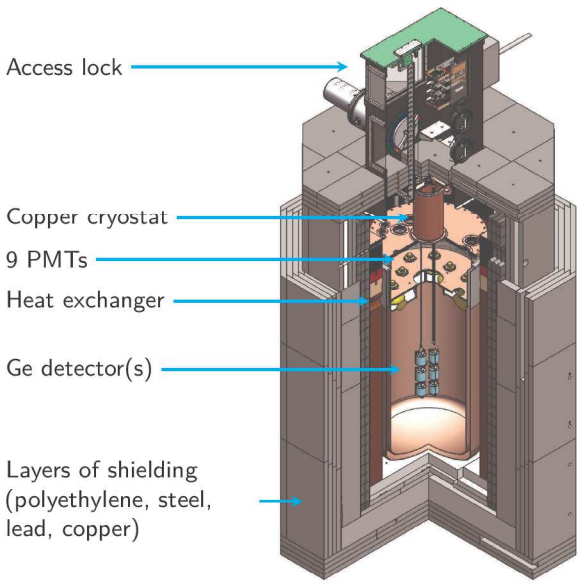

Figure 3.1: View of the LArGe setup revealing the graded structure of passive shielding.

LArGe (Liquid Argon and Germanium) is a cryostat adapted to operating bare high purity germanium (HPGe) detectors in a $1\,m^3$ of LAr in an ultra–low background environment. LAr is equipped with 9 photomultiplier tubes (PMTs, 8" diameter) detecting its scintillation light. The LArGe cryostat, shown in Fig. 3.1, is a double–wall vacuum–insulated vessel made from electrolytic copper and equipped with an active cooling system using liquid nitrogen (LN_2) as a cooling medium. The design of the LArGe shield is devised to have the gamma background dominated by the radio–impurity of the innermost copper layer ($< 19\,\mu Bq\,kg^{-1}$ of ^{228}Th). The copper itself was produced in close coordination with the manufacturer, which allowed keeping the exposure time for cosmic activation low ($< 10\,\mu Bq\,kg^{-1}$ of ^{60}Co). The relatively high content of ^{228}Th in the used carbon steel ($\approx 5.3\,mBq\,kg^{-1}$) led to an additional layer of low–activity lead ($< 22\,\mu Bq\,kg^{-1}$ of ^{228}Th) between copper and steel. Together, all three layers attenuate an external gamma from the 2.614 MeV line of ^{208}Tl to 5×10^{-8} of the initial flux. The installation of the shield has not been finalized yet. The steel layer was completed to 2/3 of its planned height, the lead shield to about half. The polyethylene layer was installed only at the bottom. The copper shield was fully closed with installation of the lock. The innermost layer (around a HPGe crystal immersed therein) is ≈41 cm of pure LAr (assumed for a centrally positioned Ge detector of 4 cm radius).

LAr in LArGe was instrumented with 9 photomultiplier tubes (PMTs). The PMTs detect scintillation light (after shifting the scintillation light wavelength from 128 nm to ≈460 nm by a dedicated VM–2000 foil, coated with TMB compound) of liquid argon, and they may be used to veto background events. By using

the LAr veto, background index was reduced to $< 10^{-2}\,\mathrm{cts\,keV^{-1}\,kg^{-1}\,y^{-1}}$, i.e. the design goal of Gerda Phase I.

Long–lasting measurements, performed with the LArGe setup, required a dedicated hardware control system for the stable and LAr loss–less operation of the cryostat. In the frame of the PhD thesis, the LArGe Slow Control system was designed and implemented to automatically keep the desired physical parameters of the LArGe cryostat within pre–defined ranges [91, 92]. The allowed pressure range inside the cryostat is specified by the design. The temperature of the liquid argon must be kept above the freezing point not to crack the PMTs. Additionally, the system was meant to aid the automatic operation of the set of 9 PMTs. The system amalgamates numerous hardware interfaces and different software techniques into one piece of software, responsible for supervising and control of the thermodynamic parameters, while maximizing the safety (including also automatic reporting of errors or warnings). Along with the safety, the system has to guard the stable operation of the cryostat during physics measurements while optimizing consumption of the coolant.

The slow control system consists of the software cooperating with hardware sensors (pressure, temperature, voltage, current, and weight gauges) and actuators (liquid nitrogen flow controller, high voltage power supplies). The software is logically composed of three components (Fig. 3.2): the control loop, the state database and the web interface. The control loop periodically reads out current values of the parameters of enabled devices, keeps the cryostat inner pressure in the allowed range based on the readouts by realizing the PID algorithm (Proportional–Integral–Derivative). The control loop also monitors currents and high voltages of the PMTs, and updates the state in the state database. The user is granted access to the current state stored in the state database via the web interface. The database keeps track of the parameter history. User commands to the slow control are passed also through the database and the web interface.

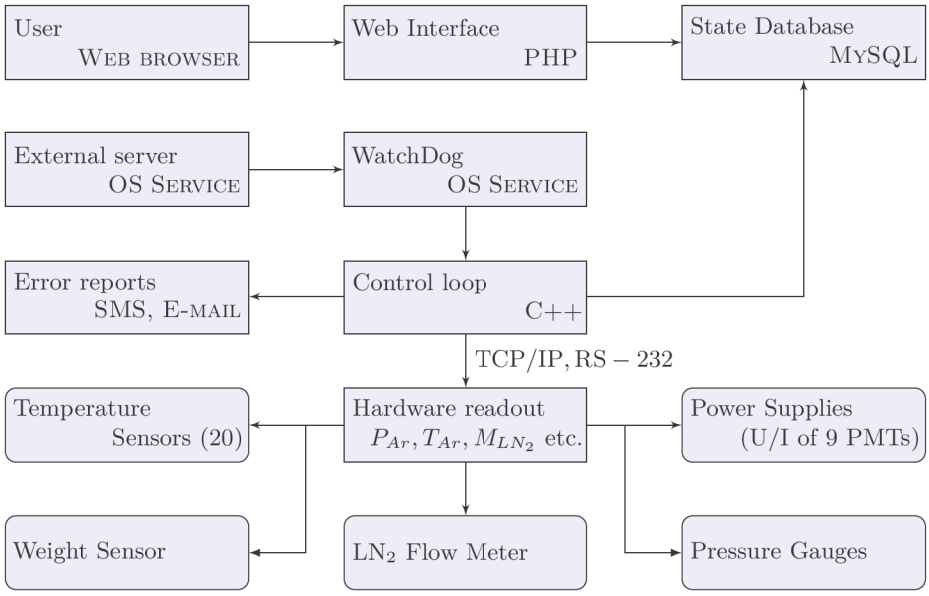

Figure 3.2: The Slow Control software consists of several distinct segments. Each piece of software code is responsible for a well–defined functionality within the slow control system. All connections are realized using TCP/IP protocols, except for the direct UART (RS–232) communication with the liquid nitrogen flow controller and the cryostat inner pressure gauges. Arrows indicate the direction of a connection initiation. As it can be seen, the user has no direct access to the control loop. The security of the system is ensured by the built–in mechanisms of the Apache WWW server and the MySQL database. Reliable interconnections are provided by the industry standards: Ethernet TCP/IP and serial RS–232.

The web interface is written in the PHP programming language (based on the Apache WWW server implementation). It allows the cryostat parameters to be easily monitored in the form of a colour coded diagram on a webpage. The page contents are updated automatically every 10 s using the Ajax technology.

An additional sub–page, password–secured, provides the interface for issuing commands to the slow control system. Firstly, the operator (user) selects the mode of the system operation, choosing between manual and automatic regimes of the cryostat pressure control. Secondly, it is possible to define the desired gas pressure inside the cryostat and alter parameters of the PID automaton. Independently, the interface allows for automatic or manual control of the PMTs high voltages. Each PMT channel may be programmed to raise or lower the high voltage in a given time period automatically. The upper limit of the current flow through the resistor voltage dividers is programmable as well. Such architecture permits for flexible access to the system from a variety of devices equipped only with a web browser, like personal computers, PDAs, tablets, or mobile phones, to name a few.

The displayed parameter values are also colour–coded. Whether a given value lays within the allowed range is the most important information, which should be easily readable not only to the trained operator, but also by bystanders outside working hours (e.g. security crew of the LNGS).

The state database is implemented in the industry standard MySQL environment. It consists of a few tables, collecting data about physical sensors (like the Ethernet addresses, unique names, state), allowed ranges for the physical parameters, history of the user commands or parameter values, and current system status for ease of querying.

The physical sensors are identified in the database by their unique name. Also, the connection parameters like the IP address in the local sub–network, or serial (COM) port number are stored along with the status of the device (enabled/disabled). The associated software interface to the device is also identified in the database by the unique class name.

The control loop periodically reads out the sensors using the interface objects instantiated during the system initialization, based on the information gathered from the database (abstract factory pattern). Each interface object is executed in a separate thread. The control loop verifies the sensor readings, and compares them with the predefined allowed range. Additionally, the state of the sensors is checked for errors, false readings, connection loss etc. The list below presents the variety of the controlled parameters:

- reserve of the liquid nitrogen (weight sensor, BOSCHE GmbH & Co. KG);
- LN_2 flow rate (for the active cooling, Smart–Trak® 2 Series 100 Mass Flow Meter);
- nitrogen heat exchanger input and output temperature (active cooling, Pt-1000, Web–Thermograph 8x, Wiesemann und Theis GmbH);
- cryostat inner pressure gauges (doubled, active cooling, Compact FullRange™ Gauge, Pfeiffer Vacuum and a spare, custom made pressure gauge);
- temperature sensors inside the cryostat – argon liquid and gas phase (active cooling);
- ambient temperature and pressure;
- copper shield inner pressure gauge;
- cryostat insulation pressure gauge;
- argon boil–off temperature at the safety valve;
- PMT voltage and current values (NIM NHQ x2xx High Voltage PSU, Iseg Spezialelektronik GmbH);
- server local time and client local time.

The read out values are stored in the database. The user commands are read out from the database and dispatched to the specific interface objects or to the control loop. After the command completion the user is acknowledged, and command state is changed in the database from PENDING to DONE.

Parameter	Minimum	Set point	Maximum	unit
Cryostat pressure	940	960	990	mbar
Piping temperature	4			°C
Vacuum insulation pressure			10^{-4}	mbar
Coolant flow rate	2	PID controlled	3	$m^3\,h^{-1}$
Weight of LN_2	50		354	kg
LAr level	-19	0	2	cm
PMT supply current			20	µA

Table 3.1: Allowed ranges of the physical parameters. The PID controller algorithm maintains the cryostat pressure at the set point value by varying the liquid nitrogen flow. It also asserts the cryostat pressure within the allowed limits in case of emergency. An overpressure may permanently damage the copper cryostat. (The typical ambient pressure value in the LNGS is 900 mbar). An additional argon shroud is installed (volume around the cryostat instantly flushed with boil–off argon). Liquid argon level is referenced to the PMT bayonets.

The most important parameters of the cryostat state are: the cryostat inner pressure, the liquid nitrogen (coolant) flow rate and the amount of liquid nitrogen. These values are additionally accented in the web interface. The design constraints of these values are summarized in Tab. 3.1.

The temperature sensors inside the cryostat are used to readout the LAr filling level by indicating the temperature differences between the argon boiling point under standard conditions (i.e. −185.85 °C) and the actual temperature readings. The positive deviation indicates that liquid argon level is below the sensor. Negative (or zero) deviation means that the liquid level is above the sensor position. It is mandatory to maintain the liquid argon temperature not lower than 1 K below the actual boiling point not to freeze the LAr.

The PID algorithm with the anti–windup protection controls the coolant flow in the active cooling system, based on the current and past cryostat pressure values. The low resolution of the cryostat pressure gauge (10 mbar) was improved by averaging (low–pass filter) of the sensor values in a running–average digital filter. The control value of the coolant flow $u(t)$ [$m^3\,h^{-1}$] is calculated periodically using the following expression:

$$\frac{u(t)}{K} = \left(e(t) + \frac{1}{T_i} \int_0^t \left(e(\tau) + \frac{T_i}{K T_t} w(\tau) \right) \mathrm{d}\tau + T_d \frac{\mathrm{d}}{\mathrm{d}t} e(t) \right) \tag{3.1}$$

where K [$m^3\,h^{-1}\,mbar^{-1}$] is the controller amplification constant, $e(t)$ [mbar] is the pressure error value (the difference between the set–point pressure value and the current reading), $w(t)$ [$m^3\,h^{-1}$] is the difference between the current ($v(t)$) and calculated ($u(t)$) liquid nitrogen flow rate. Time constants T_i, T_d, and T_t define response times of the integral, differential and anti–windup components, respectively. The algorithm is shown in Fig. 3.3.

The meaning of each block will be briefly described. The proportional part P (block K) is responsible for adjusting the controller signal $u(t)$ in direct proportion to the error $e(t)$. Based on the observation, value of K was estimated and set to $10^{-4}\,m^3\,h^{-1}\,mbar^{-1}$. The integral part I (1/s block) automatically corrects offset errors between the set–point value and the controller output, occurring over the time of operation. Time constant T_i is set equal to 15 min, again based on observation. An additional signal is fed to the I part – the anti–windup term (block $1/T_t$). This term prevents the integral part from ramping over (or below) the maximum (minimum) value of the allowed physical limits of the flow in case of big error values. In case of ramping over the limits, the pure I–term would need much longer time to return to the operational value (the physical limits of the flow controller) after the error is cancelled. In other words, this term avoids oscillation between boundary settings of the flow controller. The T_t, tracking time, describes the time needed to restore the I–part to the operating range. It is set to 10 min.

The derivative part (s block) improves the dynamic response of the controller by following the direction of $e(t)$ change over the time. The T_d time constant was determined based on the manual operation of the cryostat and set equal to 2 min.

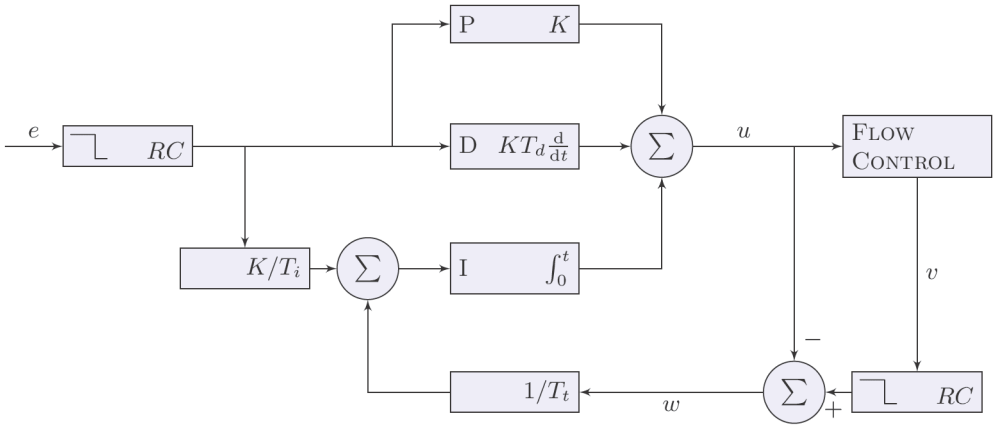

Figure 3.3: The PID controller algorithm. Signal e is the pressure error value (the difference of the set–point and the current values). Signal u is the control value (liquid nitrogen flow rate), while v is the real value of the flow rate. Signal w is the anti–windup variable, preventing the I–term from saturation beyond physical limits of the flow controller in case of permanent error deviation.

Error reporting is based on the watch–dog model. The slow control software is monitored by a custom–coded, built–in Windows operating system service (WatchDog). The service routine periodically polls the slow control program expecting a predefined response. The operating system, at the lowest software level, monitors the WatchDog for proper operation, and in case of failure, attempts to restart the service. Also, the WatchDog awaits Ethernet connections from external servers to monitor the quality of the network. If any of the checks fails (no response from the slow control program, failure of the service routine, no external connection from the external servers) an SMS error message is issued along with an e–mail notification to the predefined set of operators. The external server failing to connect to the WatchDog routine also reports an error (in such case the connection from the underground laboratory probably fails and such situation is considered a serious security threat).

Warning messages are also sent when the system recovers from errors or when an operator alters the normal program operation.

3.2 ^{42}Ar induced background in Gerda/LArGe

The progeny of long–lived ^{42}Ar isotope ($T_{1/2}$ = 33 y, Q = 0.6 MeV), ^{42}K, poses a source of possible background for observation of $0\nu\beta\beta$ decays in Gerda. The maximum energy of electrons in ^{42}K beta decays is 3.5 MeV, and the decay is accompanied by a weak γ–line at 2.424 MeV (both energies are above $Q_{\beta\beta}$). The β–decays of ^{42}K, occurring on the HPGe detector's surface, may mimic the $0\nu\beta\beta$ decays by their single–site character. Energy of the Compton events from 2.424 MeV γ–line may overlap the $Q_{\beta\beta}$ region. Therefore presence of ^{42}Ar (and consequently ^{42}K) was included in the background budget of the Gerda experiment. In the Monte Carlo simulations it was assumed that ^{42}K is homogeneously distributed over the liquid argon volume contained in the cryostat, like ^{42}Ar atoms[i]. Already the first measurements with immersed germanium detectors showed that ^{42}K gamma–line is much stronger than expected from the estimations. It became clear that either the concentration of ^{42}Ar in natural argon (^{nat}Ar) is higher

[i] 'If the choice of the liquid is argon, then additional background from ^{42}Ar decays have to be taken into account. The upper limit of the ^{42}Ar activity is 40 µBq kg^{-1} [Ash 03]. A simulation shows that this results in a background of $< 10^{-4}$ cts keV^{-1} kg^{-1} y^{-1}). Beta decays of ^{39}Ar have a Q value of 0.6 MeV and do not contribute to the background for neutrinoless double beta decay.' – from Gerda proposal to the LNGS P38/04.

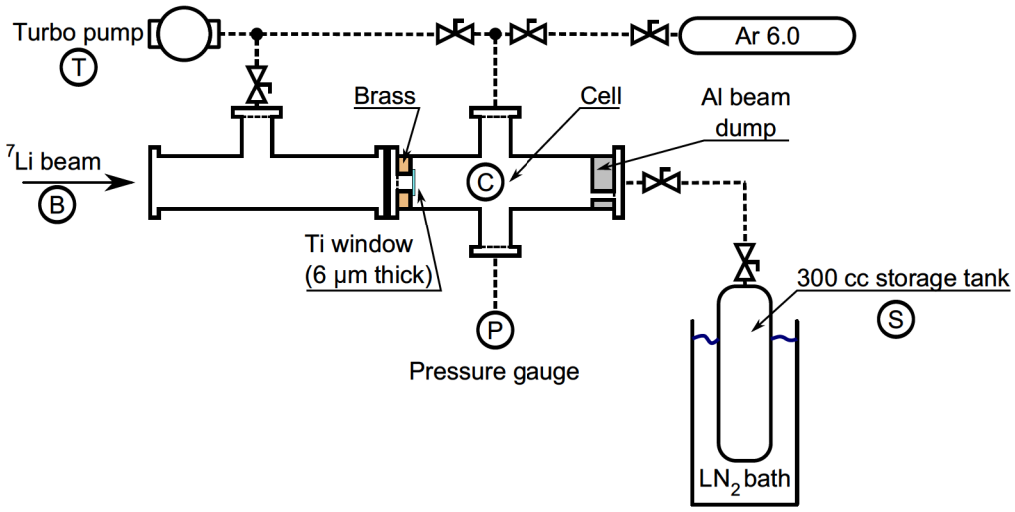

Figure 3.4: Schematics of the ^{42}Ar production experimental setup at MLL Garching. ^{7}Li beam enters the ^{42}Ar production cell from the left, passing through the thin titanium window. After the irradiation, enriched gas is transported into the storage tank (cryogenic pump using LN_2 bath).

than reported [93] or there is another process responsible for the increased ^{42}K activity close to the Ge detectors.

The observed prominent ^{42}K 1525 keV γ–line indicates the presence of ^{42}K atoms in vicinity of the Ge detectors. Therefore it was used as a marker in the ^{42}Ar/^{42}K studies. The hypothesis of increased ^{42}Ar concentration in ^{nat}Ar was easily rejected as the observed ^{42}K activity was varying in measurements with the high voltage bias applied to the Ge detectors. From this observation it was deduced, that ^{42}K is produced in the ^{42}Ar decays charged, and it's long life–time (17 h) allows the ions to be drifted in the electric field of the Ge detectors. Additionally, the high purity liquid argon used as a cryoliquid further improves the ionic life–time of ^{42}K ions, as the concentration of electronegative impurities is low.

Figure 3.5: The transport bottle (dashed yellow line) placed under the germanium detector. View from the top into the lead shielding used for screening.

By dissolving an additional ^{42}Ar activity in liquid argon (called spiking) it was possible to study the specific ^{42}Ar activity in natural argon in a model–independent way. Two sets of measurements were performed: the first series with natural argon, and the second with spiked argon (known added activity) in the same physical conditions. The natural abundance of ^{42}Ar could be measured through determining the ratio of registered ^{42}K 1525 keV γ–line strengths in the same hardware configuration for the natural and the spiked argon. Taking advantage of the spiked argon (almost 5 mBq l^{-1}), the collected data was used to estimate the ^{42}K cations life–time. Long term properties of the ionic flux were also observed (similar to the ^{222}Rn in liquid nitrogen described earlier) in over 60 measurements (lasting for 8 months).

An additional but known amount of ^{42}Ar had to be introduced into the cryostat in the procedure prepared by the LArGe team. This allowed to calibrate the measurements of the natural concentration of

Parameter	unit	Sample №1	Sample №2
Duration of irradiation	h	10.2	16.8
Averaged Li^{3+} beam current	nA	116 (6)	122 (8)
Beam energy	MeV	33	24

Table 3.2: Irradiation parameters of the ^{nat}Ar samples.

^{42}Ar in ^{nat}Ar. It was also useful in the studies of ^{42}Ar and ^{42}K ions, described here, thanks to the improved statistical error of the ^{42}K signal registered in the Ge detector.

Using the Tandem Accelerator at Maier–Leibnitz–Laboratorium (MLL) in Garching 10 Bq of ^{42}Ar activity was produced, stored in two separate samples [94]. Production of ^{42}Ar from ^{40}Ar (99.6 % of ^{nat}Ar) via reaction (^{7}Li, αp) was achieved with a $^{7}Li^{3+}$ beam hitting a gas cell target (Fig. 3.4).

The assembled system was evacuated with a turbo pump Ⓣ (cf. Fig. 3.4). Next, the volume of the cell Ⓒ was pressurized with 6.0 purity Ar gas up to 500 mbar. Pressure in the irradiation cell had to be lowered in order not to penetrate the thin titanium window due to pressure difference between the cell and the void accelerator pipe. The irradiation was carried out with ^{7}Li beam Ⓑ. Sample №1 was irradiated in several stages, totalling in 10 h 10 min of the beam time with an average 116 nA of the ion current. Sample №2 was activated without interruption within 16 h 45 min with 122 nA of the ion current (see Tab. 3.2). After the irradiation the gas was transferred to a storage tank Ⓢ, by cooling the tank down to the LN_2 temperature (a cryopump) – the majority of the gas condensed in the bottle in liquid form.

Screening of the samples was then carried out at Technische Universität München (TUM) underground laboratory with a low background germanium detector. The samples were enclosed in a lead shield, housing also the Ge detector (Fig. 3.5). MC simulation was performed to determine the geometrical detection efficiency of the screening setup (efficiency was 3 ‰ for the 1525 keV γ–line of ^{42}K). The activities of ^{42}Ar obtained in the sample №1 and №2 were (5.83 ± 0.97) Bq and (5.18 ± 0.91) Bq, respectively.

The produced activity from the sample №2 was introduced into the LArGe system. First, it was dissolved in the liquid argon, then transferred into the cryostat volume. After the operation was completed, the final concentration of added ^{42}Ar in LArGe was estimated to be $(4.8 \pm 1.0)\,\mathrm{mBq\,l^{-1}}$. Some amount of liquid argon evaporated during the operation, and had to be refilled afterwards, resulting in a slightly lowered concentration of the dissolved ^{42}Ar.

3.3 Measurements of the spiked liquid argon in LArGe

To effectively attract positive and negative particles, the coaxial germanium detector (GTF–44) operated in LArGe was equipped with additional 3 layers of encapsulation (see Fig. 3.6). The first, innermost layer made of PTFE (0.5 mm) isolated the second layer made of copper (1.5 mm). The copper served as a high voltage electrode, separated from the liquid by yet another layer made of PTFE (1 mm). The assembly provided an electrostatic isolation of the detector high voltage bias. High electric potential (bipolar) could be applied to the inner copper layer, not affected by the detector polarization voltage. A scenario with grounded encapsulation is called a 'semi field–free' configuration, as some parts of the detector bias wiring could not be effectively shielded.

The LArGe cryostat is also equipped with photomultipliers, biased by a high voltage (1180 V to 1540 V) when in use. During the measurements with the spiked argon they were not operated, in order not to influence the electric field shape generated by the detector encapsulation. Electric potential of the cathodes was kept at ground by the dynode voltage dividers and, in parallel, output resistors of the high voltage power supplies.

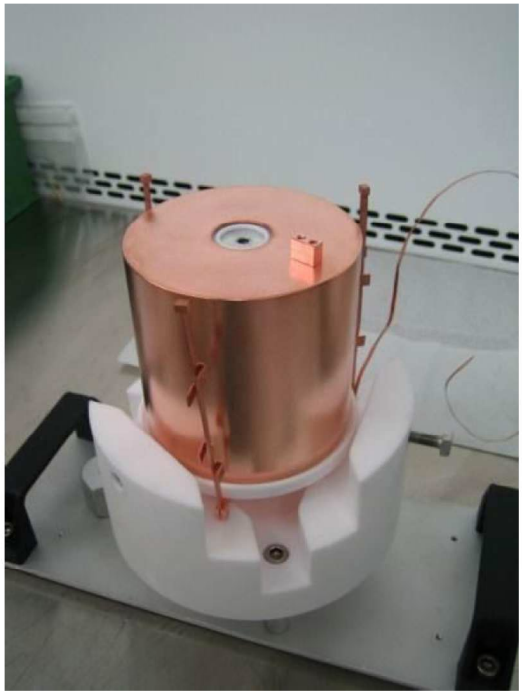

(a) Copper over the inner PTFE layer.

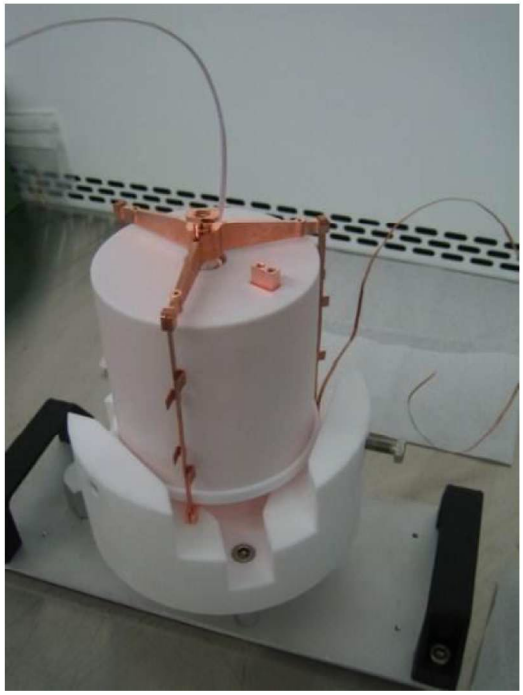

(b) Fully encapsulated detector.

Figure 3.6: Encapsulation layers on the GTF–44 detector. Images taken from [95].

A series of tests was performed with the encapsulation voltage ranging from 0 kV to −3 kV, in 500 V steps with the ^{42}Ar–doped argon[ii] [95]. Results obtained for these measurements were used to analyse the positive–only potassium ions life–time in the liquid argon, due to their high statistics. Fig. 3.7 shows the time evolution of the selected (combined) measurements at −3 kV and −2.5 kV, and separately in the range of −2 kV 0 kV. Long term increase of the registered ^{42}K signal is seen on an almost 3 month time scale (e.g. at −3 kV). Therefore the analysis should identify and take into account variations of the experimental conditions (in that case the liquid argon environment itself, as the thermodynamic conditions were under fully automatized control).

3.4 Modelling of the ^{42}K–induced background

Several factors, evaluated in the frame of the PhD thesis, had to be included in the calculation of the expected ^{42}K signal, registered by the GTF–44 coaxial detector in LArGe. These were: production probability of ionized ^{42}K atoms in β–decays of ^{42}Ar, transport of the cations in the electric field, and registration of the ^{42}K γ–decays in the HPGe detector. Additionally, the thermally driven convection in LArGe was computed, as both charged and neutralized ^{42}K could be transported in that way. Finally, ^{42}K atoms may be adsorbed on the surfaces of copper–made detector support structures or directly on the Ge detector (encapsulation), washed by the liquid flow.

[ii] Single measurements with (positive) 1.5 kV bias were also performed.

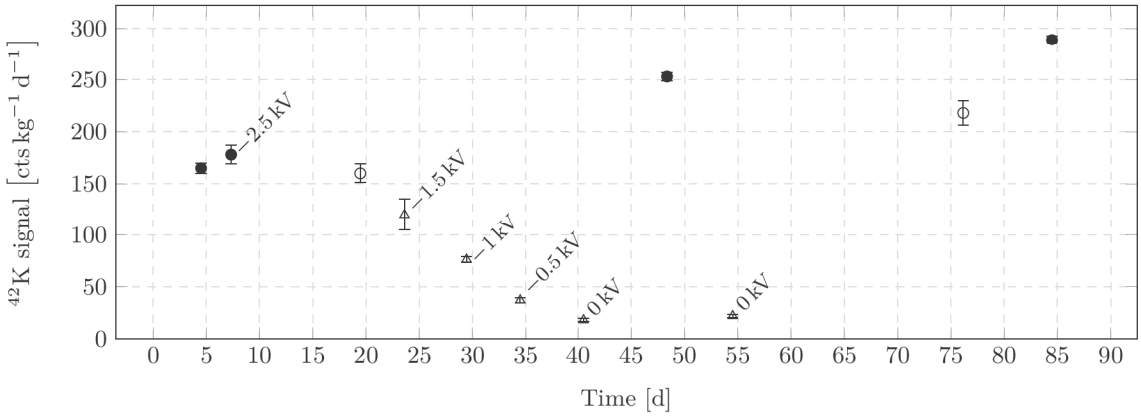

Figure 3.7: Time evolution of the registered ^{42}K signal as a function of the high voltage bias applied to the Ge crystal encapsulation; −3 kV and −2.5 kV (solid circles), −2 kV (empty circles), single measurements are annotated on the plot too (empty triangles). Growth of the registered signal is clearly observed for the measurements at −3 kV, −2 kV and 0 kV.

3.4.1 Monte Carlo simulations of the GTF–44 coaxial detector

Distribution of ^{42}K activity around the detector is pronounced by registration of the 1525 keV γ–line. Detection efficiency strongly depends on the geometry of the source and the detector, thus detailed simulations of the germanium detector response to the gamma–line were performed. A full 3D map of spatial detection efficiency was generated using the Monte Carlo code, called MaGe (Majorana–GERDA, embedded in GEANT4 modelling environment), developed jointly by the GERDA and Majorana collaborations.

The geometry of the LArGe cryostat and the Ge detector used in the study were implemented in the MaGe software in detail. In particular, physical dimensions, relative positions and materials of the construction elements were incorporated. The software allowed simulation of the detector's response to the external and internal sources of alpha, beta and gamma radiation. The observed energy spectra of different calibration sources (mainly ^{228}Th and ^{226}Ra) were compared with the spectra obtained in the simulation. The agreement was very good.

In the frame of the PhD thesis an additional modification of the MaGe software was implemented in order to track the positions of gamma emitting nuclei [96]. It was necessary to create the correspondence map between the gamma emitter position and the probability to register the quanta by the HPGe detector. Such volumetric map gave information on the efficiency of the whole detector setup for spatial (not point–like) radiation sources, such as volumetric distribution of ^{42}K ions. The map was then used in convolution with the computed ^{42}K activity distribution to infer the registered 1525 keV γ–signal.

The MaGe framework allows increased speed for the computation for large amounts of simulated events by forcing directionality of the emitted gamma quanta into the quadrant containing the Ge detector (the probability that a single γ, emitted opposite to the half–space containing the Ge detector, back–scatters and reaches the detector is negligible for distant locations). Thus this technique was exploited and over 1.3×10^{10} events were simulated to obtain the efficiency map with low statistical error in a short computational time.

The geometrical model of the LArGe cryostat was initially divided into small cubic cells (mesh accuracy 1 cm). In consequence, over 1.3×10^4 cm^{-3} decays were simulated. By tracking the origin of registered γ quanta it was possible to compute the efficiency for each cell accurately. The resulting files held x, y and z coordinates of the cell's centre, and the 1525 keV γ registration efficiency ε_{1525}. Cells with zero efficiency were the majority and were excluded from the data set (zero suppression technique).

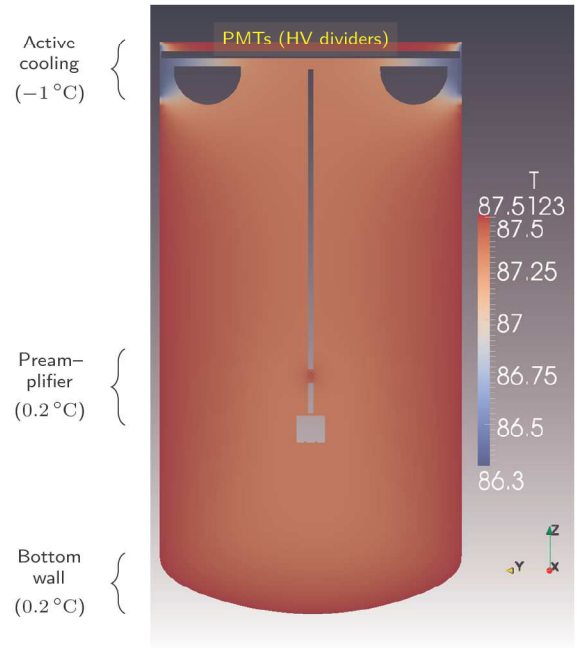

(a) Heat sources in the LArGe cryostat and the temperature distribution (colour map, shown in [K]). The main heat sources are placed at the bottom of the cryostat (in total ca. 100 W of heat load through the cryostat support pads) and in the preamplifier (∼0.1 W). Indicated are the approximate differences of the temperatures relative to the LAr boiling point.

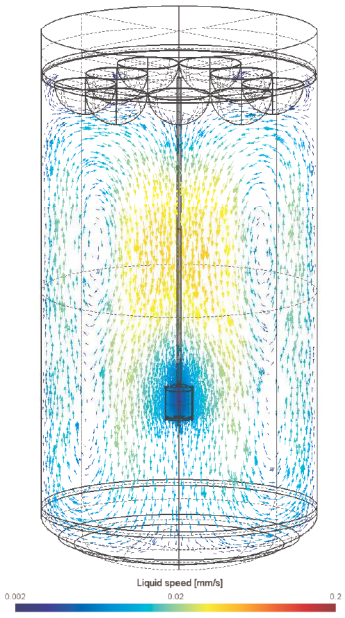

(b) Liquid argon speed distribution in the LArGe cryostat in [mm s^{-1}]. The stream lines are shown for the vertical cross–section of the cryostat. The flow is driven by the heat exchange between the walls of the cryostat and the active cooling system at the top.

Figure 3.8: Liquid argon convection in the LArGe cryostat. Heat load of the cryostat is compensated by the active cooling system. The system (controlled by the LArGe Slow Control) removes the heat to keep argon pressure constant.

Since the geometrical accuracy (and realistic dimensions) of the Ge detector model is below 1 cm of the cell dimension, the efficiency ε_{1525} in cells overlapping with the detector had to be corrected for the effective cell volume (excluded by the presence of the detector or its support structures). Such computation was done by a dedicated software by sampling the physical volume of the overlapping cells.

3.4.2 Thermally driven convection of the cryogenic fluid

Besides the motion in the electric field, cations (and neutral atoms) may be transported by the convection of liquid argon. This may have an impact on the background registered by the Ge detector. As an example, the electric field may attract the ions towards a steady–state streams of the cryogenic liquid. The ^{42}K activity in such a laminar stream may build–up, and if the flow rate is high enough, the ions (or neutralized atoms) may reach the vicinity of the detector before they decay. One has to consider the diffusion rate of atoms of interest, too. This mechanism is taken into account in the simulation code presented later in this chapter.

Studies of the liquid argon thermal convection in the LArGe cryostat were performed using the open source OpenFOAM [97] framework for computational fluid dynamics. The software incorporates also multiple tools to solve complex numerical problems, such as chemical reactions, turbulence and heat transfers, solid dynamics and complex electrodynamics. Full–size model of the cryostat was implemented as a multi–scale mesh, aiming at reproducing the most important details of the cryostat components. The three–dimensional model included 9 photomultipliers (PMTs) and their support copper plate, detector

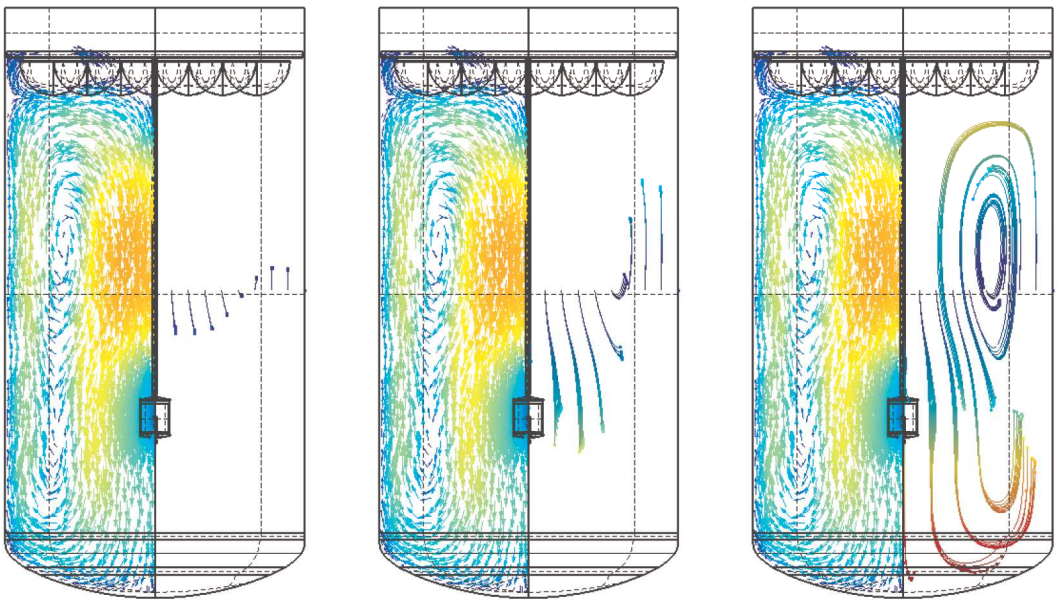

Figure 3.9: A set of time snap–shots of the neutral particle trajectories around the central part of the cryostat, calculated from the steady–state flow of liquid argon. A typical time scale for the argon stirring is 10 h, when the particles cover a distance equal nearly half of the cryostat height. The images show the neutral particle trajectories after 1 h, 5 h and 20 h (from left to right, respectively).

string, preamplifier, germanium detector, active cooling system and cryostat supports. The heat sources (cryostat walls, preamplifier, PMT high voltage dividers) and sinks (active cooling system) were modelled to reflect the total heat load of the system, known empirically from the operation of the active cooling system (see Sec. 3.1). The model was then used to generate a 3D mesh, consisting of more than 2×10^5 nodes, for the computation of the cryogenic liquid flow.

The package was tuned to determine the static laminar flow of liquid argon in the LArGe cryostat. The total heat load was known to be fully balanced by the active cooling system. The assumption was derived from the fact that the consumption of liquid nitrogen by the cryogenic system (responsible for the active cooling) was stable for significant periods of time (more than a year) with no loss of liquid argon (except when refilling or replacing the Ge detector). The thermodynamic parameters were instantly monitored and adjusted by the slow control system. The heat released in the sources is transferred by the liquid motion towards the heat exchanger, coupled with the active cooling system. The heat exchanger is placed at the liquid–gas phase interface.

The simulation code took 6 days to execute (140 hours of computation on a quad–core CPU). The temperature map was generated (cross–section shown in Fig. 3.8a), as well as the velocity field of the liquid argon (Fig. 3.8b). Heat from the cryostat bottom drives the liquid up, towards the active cooling heat exchanger. The stream is evenly distributed along the cryostat walls. The return path goes through the centre of the volume, where the liquid flux velocity is high[iii]. The heat released in the preamplifier (central part of the cryostat) counteracts the 'fall' of liquid, thus the liquid pattern spreads around the Ge detector. Fig. 3.9 shows the calculated trajectories of the neutral particles in the liquid velocity field. The average flow speed in the central part of the cryostat (close to the detector) equals $0.2\,\mathrm{m\,h^{-1}}$. The speed of ^{42}K ions, solely due to the electric field (assuming no liquid flow), is on average $0.4\,\mathrm{m\,h^{-1}}$. As both values are comparable, the convection of liquid argon had to be included in the the final calculations.

[iii] Obviously, liquid argon is treated as incompressible.

3.4.3 Chemisorption of potassium on copper, germanium and PTFE

GTF–44 detector was operated in LArGe in the support structure and encapsulation made of copper and PTFE. Therefore, it was relevant to study whether the ^{42}K atoms could be efficiently deposited on the Cu surfaces once neutralized in contact with the conductor. Additionally, germanium was included in the computations, as the HPGe detectors in Gerda are also operated naked. A ^{42}K ion preserves its charge in contact with the surface made of non–conducting PTFE, therefore the calculations of the bonding energy for the PTFE surfaces were not performed (also due to the complicated structure of the PTFE compound). It is assumed that the electrostatic force, induced by the high voltage copper electrode, holds the ^{42}K cation at the PTFE surface.

Depending on the strength of atomic bonding, adsorption is regarded either as physisorption ($E_{bond} \leq 0.1\,eV$, characteristic for noble gas adsorption, molecular adsorption through Van der–Waals interaction) or chemisorption ($E_{bond} \sim 1\,eV$ to $10\,eV$, characteristic for chemical bonds between a surface and an adsorbate). If the bonding energy is less than the thermal energy (k_BT), then bonding is not sufficient to hold the adsorbed atom in position. Presence of other atoms (liquid argon) is also reducing the possibility of adsorption as most of the sites at material's surface are occupied. Modelling of ^{42}K physisorption on copper and germanium surfaces is presented here, performed in the Atomistic Simulation Environment (ASE, [98]). The calculations were required as the experimental values of adsorption energies of potassium on copper and germanium surfaces were not available.

A toy model of Lennard–Jones (L–J) potential was constructed for interactions between the liquid atoms (argon), potassium and both copper and germanium surfaces[iv]. For a comparison, radon was also included in the calculations. The ASE environment was used to construct the surfaces, ordered in the face centered cubic (FCC) [111], [110] and [100] crystal structures (Cu) and the diamond (DIA) [111] and [100] faces (Ge). Depending on how an FCC crystal (copper) or diamond (germanium) is cleaved, these five surface configurations are exposed to adsorb atoms in the microscopic scale. The crystal dimensions (number of atoms) was chosen to be $8 \times 8 \times 5$ (see Fig. 3.10), ensuring that within the cut–off range of the L–J interaction lattice atoms are present. Next, an adsorbed atom (Ar, K, Rn) was thermalized on the solid surface to find it's equilibrium position. Temperature of the system was fixed to 86 K, corresponding to 7.41 meV.

Tab. 3.3 summarizes the results of adsorption energy calculations for different surface structures. In the macroscopic scale it is assumed that each of the structures is observed with equal probability, thus the average adsorption energy is given for each adsorbent type (Cu and Ge). The values obtained are used in the following estimation: having computed the adsorption energies, it is possible to estimate the probability that an atom freezes out on a copper (or Ge) surface in presence of liquid argon by calculating the Boltzmann factor $B_{K\to Ar}$:

$$B_{K\to Ar} = \frac{F_{\mathrm{Cu+K}}}{F_{\mathrm{Cu+Ar}}} = \exp\frac{\Delta E_{\mathrm{ads}}}{k_BT} \tag{3.2}$$

In the above equation, F_{Cu+Ar} and F_{Cu+K} denote the thermodynamic states, in which Ar or K atoms are adsorbed on Cu surface, respectively. ΔE_{ads} is the energy difference of the states, and T is the system temperature. The Boltzmann factor may then be interpreted as the probability of the exchange between Ar and K atoms adsorbed. In the proposed L–J model potassium is more bound, and the Boltzmann factor is 0.0045. As the probability $B_{K\to Ar}$ is low, once the potassium atom is adsorbed on copper, it is unlikely to be replaced by an argon atom. Similar result was obtained for the germanium surface, so in the simulation of ^{42}K behaviour in liquid argon, it is assumed that the potassium ion reaching copper or germanium surfaces, remains permanently bound.

[iv] More complex potentials should be in fact used, such as three–body potentials for Cu and Ge crystal structures, to perform detailed studies, which are beyond scope of this thesis, and should be the subject of future efforts.

Adsorbent surface	Potassium (K)	Argon (Ar)	Radon (Rn)
Cu FCC[111]	0.53	0.50	1.06
Cu FCC[110]	0.65	0.59	1.10
Cu FCC[100]	0.57	0.53	1.06
Copper average [eV]	*0.58*	*0.54*	*1.07*
Ge DIA[111]	0.60	0.54	0.98
Ge DIA[100]	1.15	0.97	1.50
Germanium average [eV]	*0.88*	*0.76*	*1.24*
L–J σ [Å]	3.13	3.40	4.36
L–J ε [eV]	0.014	0.010	0.024

Table 3.3: Adsorption energies of K, Ar and Rn on different surfaces, expressed in eV. Parameters of the Lennard–Jones (L–J) potential model are given for the selected elements, used to estimate the adsorption energies. Lattice parameters and interaction constants of Cu and Ge are built in values of the ASE package.

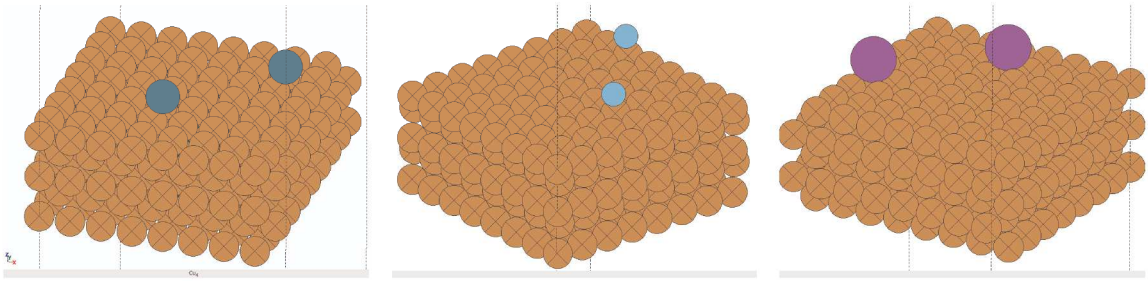

(a) Radon **(b)** Argon **(c)** Potassium

Figure 3.10: Visualisations of the ASE simulations for adsorption of radon, argon and potassium on the copper surface, respectively. Atomic radii drawn are proportional to the van der Waals radii (see Tab. 2.2).

3.4.4 Ionic properties of ^{42}K cations

The model for drifting ^{42}K ions in the liquid argon in presence of the electric field includes several mechanisms influencing the ^{42}K ion flux. These are: *primordial recombination* of positively charged ^{42}K ions, *bulk recombination* on electronegative impurities (see Eq. 2.13), diffusion (mobility dependant), *time–varying concentration of the impurities* (directly related to the effective ionic life–time), and nuclear decay of ^{42}K atoms.

The primordial recombination of ions may be described by the $\xi \cdot E$ parameter (see Eq. 2.10), relating the probability of the initial charge retention on the external electric field strength immediately after the act of a nuclear decay. The parameter $\xi \cdot E$ depends on the nuclear decay type (short ionization range and high density in α–decays, long range and low density in β) and the bulk material (cryogenic liquid). Cations created in β–decays are very likely to remain charged (typically 10 %). It is also expected that for higher $\xi \cdot E$ values, the ionic life–time (bulk recombination) should also increase in order to yield the same flux of ^{42}K ions. Therefore uncertainty in $\xi \cdot E$ translates to the uncertainty in the ion life–time.

Impurities in LArGe As it can be seen in Fig. 3.7, 1525 keV γ count rate enhances in time for a particular high voltage applied to the detector's encapsulation. The ingrowth lasts for almost 3 months. Temperature and pressure of the liquid were ensured constant over the measurement period by the slow control system. Slight overpressure in the cryostat, combined with the shroud covering the whole setup and continuously flushed with fresh boil–off argon, ensured that no external impurities could enter the liquid argon volume.

Algorithm 1 ^{42}K Multiphysics Simulation. Some parameters (e.g. $T_{1/2}$ – half–life of ^{42}K) are fixed in the simulation code. Other, like initial (dissolved) ^{42}Ar activity A, efficiency map ε_{1525} (geometry dependent), ^{42}K mobility μ, electric configuration and geometry $\vec{E}$, thermal flows $\vec{w}$, ^{42}K ionic life–time τ and maximum simulated time t_{max} are input for the algorithm. The code is optimized and paralleled, e.g. some loops over set of atoms are amalgamated.

procedure MAIN($A, \varepsilon_{1525}, \mu, \vec{E}, \vec{w}, \tau, t_{max}$) ▷ Input parameters
  $t \leftarrow 0$ ▷ The time
  $K \leftarrow$ DECAYSARGON($A, T_{1/2}/\log 2, \tau$)
  NEUTRALIZE($K, T_{1/2}/\log 2, \tau$)
  while $t \leq t_{max}$ **do** ▷ Time stepping until t_{max} reached
    $K \leftarrow K \cup$ DECAYSARGON($A, \Delta t, \tau$)
    NEUTRALIZE($K, \Delta t, \tau$)
    $S \leftarrow$DECAYSPOTASSIUM($K, \Delta t, \varepsilon_{1525}$) ▷ Signal at the time t
    TRANSPORT($K, \Delta t, \mu, \vec{E}, \vec{w}$)
    $t \leftarrow t + \Delta t$
    print t, S

function DECAYSARGON($A, \Delta t, \tau$) ▷ Creates a new set of ^{42}K atoms
  $K \leftarrow$ number of atoms with total activity $A\Delta t$ ▷ New set of ^{42}K atoms
  for all $k \in K$ **do**
    k.position $\leftarrow$ random (uniform) inside geometry
  return K ▷ Newly produced ^{42}K atoms (all charged)

function DECAYSPOTASSIUM($K, \Delta t, \tau$) ▷ Signal S from decaying ^{42}K atoms
  $S \leftarrow 0$
  for all $k \in K$ **do**
    if k **decays** within Δt **then**
      $S \leftarrow S + \varepsilon_{1525}(k.\text{position})$
      remove k
  return S

procedure NEUTRALIZE($K, \Delta t, \tau$) ▷ Neutralize ^{42}K cations
  for all $k \in K$ **do**
    if k **is** charged **then**
      k.charge $\leftarrow$ neutral w.r.t. τ (bulk recombination)

procedure TRANSPORT($K, \Delta t, \mu, \vec{E}, \vec{w}$) ▷ Transport of atoms
  for all $k \in K$ **do**
    if k **is not** fixed **then**
      k.position $\leftarrow$ RK–4 updated position ▷ See Eq. 3.7a
    if k **is** outside geometry **then**
      adjust Δt appropriately
      k.position $\leftarrow$ fixed (at the boundary) ▷ Atom deposited on a surface

Some time after the measurements, the cryostat was opened to replace the Ge detector. After that procedure the electronegative impurity content was measured at the level of 2 ppm (oxygen equivalent for all electronegative impurities) in the mixed[v] liquid argon.

The only source of impurities could be assigned to outgassing of the materials inside the cryostat. Nevertheless, the observed ^{42}K signal behaviour is more related to improving liquid quality (purity). The mechanism was already mentioned in Sec. 2.2.7. As the high voltage bias acts also on electronegative impurities, the anions[vi] are drifted away from the active volume of the detector. Purity of the liquid may be enhanced locally and, consequently, ionic life–time increases. In case of no significant sources of impurities, equilibrium concentration of the impurities (i.e. the spatial distribution) is reached (while the total content of impurities is rather constant). Such behaviour was already observed in the Icarus experiment [99], where the free electron life–time in ultra–pure argon was also observed to improve over time.

The ion life–time τ depends on the impurity concentration, and may be expressed as (see Eq. 2.13):

$$\tau = \frac{M}{[Z^-]} \tag{3.3}$$

where $M \approx 10\,\mathrm{min} \cdot \mathrm{ppm}$ (it will be shown later, that the typical τ is 20 min for the uniform distribution of impurities). Considering the temporal concentration of impurities $[Z^-](t)$, it may be expressed as:

$$[Z^-](t) = \frac{A}{B - \mathrm{e}^{-\kappa t}} \tag{3.4}$$

where A/B is the equilibrium impurity content (the final value; A is expressed in ppm), $A/(B-1)$ is the initial impurity concentration (at $t = 0$), and $1/\kappa$ is the typical time–scale of the process. From the mass spectrometry measurements, $A/(B-1) \approx 2\,\mathrm{ppm}$. The time constant κ and the final impurity concentration will be later determined through the data analysis.

Potassium mobility in liquid argon Due to large atomic polarizability of argon atoms, potassium cations are encapsulated in atomic clusters, stacked by electrostriction in layers around the central cation. In such conditions the ion transport is mainly determined by the hydrodynamics of the structure. In the Stokes regime, the mobility μ depends on the cluster radius and the liquid viscosity (see Eq. 2.8), and not on the ionic species (except for the ionic radius, as discussed before). In strong external electric fields, the cluster radius may be reduced, as the outermost layers of the polarized atoms become stripped off by shear forces. Different measurements show values of ion mobility in liquid argon ranging from $0.02\,\mathrm{mm^2\,V^{-1}\,s^{-1}}$ [75] to $0.06\,\mathrm{mm^2\,V^{-1}\,s^{-1}}$ [100]. The difference may be explained by a variable number of clustered layers of neutral atoms. Possibly smaller values of the mobility, extrapolated to the null external electric field, imply the presence of two atomic layers around the cation. Higher values correspond to one layer of surrounding atoms. Potassium ions in liquid argon are therefore assumed to exhibit maximum observed mobility of positive ions of similar size, i.e. $0.06\,\mathrm{mm^2\,V^{-1}\,s^{-1}}$, as in the worst case scenario.

For a comparison, a theoretical value based on Eq. 2.8 is computed assuming singly ionized potassium atom surrounded by one layer of neutral argon atoms. Liquid argon viscosity under normal pressure is $2.695\,\mathrm{mg\,cm^{-1}\,s^{-1}}$, atomic radius of argon is 1.88 Å, and covalent radius of potassium (see Tab. 2.2) is 2.03 Å; therefore $\mu = 0.05\,\mathrm{mm^2\,V^{-1}\,s^{-1}}$.

Diffusion processes Both neutralizing agents and cations of interest diffuse into the cryogenic liquid, independent from the electric field applied. The three–dimensional Brownian motion describes the diffusion process, in which the average distance σ, travelled by a particle in time t, is:

$$\sigma = \sqrt{6Dt} \tag{3.5}$$

[v] Mixing was caused by the operations of detector replacement, during which warm crystal was immersed in the liquid argon.
[vi] Anion life–time is significantly longer than cations'.

where D is the diffusion coefficient, expressed through the ion's mobility μ and charge q, following the Einstein's relation, as:

$$D = \mu \frac{kT}{q} \tag{3.6}$$

In the cryogenic liquids, the motion caused by the electric field, combined with the convection flows, may be regarded as dominant. The chosen value of mobility ($0.06\,\mathrm{mm^2\,V^{-1}\,s^{-1}}$), yields the diffusion constant D equal $4 \times 10^{-4}\,\mathrm{mm^2\,s^{-1}}$. The average distance σ, travelled within 20 min, is then equal 1.7 mm.

Nevertheless the process is included in the model, because the strong electric field is not spread over the entire considered cryostat volume. What is more, the thermally driven liquid flows, being laminar, do not cover the full volume of the cryostat, leaving some parts intact. Therefore the diffusion may be the only possible way for atoms (including radioactive ions) to approach the detector (e.g. by first travelling closer to the volumes of high E–field or by entering the convective fluxes).

3.4.5 Numerical implementation of the ^{42}K model and results

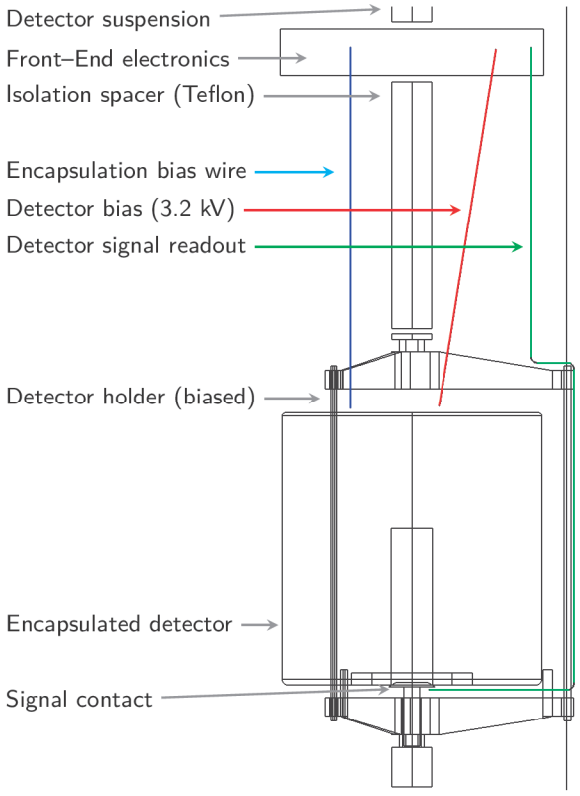

Figure 3.11: Diagram showing the high voltage biasing configuration close to the encapsulated detector. The detector suspension (string) is grounded (or at near–to–ground potential), likewise the electronic front–end box, and shielded signal readout cable. Detector bias is required for proper detector operation, encapsulation bias (applied also to the copper–made detector holder) initially was not shielded.

The numerical ^{42}K model incorporates formerly described components of the physical system, such as ion mobility (in E–field) and diffusion, neutralization, liquid thermal convection and radioactive decays, into a computational procedure. Spatial data required for the computation is pre–calculated (electric field shape for different bias schemes, liquid convection, detection efficiency of the 1525 keV ^{42}K gamma–line) in a dedicated software.

To calculate the expected ^{42}K signal, the simulation is performed in time domain divided by equally spaced time–steps. In each time–step (Δt) a number of ^{42}K ions is produced in decays of ^{42}Ar (accordingly to the dissolved ^{42}Ar activity, which is known). The ions created in ^{42}Ar decays are initially uniformly distributed. Next, the time–stepping algorithm (4th–order Runge–Kutta integration, RK–4) is applied to compute the ion's displacement due to the presence of the electric forces (velocity is derived from the ^{42}K mobility μ), diffusion and the liquid flows.

The electric field distribution is obtained from the detailed model of the LArGe cryostat (GMSH and GETDP software introduced earlier; see Fig. 3.11 and Fig. 3.12), while the liquid velocity at the given vertex was calculated in a dedicated software (OpenFOAM). In case of ^{42}K ion decay, the expected signal in the detector is enhanced by the fraction deduced from registration efficiency ε_{1525} at the given vortex (detection efficiency map). A neutralized atom is only a subject to the liquid flow motions and the diffusion. The integration scheme (RK–4) is modified to properly treat the very likely situation, in which the ion is directly drifted to the surface of the Ge detector,

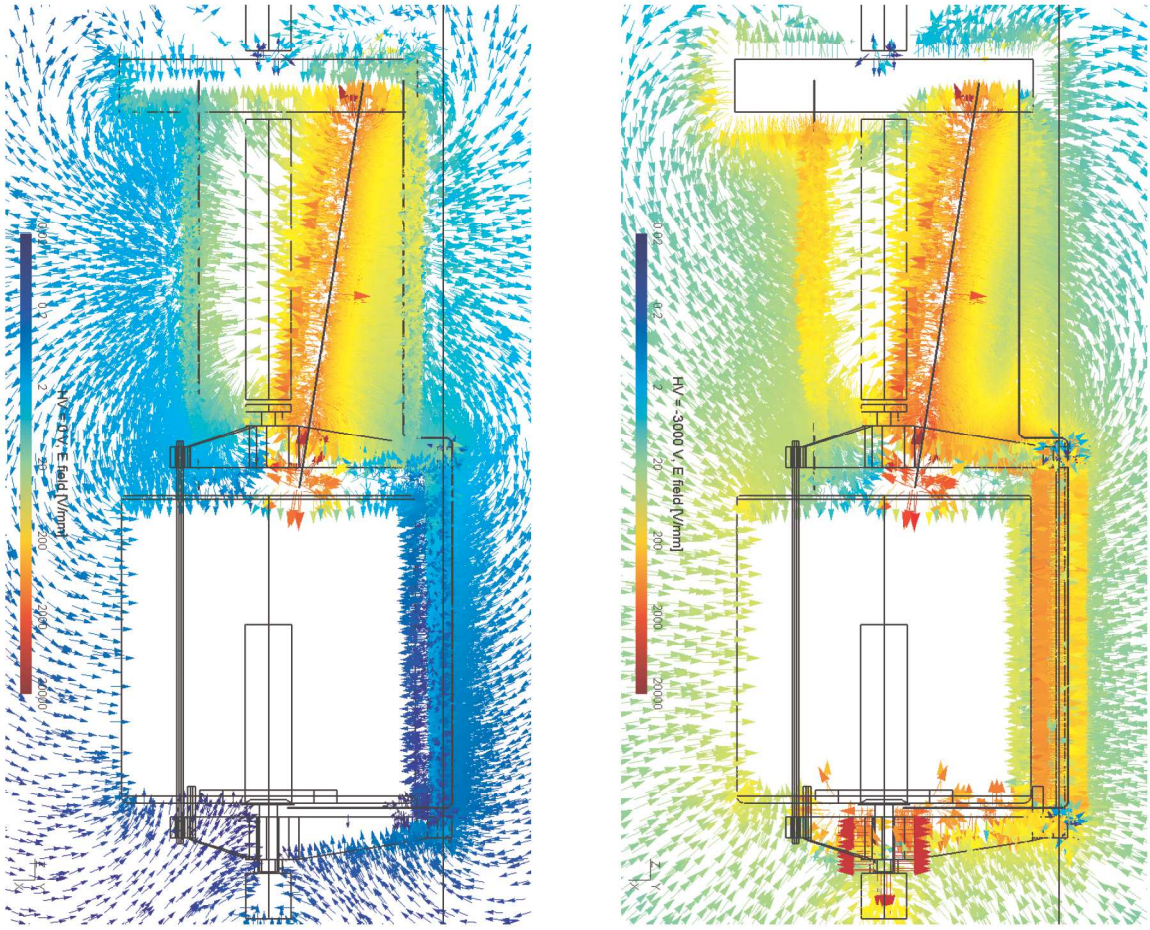

(a) Quasi field–free configuration. **(b)** −3 kV applied to the encapsulation.

Figure 3.12: Shape of the computed electric field in the vicinity of the encapsulated detector. Initially, the detector high voltage bias wire was not fully shielded, thus the configuration with grounded encapsulation is called 'quasi field–free'. Note that in the quasi field–free configuration electric field lines still close on the detector encapsulation.

where it remains until its decay. The numerical procedure was developed to compute the moment of time, at which the ion reaches the geometrical boundary. The time–step length is adjusted accordingly if the intersection occurs before the end of the time–step.

Even though the electric force acts on the cations, there is no need to use symplectic integrators (e.g. Leap–Frog, Forest–Ruth etc.), as a natural choice. Presence of liquid friction yields first–order set of differential equations, where the particle velocity depends proportionally on the electric force. Density of cations of interest is low enough such that the interactions between the charged particles may be neglected.

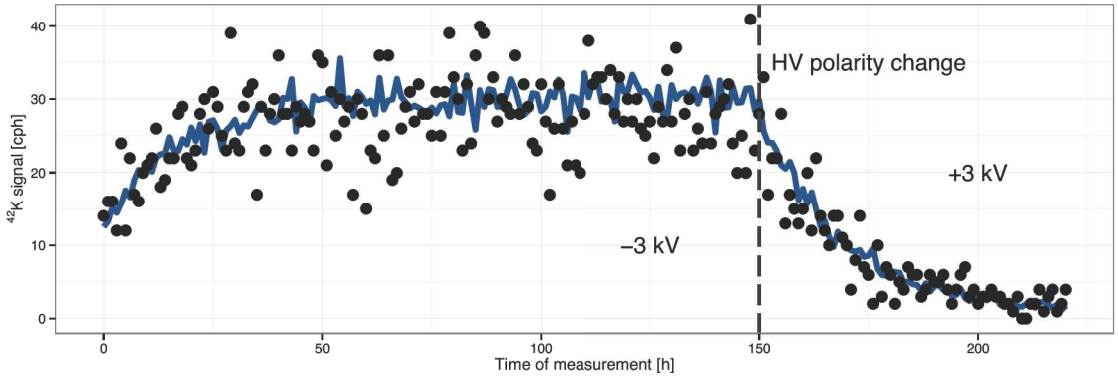

Figure 3.13: ^{42}K signal registered by the GTF–44 detector in 1–hour bins (dots) and the Monte Carlo simulated signal (blue line). The vertical dashed line indicates the moment when the high voltage bias was reversed ($-3\,\mathrm{kV} \rightarrow 3\,\mathrm{kV}$). Growth and decay time constants correspond to the ^{42}K life–time (12.3 h).

Finally, the set of equations implemented in the numerical model is:

$$\dot{\vec{r}} = q\mu\vec{E} + \vec{w} \tag{3.7a}$$

$$\frac{C}{C_0} = \ln\left(1 + \frac{\xi \cdot E}{|\vec{E}|}\right)\frac{|\vec{E}|}{\xi \cdot E} \tag{3.7b}$$

$$[\dot{Y^+}] = -\frac{[Y^+]}{\tau} \tag{3.7c}$$

$$[\dot{N}] = -\ln 2\frac{[N]}{T_{1/2}} \tag{3.7d}$$

$$\mathrm{d}S_{MC} = \varepsilon_{1525}\,(\vec{r}) \tag{3.7e}$$

$$\sigma = \sqrt{6D\mathrm{d}t} \tag{3.7f}$$

where $\vec{r}$ is the charged ($q = 1$) or neutral ($q = 0$) current atom position, μ is the mobility, $\vec{w}$ is the liquid flow velocity. The second equation (3.7b) describes the probability of charged cation production in nuclear decays (see Sec. 2.1.2). The third equation (3.7c) describes the neutralization of cations, and governs the probability of a cation to neutralize with neutralization life–time τ. Similarly, the fourth expression (3.7d) describes the nuclear decay of an atom. $\mathrm{d}S_{MC}$ (3.7e) is the contribution from the decaying atom to the 1525 keV γ–line signal, registered in the Ge detector. Finally, the last equation (Eq. 3.7f) describes the mean diffusion range of an atom in a time step $\mathrm{d}t$. The above set of equations is then solved numerically for a given number of charged and neutral ^{42}K atoms in secular equilibrium (known ^{42}Ar activity).

The simulated experimental time equals at least 5 life–times of ^{42}K (17 h), i.e. 90 h[vii]. In such case the obtained signal, registered by the Ge detector is stable (in secular equilibrium), with statistical error (MC) less than $1/2^5 = 3\,\%$. Also, such long simulation time allows studying the ^{42}K signal in case of high voltage bias changes (transients). As an example, to study the amount of ions deposited on the encapsulation ^{42}K, cations are collected by the negative bias applied to the Ge detector encapsulation. Next, the bias voltage is reversed ($-3\,\mathrm{kV} \rightarrow 3\,\mathrm{kV}$). Nuclear decay of the activity is observed, with the time constant distinctive for ^{42}K (see Fig. 3.13), and the code accurately reproduces the observed signal.

The simulation procedure may be repeated for each physical parameter changed, e.g. the ionic life–time, ion mobility, magnitude and sign of the high voltage bias, dissolved ^{42}Ar activity etc. The algorithm is presented in listing 2. Finally, the Monte Carlo simulation code yields the expected ^{42}K signal S_{MC}, registered by the GTF–44 detector.

[vii] CPU time, the time required to run the simulation for one set of the parameters, is typically 5 h for 4.8 mBq l^{-1} of dissolved ^{42}Ar.

Algorithm 2 $S_{MC}(\xi \cdot E, \tau)$ map generation algorithm, evaluated for each electric field configuration $\vec{E}$.

1: $\mu \leftarrow 0.06\ \mathrm{mm^2\,V^{-1}\,s^{-1}}$ ▷ Fixed mobility
2: $\vec{w} \leftarrow$ Convection field
3: **for all** Electric field configurations $\vec{E}$ **do** ▷ 0 kV, −0.5 kV, ..., −3 kV
4: **for all** $\tau \leftarrow \tau_{min}, \tau_{max}$ **do** ▷ 1 min, ..., 30 min
5: **for all** $\xi \cdot E \leftarrow \xi \cdot E_{min}, \xi \cdot E_{max}$ **do** ▷ 25 V mm^{-1}, ..., 105 V mm^{-1}
6: Calculate $S_{MC}(\mu, \vec{w}, \vec{E}, \tau, \xi \cdot E)$

A two–dimensional field $S_{MC}(\xi \cdot E, \tau)$ was constructed using a simple procedure shown in listing 2. Fig. 3.14 presents the selected results in a graphical form. Each measurement, represented by the signal $S_{exp}(t, HV)$ and its uncertainty, is drawn on the $S_{MC}(\xi \cdot E, \tau)$ plots. Curves $S_{exp} = S_{MC}(\xi \cdot E, \tau)$, shown for each given cumulative time t and high voltage bias HV (Fig. 3.7), are next used to disentangle the value of τ. While both, the ion mobility μ and the charged atom production parameter $\xi \cdot E$, are expected to be constant over other simulation (environmental) parameters, ionic life–time τ depends on the local liquid purity only, and therefore on the cumulative time t of a particular measurement.

Parameter	w/o outlier	w/ outlier
$A/(B-1)$ [ppm] (*fixed*)	2	2
A/B [ppm]	0.23 ± 0.27	0.53 ± 0.23
κ [d^{-1}]	0.084 ± 0.021	0.032 ± 0.015
$\ln 2/\kappa$ [d]	8.3 ± 2.1	22 ± 10
M [min · ppm]	4.8 ± 5.8	14 ± 7
Res. std. error	2.55/6 DOF	6.23/7 DOF

Table 3.4: Impurity concentration model (Eq. 3.4) applied to the computed ion life–time. The constraint for $A/(B-1)$ is derived from the impurity concentration measurement (2 ppm of oxygen equivalent).

When calculating the expected ^{42}K signal, the range of radioactive ions is important, being a product of the mobility μ and the ion life–time τ (and the path integral along the electric field lines, called the 'shape' factor, yielding the volume from which the ions may approach the Ge detector). Thus, the ion mobility μ impacts the computationally determined ion life–time in an obvious way. The product of the two quantities, i.e. $\tau \cdot \mu$, is present entangled throughout the analysis, and for the lower values of the mobility reported before (e.g. $0.02\,\mathrm{mm^2\,V^{-1}\,s^{-1}}$) the estimated τ values would be higher to compensate for the lowered mobility of the ions. For the purpose of the simulations, the fixed ^{42}K mobility of $0.06\,\mathrm{mm^2\,V^{-1}\,s^{-1}}$ is assumed.

Having fixed $\xi \cdot E$, using the value of $40.3\,\mathrm{mm^2\,V^{-1}\,s^{-1}}$ determined in the measurements of ^{222}Rn daughters in liquid nitrogen (see Sec. 2.2.5), it was straightforward to calculate the ion life–time $\tau(t)$ and its uncertainty, as shown in Fig. 3.14a. The value and the uncertainty interval were found as the coordinates of points where the $\xi \cdot E$ (± 1 σ error) lines cross with the parametrized curves $S_{exp} = S_{MC}(\xi \cdot E, \tau)$.

The ion life–time $\tau(t)$ is plotted in Fig. 3.15. Curve (Eq. 3.3 and 3.4)

$$\tau(t) = \frac{M}{[Z^-](t)} = \frac{M}{A}(B - \mathrm{e}^{-\kappa t}) \tag{3.8}$$

was fitted to the data, constrained by the early purity measurement ($\tau(0) = A/(B-1) = 2$ ppm of oxygen equivalent). As it can be seen in the Fig. 3.15, the measurement at 76.16 d (−2 kV) seems to be an outlier. The measurement was preceded by a long positive high voltage bias measurement (1.5 kV for 10.73 d) and ^{228}Th calibration (lasting for 0.93 d), therefore the two fitted curves were plotted and fitting values reported in Tab. 3.4, with and without the outlier point, respectively. A better quality of fit was obtained without the outlier point.

Uncertainty budget Each measurement point indicated in Fig. 3.15 is associated with an uncertainty, of which nearly 21 % comes from the dissolved ^{42}Ar activity estimation, dominating the final results. Another contribution (∼12 %) is due to the uncertainty in $\xi \cdot E$. As it can be seen from the plots in Fig. 3.14, the lower the high voltage bias, the higher is the impact of $\xi \cdot E$ uncertainty on the overall error (slope $\mathrm{d}S_{MC}/\mathrm{d}(\xi \cdot E)$ increases with decreasing high voltage bias). The experimental activity S_{exp} was determined

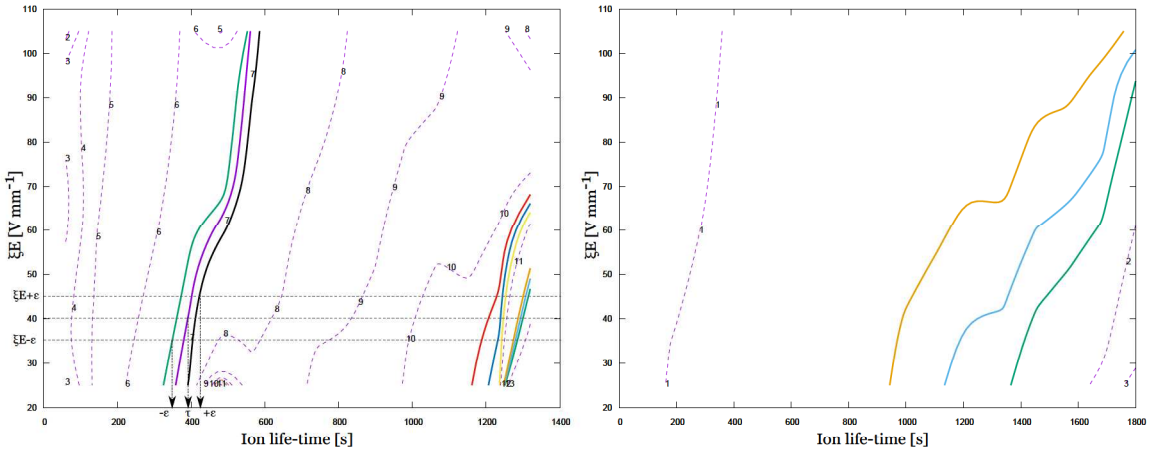

(a) −3 kV, 3 experimental points. **(b)** −0.5 kV, 1 experimental point.

Figure 3.14: Example parametric plots of the expected ^{42}K signal S_{MC} (Monte Carlo) as functions of $\xi \cdot E$ (ion production probability parameter) and τ (ion life–time). Results obtained for −3 kV and 0 kV (semi field–free) are shown as an example. The procedure used to calculate the ion life–time is shown: thick lines indicate the measured signal S_{exp} (in cts h^{-1}, middle line) with error bands (side lines). Dashed horizontal lines indicate $\xi \cdot E$ value, as experimentally determined in Sec. 2.2.5 ($\xi \cdot E = 40.3^{+4.4}_{-5.5}$ V mm^{-1}). The ion life–time τ and the uncertainty interval $[-\varepsilon, +\varepsilon]$ are then determined by finding the crossing points of the curves (see Fig. (a)).

in measurements lasting from 2.82 d to 12.1 d, but typically around 5.5 d, from which the first two days after a change of the bias voltage were always excluded from data (to account for the ^{42}K long life–time). During these rather short periods of time the local purity was not changing significantly, and the overall effect was estimated to be less than 5 %. The only exception was the measurement at −2 kV at the beginning of the measurement campaign (see Fig. 3.15, which lasted over 12 d), but in that case the contribution was estimated to be less than 6 %.

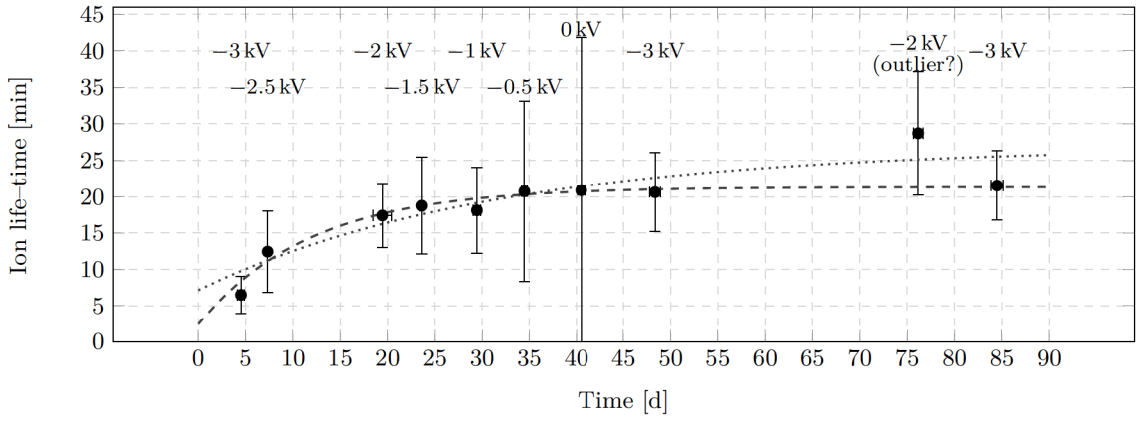

Figure 3.15: The calculated ion life–time τ, as a function of the measurement time. The single result marked as an outlier, was taken right after a measurement at positive high voltage bias (over 10 d), 1.5 kV, also preceded by a calibration run with ^{228}Th source. Error bars include the most dominant uncertainty in the amount of dissolved ^{42}Ar activity.
Limited growth model fitted to the data is plotted, with the outlier excluded (dashed line), and the outlier included (dotted line), respectively. The fit parameters are given in Tab. 3.4.

3.5 Applications to GERDA

Radon emanation from the GERDA cryostat walls enters the liquid and is transported with the convection flows towards the central part of the cryostat. Short Rn diffusion range (tens of cm) does not ensure homogeneous distribution of the inert atoms. In order to keep the radon atoms far from the Ge diodes, a decision was taken by the GERDA collaboration to install the radon shroud [101]. The cylindrical shroud 3 m high, nearly 0.8 m in diameter, closed at the bottom, was made of thin copper foil. Access from the top was ensured for the germanium crystals arranged in strings.

The measurements of ^{42}K cations in LArGe and the data analysis performed in parallel (in the frame of the PhD thesis), were then applied to tackle the problem of the remaining natural radioactivity, coming from ^{42}Ar. In order to further protect Ge detectors from closely decaying ^{42}K, the so–called mini–shrouds (made of copper) were installed around each string of Ge detectors, also closed at the bottom. Electric field generated by a detector was confined to a small volume of a mini–shroud. Electrical separation from the detector holders allowed applying high voltage bias to the mini–shrouds to control the distribution of ^{42}K ions. In different electric configurations the ^{42}K signal was registered in three Ge detectors, assembled into a single string, in order to find the most optimal high voltage bias scheme. Besides the minimization of the ^{42}K signal, the system electronic noise had to be kept possibly low.

Fig. 3.16 depicts the three–dimensional model of the inner–most part of the GERDA detector [102]. It was used to compute the vertical distribution of ^{42}K ions attracted by the mini–shroud, that later allowed to explain the differences in the registered ^{42}K signal between the three Ge detectors, enclosed by the mini–shroud. The model did not require inclusion of the convection due to the fact that volume of liquid argon inside the shroud is mechanically separated from the rest of the cryostat and is considered static. What is more, the heat input from the electronic readout chains is rather low (<0.15 W in total for the three Ge detectors), and the thinness of the shroud (high heat transport) ensures highly uniform temperature of the cryogenic liquid contained inside.

The activity distributed on the mini–shroud side wall was then calculated using the ionic parameters derived in the previous studies in the LArGe facility. The vertical distribution of this activity is shown in Fig. 3.17. The obtained picture clearly explains the higher registered ^{42}K signal in the top and the bottom detectors, while the lowest signal was seen in the middle detector. The amount of deposited ^{42}K activity depends on the amount of electric field lines closing on the mini–shroud surface, mostly on the sharp brink on top or at the bottom edges. Additionally, it was shown in LArGe, that the best noise performance is achieved with the mini–shroud grounded, as there was no improvement from the positive high voltage bias repelling cations. It was both worsening the signal readout quality, and did not significantly lower the ^{42}K signal compared to the case of the grounded mini–shroud.

3.6 Summary

An accurate method of radioactive background assessment was developed, focussed on the studies of signal from ^{42}K ions decaying in liquid argon in the LArGe setup. The model proposed here includes several mechanisms responsible for the overall ionic flux approaching the active volume of the cryostat hosting the high purity germanium detectors.

Due to the presence of the electric field acting instantly on the charged particles, the radioactive ion distribution was altered, and enhancement in the background signal was observed. Thanks to dissolving an additional ^{42}Ar activity it was also possible to observe the long–term behaviour of the ^{42}K ions. These measurements were of great importance to the background assessment, as the most abundant construction material of the GERDA experiment is the liquid argon. Two types of copper–made shrouds were installed in the GERDA cryostat in order to cope with the background induced by ^{222}Rn and ^{42}Ar: the large radon

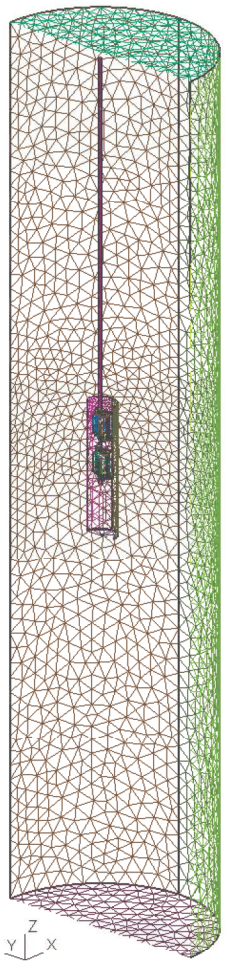

(a) A string of three Ge detectors encapsulated in a mini–shroud. The string is placed inside the radon shroud.

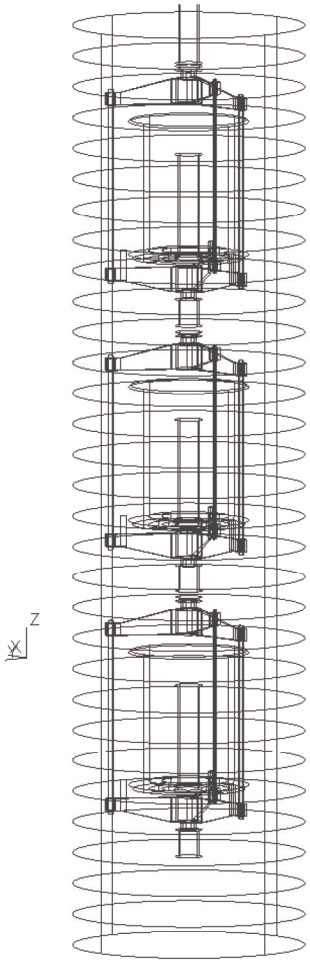

(b) Mini–shroud model close–up. The mini–shroud is divided into 15 mm slices for a detailed analysis of ^{42}K ions vertical distribution.

Figure 3.16: The 3D mesh structure of the radon shroud (3 m high), hosting one string of Ge detectors inside the mini–shroud. The model was used for computation of the expected signal distribution from ^{42}K ions collected on the mini–shroud.

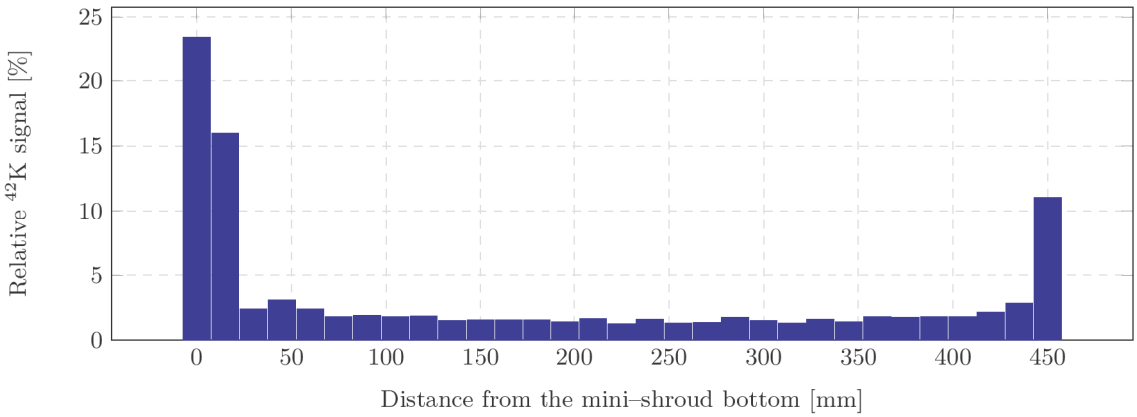

Figure 3.17: Vertical distribution of the collected ^{42}K activity on the surface of the mini–shroud, from the bottom (0 mm — the activity deposited on the bottom lid) to the top (450 mm).

shroud, preventing inert ^{222}Rn atoms from approaching the vicinity of the germanium detector strings due to the convection, and separate mini–shrouds, encapsulating each detector string, as a protection against ^{42}K ions drifted by the electric field.

It is instructive to compare the registered signal in a semi field–free configuration, and when the high voltage bias of $-3\,\mathrm{kV}$ is applied to attract the ions. $4.8\,\mathrm{mBq\,l^{-1}}$ of uniformly distributed ^{42}Ar activity yields the signal under the 1525 keV γ–line of about $12\,\mathrm{cts\,d^{-1}}$. Comparing this value with the measured signal in the quasi field–free configuration one gets between 1.5 and 1.8 enhancement, while for the high voltage bias of $-3\,\mathrm{kV}$ the figures are much higher, i.e. up to 24 times higher signal was registered.

Understanding the time dependence of the ion life–time due to variations of the impurity concentration is also helpful in studies of the natural ^{42}Ar concentration measurements. Introduction of known ^{42}Ar amount into the cryostat was necessary to eliminate the unknown systematic errors (and efficiency) in 1525 keV γ–line observation, used to directly estimate the ^{42}Ar concentration. As the measurements of both natural and enriched argon under the same high voltage bias were not coincident in (cumulative, not absolute) time, their comparison was still vitiated by a systematic error stemming from the varying detection efficiency. Now it is possible to correctly interpolate the values of the ^{42}K signal (of enriched argon) to the coincident times of the natural argon measurements.

The need of extremely low background index justified the need to fully understand the physical processes responsible for the ^{42}K flux reaching the Ge detectors. It also led to the detailed description of the charged radioactive species in cryogenic liquids, that may be generalised for other families of radioactive isotopes, mainly ^{222}Rn, that may be highly relevant to the future ultra–high sensitivity experiments aiming at background index order of $10^{-3}\,\mathrm{cts\,keV^{-1}\,kg^{-1}\,y^{-1}}$.

4

A novel charge sensitive preamplifier proposed for Gerda

The second Phase of the Gerda experiment aims at the background index order of $10^{-3}\,\mathrm{cts\,keV^{-1}\,kg^{-1}\,y^{-1}}$. A significant amount of materials, including highly–radiopure copper and PTFE, were already replaced by intrinsically radio–pure silicon in order to lower the background. Still, one of the major radiation sources close to the Ge detectors is the electronic readout chain (Very Front–End, VFE), especially the feedback resistor of a charge sensitive preamplifier (the VFE electronics in the Phase II is located closer to the detector than in the Phase I) [103]. Options for a custom–made feedback resistor considered were: amorphous germanium, titanium nitride (TiN) thin film resistors, and tungsten (W) on a quartz substrate, and all showed stability problems that needed to be solved (commercially available surface mount resistors are not radio–pure enough).

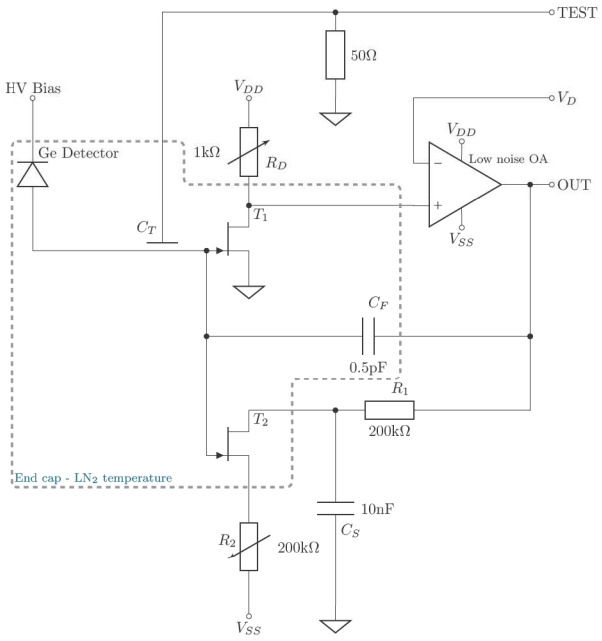

Figure 4.1: Simplified schematics of the resistorless Charge Sensitive Preamplifier. The input transistors are placed close to the detector to minimize noise pick up. C_F closes the high frequency feedback loop, while T_2, C_S and $R_1 \| R_2$ form the DC loop. Other than that, the design uses a classical approach to the CSA construction. V_D controls the operating point of T_1, while R_D controls T_1's drain current.

Readout from the Si–PIN diodes requires a charge sensitive preamplifier (CSA) to condition the faint ionization signal before feeding it to the (shaping) amplifier. Therefore, low capacitance of the detector should be matched by the input capacitance and noise performance of the CSA. In the frame of the PhD thesis a new design of a resistorless CSA was proposed, constructed and tested to work with Ge detectors, replacing the high value feedback resistor with an additional FET transistor, and a second feedback loop, composed of a small value (and thus low intrinsic radioactivity) RC elements. Bare die FET transistors contribute very low to the background, also due to the fact that the bonding technique is used for the electric connections.

The circuit diagram of the invented CSA is shown in Fig. 4.1. Two feedback loops are used to separate the fast and the slow (down to DC) components of the feedback signal. High frequency response is ensured by the feedback capacitor C_F, responsible for integrating the detector current. The operating point of the circuit is governed by the feedback loop composed of the low–pass RC network ($R_1 \| R_2 \cdot C_S$ defining the C_F discharge time constant), R_2 (DC output offset fine adjustment via $R_1 R_2$ voltage divider) and T_2. In the steady state, diode current flows into the T_2 gate (and through R_2, small comparable to the T_2's gate resistance r_G). The second feedback loop is placed in lieu of the classical single resistor feedback.

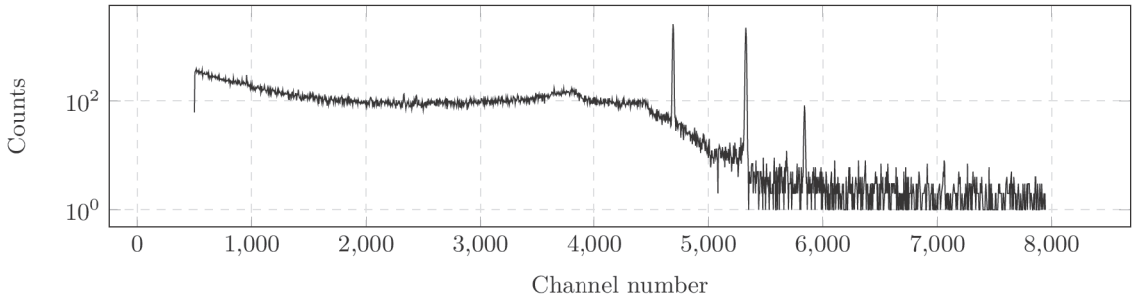

Figure 4.3: ^{60}Co energy spectrum registered with a 10 % germanium detector (DSG GmbH). Bottom threshold of the multi channel analyzer (13 bit ADC, 8192 channels [105]) was set to 500 channels. 1332.5 keV gamma line is used to characterize the amplifier performance (channel 5328), the second gamma line is 1173.2 keV (channel 4692). Two Compton scattering edges from the gamma lines are also present in the spectrum. A prominent local background ^{40}K gamma line is clearly visible (channel 5840).

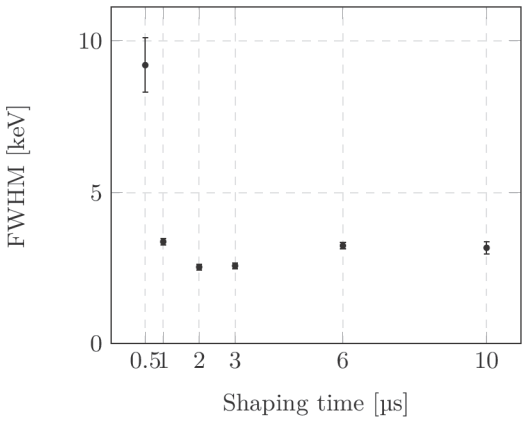

Figure 4.2: FWHM of ^{60}Co 1332.5 keV gamma line as a function of Gaussian shaping time constant. The minimum achieved for 2 µs shaping is 2.32 keV, corresponding to 0.17 % of FWHM. The interesting feature of the presented plot is that the FWHM value exhibits a tendency to improve (value decreases) for increasing shaping times, indicating an existence of a second minimum. This feature may be linked to the presence of the long exponential tail in the output signal.

Two exponential decays were clearly observed in the recorded output of the preamplifier for high energy events. The slow decaying exponent (long tail) caused degradation in the case of high rate of incoming pulses. Height of a piled–up pulse was affected by the base–line shift, thus the result of analogue energy reconstruction (through a shaping amplifier and a multi–channel analyser) was worsened. For a possible solution to the problem see e.g. [104]. However, the modification proposed there, resulting in the increased element count and energy dissipation, may not be acceptable, as the main field of application of the preamplifier is in the very low background experiments. Therefore the average pulse rate is expected not to exceed tens of counts per second, even during the calibrations with external gamma sources. The piled–up events may be easily discarded in both analogue and digital pulse processing paths to improve the energy resolution.

Fig. 4.2 shows the Full Width at Half Maximum (FWHM) of ^{60}Co 1332.5 keV gamma line as a function of the shaping time constant. The minimum resolution of 0.17 % was reached for 2 µs shaping time and a signal cable over 1 m long. The improvement in the energy resolution (FWHM) was achieved in the analogue setup using the Pile–Up Rejection (PUR) circuitry. The average pulse rate with the ^{60}Co source used was 160 cps without PUR, and 120 cps with PUR (i.e. 25 % less). Fig. 4.3 and Fig. 4.4 show the registered ^{60}Co energy spectrum and a zoom to the gamma lines of the ^{60}Co source, respectively.

The long–term temperature stability of the amplifier was also studied. The stability of the ^{60}Co 1332.5 keV gamma peak position is shown in Fig. 4.5, expressed as a relative shift from the average peak position. Temperature of the warm part of the electronics was recorded in parallel, and is plotted along with the peak position variation.

In the near future, further tests are foreseen to investigate the system's performance in cryogenic conditions, as in the current setup the operational amplifier and the second feedback loop components were mounted outside the cryostat (except for the pair of FETs). Tests including double FET transistors (e.g. J620, LSK489 and LSK389) should reveal the most optimal configuration. It is expected that the system noise

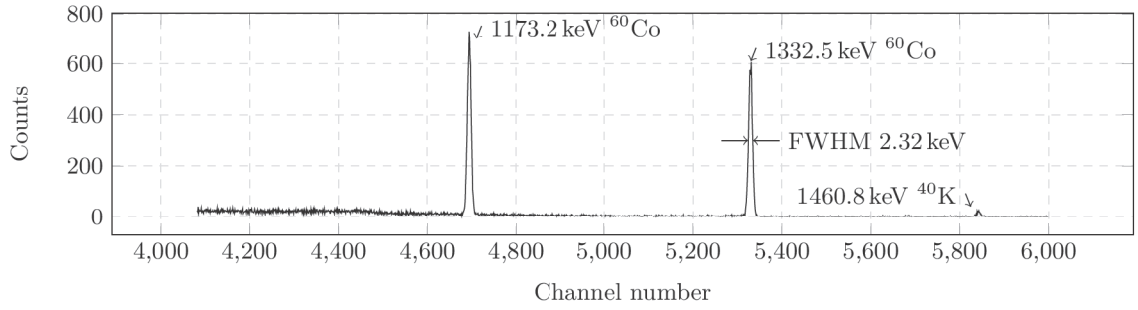

Figure 4.4: Upper part of the ^{60}Co energy spectrum registered with a 10 % germanium detector.

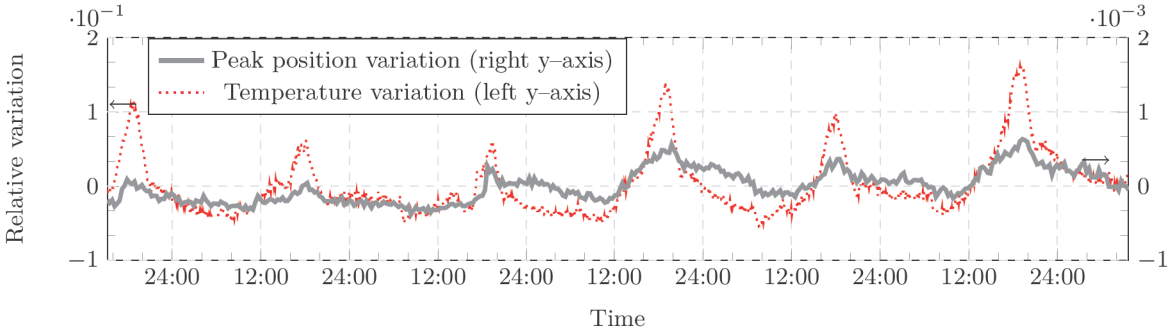

Figure 4.5: Relative ^{60}Co 1332.5 keV gamma peak position (thick gray) versus temperature (dotted red) registered in the laboratory conditions. The temperature change was in the range of 22.0 °C to 27.6 °C during six days of continuous data taking. Temperature coefficient of the energy stability was estimated as better than 0.4 % °C^{-1}, including the Ortec 672 shaping amplifier (temperature coefficient < 0.005 % °C^{-1}) and the Tukan 8k multichannel analyzer (unknown temperature coefficient). In the foreseen applications of the preamplifier, the setup will be operated in the cryogenic liquid environment, ensuring more stable temperature conditions.

improves, reducing further the FWHM of the registered energy spectra. The new design was also filed at the Polish Patent Office (applicant's file reference PZ/3228/PCT/RW).

5

The online radon monitor for the DarkSide Experiment

The internal radioactive contamination of the DarkSide–50 detector has to be addressed in a peculiar way. ^{222}Rn progenies, as heavy metals, may easily plate–out on various surfaces being in contact with air, especially during the assembly of the TPC. Alpha decays occurring on or just under the surfaces being in direct contact with the active argon volume, are a possible source of background for the search of WIMPs (both the recoiled nuclei and the α–particles with degraded energy). Therefore the assembly of the DarkSide detectors was held in ^{222}Rn–free clean rooms (Clean Room 1, CR1, where the assembly of the DarkSide–50 LAr–TPC took place, and Hanoi Cleaning Room, CRH, giving a direct access to the muon and neutron vetoes), to which the ^{222}Rn–free air was supplied from a dedicated radon abatement system. Equipment interfacing directly to the detector was also located in the clean rooms. It was also clear that the ^{222}Rn activity in air needs to be monitored at each stage of the experiment's construction and operation.

In order to reduce the background from ^{222}Rn daughters plating–out, it was mandatory to use ^{222}Rn–suppressed air ($< 1\,\mathrm{mBq\,m^{-3}}$), supplying the two ultra–clean rooms during the construction (e.g. the cleaning and preparation of the LAr–TPC parts) and the maintenance of the DarkSide–50 detector. Therefore instant monitoring of the radioactive contamination of the air was necessary. As a part of the PhD, the ^{222}Rn monitor was created in a close cooperation with University of Massachusetts, Amherst, and Princeton University. The detector's design goal was to achieve the sensitivity on the order of $1\,\mathrm{mBq\,m^{-3}}$, be able to perform real–time measurements, with air, argon and nitrogen. Its detection principle was based on the electrostatic collection of the ionized ^{222}Rn daughters. The detection limit depends on the active volume (400 l) and the electric field shape. Its low internal background was achieved by the application of clean construction materials, like copper, Teflon and stainless steel (known for their low ^{222}Rn emanation rates). The internal surfaces were electropolished (further limiting emanation), the vessel was built with a minimum welding length, and the connections and joints were metal–sealed. Micro–discharges had to be avoided (the goal to work with voltages $< 20\,\mathrm{kV}$) independently of the supplied gas type. A round (also to avoid the discharges), low–background and large–surface alpha detector was chosen to register the decays of ^{222}Rn and its daughters.

A detailed study of the ion drifting in the gas vessel was performed. The shape of the detector (including the diameters of the gas inlets, position of the alpha–particle detector, curvature of the welding points) was optimized for the design goals and technical limitations, such as the allowed inner pressure and the wall thickness. Fig. 5.1 depicts the results of a 3D E–filed computation for 8 kV applied to the chamber. Fig. 5.2 presents the results of ^{222}Rn daughter drift calculation. The study showed that the drift time is very short, i.e. less than 2 s. Majority of the particles (over 90 %) reaches the detector's active surface (Ortec Ultra–AS diode, operated at very low potential, 40 V), while only a small fraction ends on the detector's housing. Very high ion collection efficiency (ε_{col}) was thus expected.

The detector was installed in Hall C of the LNGS underground laboratory. Despite the drift chamber being enclosed in the protective metal box, analogue signal path was susceptible to the external sources of noise. The electronic noise may come from the high power electric equipment installed in Hall C (lighting, 20 t cranes, the radon abatement system, the air conditioning system), or residual micro–discharges, occurring in the vessel. Both sources of the noise produce bipolar pulses, that pass the shaping amplifier. The pulses consist of a leading negative undershoot, followed by a fine–shaped positive part. The positive part of

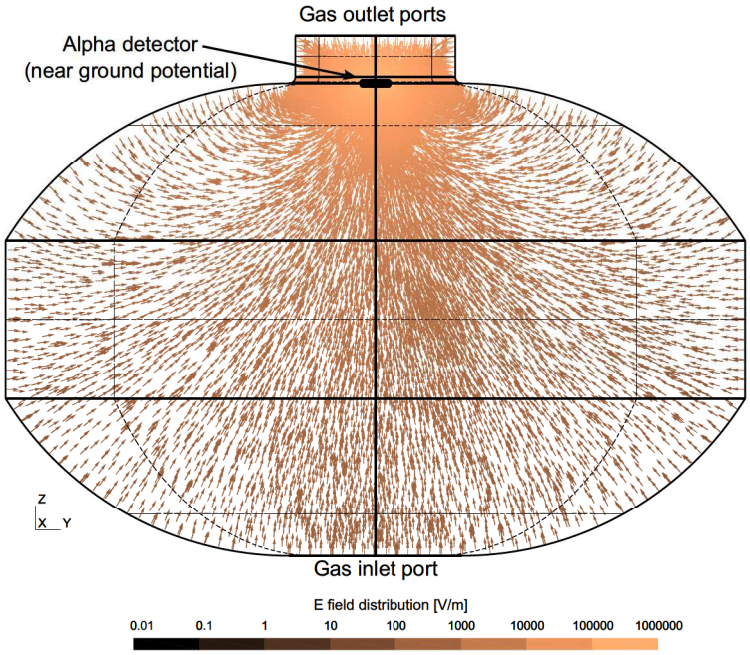

Figure 5.1: Calculation of the E–field lines inside the radon detector. Majority of the lines close on the Ortec diode yielding high collection efficiency of the charged radon daughters. Breakdown voltage of various gases is not reached anywhere in the detector volume (for air it is $3\,\mathrm{MV\,m^{-1}}$, nitrogen $3.45\,\mathrm{MV\,m^{-1}}$ and argon $0.6\,\mathrm{MV\,m^{-1}}$).

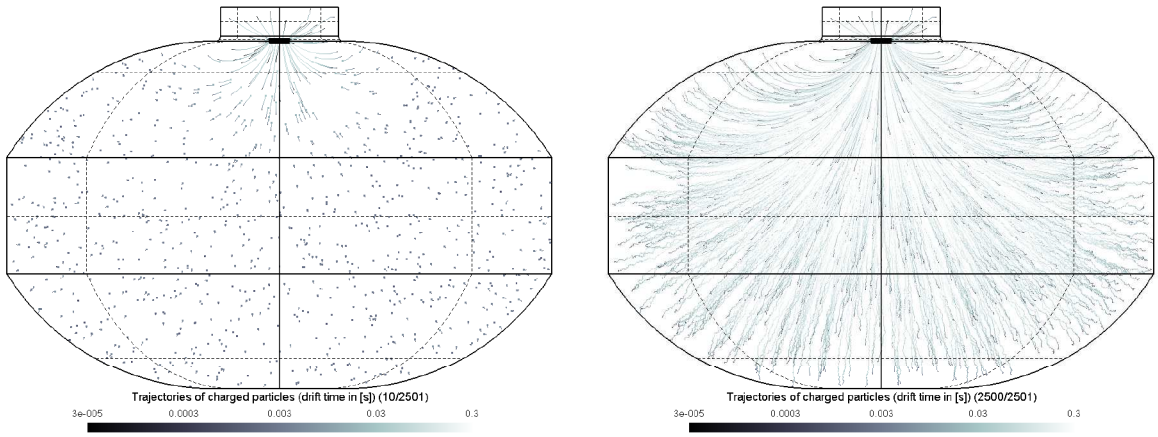

Figure 5.2: Visualization of ^{214}Po trajectories, modelled for the DarkSide online radon monitor. Typical ion drift time to the surface of the alpha detector (located on top) is below 2 s. The detector is thus capable of measuring ^{220}Rn activity. Particle diffusion is included in the computation. In overall, the geometrical collection efficiency, as the function of the electric field shape, is estimated to reach almost 95 %.

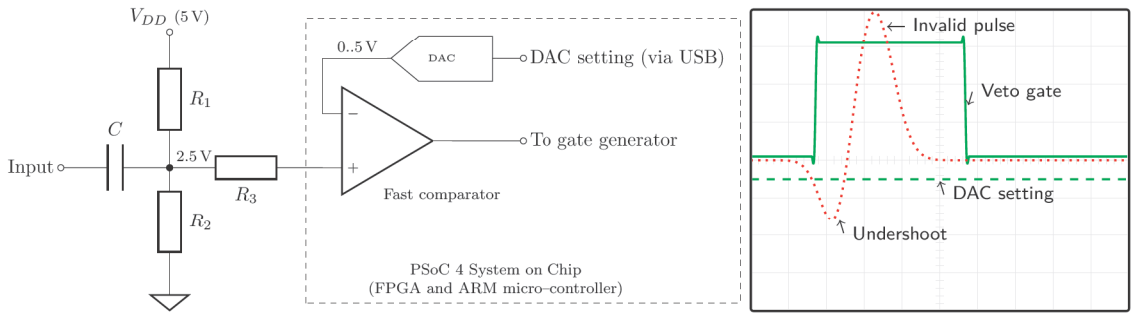

Figure 5.3: Working principle of the electronic noise veto. Electronic pulses generated by the noise pick–up in the very front end (Si–PIN detector, preamplifier) are usually preceded by a negative edge. FPGA–based veto circuit produces the gate pulse of a programmable length. The gate is used to veto the multi channel analyser to reject invalid pulses. Otherwise positive part of the pulse may be falsely interpreted as valid signal, increasing background index in the registered energy spectrum and, in consequence, lowering the sensitivity. The circuit is based on a highly versatile System on Chip (SoC) microcontroller PSoC 4 from Cypress. The chip contains ARM processor, simple FPGA structure and several analogue peripherals.

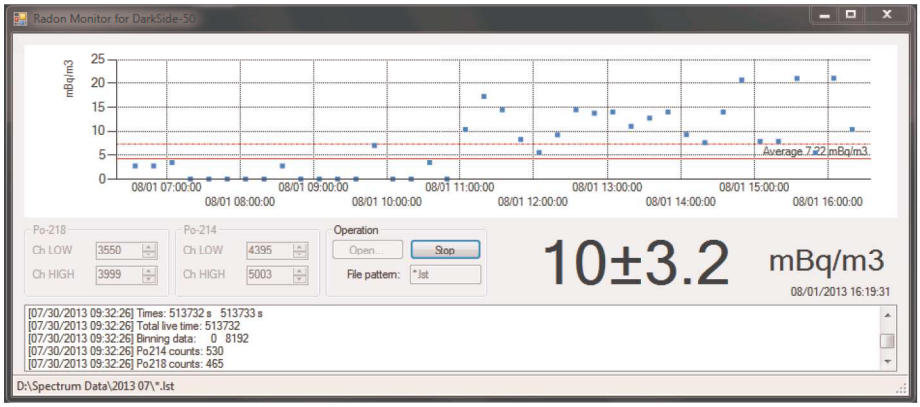

Figure 5.4: Slow control system interface with online ^{222}Rn content readout during the ^{222}Rn detector calibration campaign.

the pulses is then registered by the multi–channel analyser (MCA) as valid and contributes to the system background in the energy range of α–particles of interest.

Fig. 5.3 shows the design and a typical response of a dedicated noise–suppression circuitry, elaborated for the detector. The idea behind the circuit is to detect the leading negative edge of the pulse, and to generate a veto gate for the MCA inhibit input. The gate length is programmable in a wide range to suit different MCA inhibit input requirements, the response time to the undershoot is below 10 ns. Normally, ground referenced noise pulses exhibit a negative undershoot, which is hard to process in a single supply digital system (PSoC 4, Cypress, consisting of an ARM processor, several peripherals like a digital–to–analogue converter, and a simple FPGA). The input circuitry consists of a passive DC–level shifter ($CR_1 \| R_2$), shifting the baseline to $V_{DD}/2$ for $R_1 = R_2$ at the input of a comparator. R_3 is required to limit the current for high energy events as the comparator inputs are under– and over–voltage protected via Schottky diodes (present in the internal structure). The comparator output is generating a programmable–length inhibit gate in the built–in FPGA. Negative undershoot threshold level may now be referenced to $V_{DD}/2$, set by the DAC. Therefore, the entire circuit may be supplied from a single supply line (USB interface, also used for programming). The circuitry proved to be over 99 % effective in rejecting false pulses, while being easy to implement and operate (flexible in the threshold setting and the inhibit gate generation).

The system parameters (gas pressure and flow readout, high voltage control, noise level) are monitored by a

Parameter	Value	Remarks
Detection efficiency ε	$36 \pm 3\,\%$	Absolute detection efficiency measured for the radon suppressed air for ^{218}Po and ^{214}Po
Background B	6.4 ± 0.5 cts d^{-1}	for ^{218}Po in detector vessel
Internal ^{222}Rn emanation of the detector A_{sat}	0.72 ± 0.10 mBq	Saturation value
Detection limit	0.7 mBq m^{-3}	At 90 % C.L.

Table 5.1: Selected parameters of the DarkSide online radon monitor.

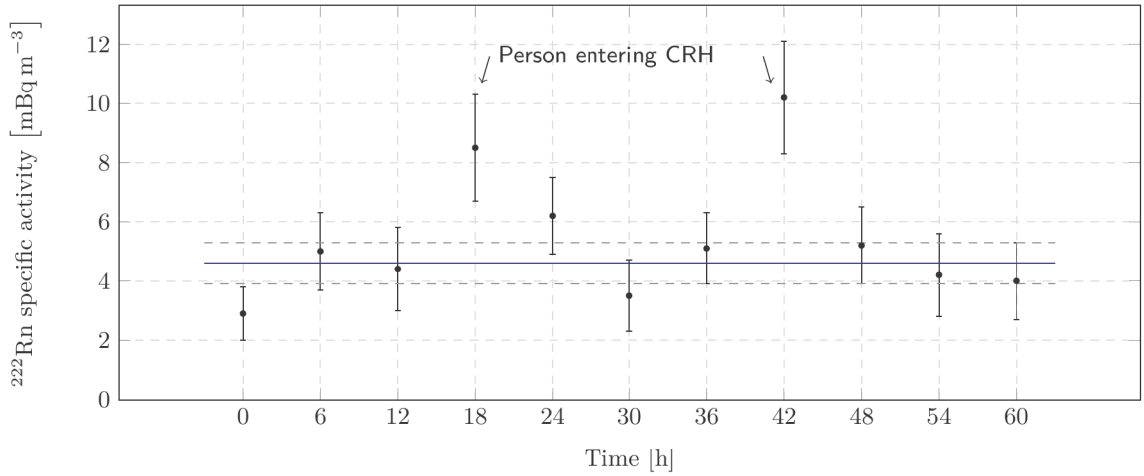

Figure 5.5: An example of ^{222}Rn content in the CRH clean room measured over the weekend of 09.11.2013 — 11.11.2013. The two highest values indicated were recorded after a person entered the clean room for a short time for maintenance work. The ^{222}Rn content, averaged over the period indicated, is (4.6 ± 0.6) mBq m^{-3}.

fully automated slow control system (with remote access). Analysis of the data collected with the MCA is performed on–line. The ^{222}Rn concentration is calculated from the ^{218}Po and ^{214}Po peaks (Fig. 5.4). The absolute detection efficiency of the system ε for both ^{218}Po and ^{214}Po reached $36 \pm 3\,\%$. In general, ε contains the collection efficiency ε_{col} of ions on the active surface of the alpha detector, and the detection efficiency (ε_{det}, probability to register an alpha decay of an ion sitting on the detector surface). Since one could assume that $\varepsilon_{det} \approx 50\,\%$, $\varepsilon_{col} = 72\,\%$, the result close to the estimated value.

Careful design and construction of the system allowed reaching the minimum measurable specific activity of 0.7 mBq m^{-3}. Though the detector was exposed to harsh environment of Hall C, active noise suppression system, designed and implemented in the data acquisition path, ensured stable operation of the whole setup. Tab. 5.1 summarizes the most important parameters of the detector, as measured during it's operation in LNGS.

Tab. 5.2 presents the most important results obtained for the DarkSide–50 clean rooms using the radon monitor. They showed that the DarkSide–50 radon abatement system reduces the radon content in the air by more than four orders of magnitude, down to a single mBq m^{-3}. Air samples from clean rooms CRH and CR1 showed about 10 mBq m^{-3} (on average) and 200 mBq m^{-3}, respectively. The measured ^{222}Rn concentrations come from the internal emanation of the rooms, and CR1 exhibits a higher value because the volume of the room is much bigger, for which the flushing with ^{222}Rn–free air is less efficient.

As an example, ^{222}Rn content in the CRH clean room was monitored over the weekend of 09.11.2013 — 11.11.2013, as shown in Fig. 5.5. The ^{222}Rn concentration was calculated every 6 h. Two sampled measurements were clearly higher than the rest of the data points. They correspond to the periods when a

Sample	^{222}Rn content [mBq m^{-3}]	Remarks
Ateko air	15 ± 2	Samples taken directly from the abatement system in July 2013
Ateko air	1.4 ± 0.4	November 2013
CRH air	from 5.8 ± 0.9 to 21 ± 3	Various periods between July and November 2013
CR1 air	208 ± 21	November 2013
Hall C air	≈ 50000	Measured with Alpha Guard

Table 5.2: Measured ^{222}Rn concentration in different air samples.

person entered the clean room (for about 1 h) for maintenance of the cryogenic systems. Excluding these two measurements the obtained average was (4.6 ± 0.6) mBq m^{-3} (the result indicated by the horizontal lines). Such an accurate measurements allowed optimization of the clean room usage (e.g. to estimate the maximum allowed number of people entering the room). Measurements of the air from the clean rooms proved them to have the lowest ^{222}Rn concentrations ever achieved, comparable with small clean benches flushed with pure nitrogen gas. Such a low ^{222}Rn concentration in clean rooms was necessary to avoid contamination of the most sensitive parts of the DarkSide–50 detector.

6

Summary

The irreducible neutrino flux will constitute the ultimate background of the ultra–sensitive dark matter experiments. Neutrino–electron scattering, registered in the low–energy electronic recoils, will yield signal at the level of 10 – 25 $\mathrm{cts\,t^{-1}\,y^{-1}}$. In the case of the searches for neutrinoless double beta decays, the background index at $Q_{\beta\beta}$ on the order of $10^{-4}\,\mathrm{cts\,kg^{-1}\,keV^{-1}\,y^{-1}}$ is required to explore the normal neutrino mass hierarchy. In order to reach these background levels, all other internal sources of the background must be mitigated one by one. If the current trend of increasing experimental sensitivity, improving roughly by an order of magnitude every two–to–three years, is to be maintained, the expected background sources have to be reduced at the same rate. Cryogenic liquids, allowing for high–purity, large mass, and scalable design, have to be characterized for the internal contamination, considering also the ionic aspects presented in this work. Ultra–pure cryogenic liquids unavoidably aid to preserve the charge of atoms, acquired during the nuclear decays. Long neutralization life–time of the cations leads to their pre–concentration in the vicinity of the detector's active volume, where the electric field is usually employed in the detection process.

This thesis presented the experimental results from the two related topics within the field of ultra–low background experiments, searching for rare events: the role of radioactive ion transport (two families) in cryogenic liquids, contributing to the experimental background, and the highly sensitive method of ^{222}Rn concentration measurements in pure gases. Along with the experimental efforts, the interpretation of the acquired data and the applications were presented. A possible solution to the problem of a low–radioactivity charge sensitive preamplifier for germanium detectors was also described.

It was shown that ^{222}Rn progenies, when in liquid nitrogen, exhibit ionic life–times on the order of 1 min. As the purity of the used liquid was low, the life–time of cations in high–purity cryogenic liquids was expected to extend, as it was later shown in the case of ^{42}K ions in liquid argon. Another interesting property of time–dependent ionic flux was first described qualitatively in the thesis (as in the case of ^{222}Rn daughters), and then quantitatively for ^{42}K in liquid argon. A detailed numerical model was proposed, including numerous aspects of the ionic flux, ranging from the birth of ions in different types of nuclear decays, throughout their transport in cryogenic liquids under electric fields, diffusion and thermal convection, to bulk neutralization and nuclear decays, finally yielding a significant signal in the detector. The model, in the form of a computer program, was used to describe the temporal changes of the registered ^{42}K flux in the LArGe setup (in the framework of Gerda). It was also used for the monitor, being extensively used in the DarkSide experiment. ^{42}K background studies in Gerda and the design and construction of a very efficient and versatile online radon

In the future, the knowledge gained during the experimental and analytical work presented here, may be used to further improve the design of ultra–low background experiments, including the assessment of the far–reaching background sources from ^{42}Ar, ^{222}Rn and ^{220}Rn in cryogenic liquids.

Bibliography

[1] K.–H. Ackermann et al., "The Gerda experiment for the search of $0\nu\beta\beta$ decay in ^{76}Ge," *Eur. Phys. J. C*, vol. 73, no. 3, 2013.

[2] C. E. Aalseth et al., "The DarkSide Multiton Detector for the Direct Dark Matter Search," *Adv. in High En. Phys.*, no. 541362, 2015.

[3] M. Agostini et al., "LArGe – Active background suppression using argon scintillation for the GERDA $0\nu\beta\beta$-experiment," *arXiv*, vol. 1501.05762, 2015.

[4] C. L. Cowan et al., "Detection of the free neutrino: A confirmation," *Science*, vol. 124, p. 103, 1956.

[5] C. S. Wu et al., "Experimental Test of Parity Conservation in Beta Decay," *Phys. Rev.*, vol. 105, pp. 1413–1414, 1957.

[6] M. Goldhaber et al., "Helicity of Neutrinos," *Phys. Rev.*, vol. 109, pp. 1015–1017, 1958.

[7] G. Danby et al., "Observation of High-Energy Neutrino Reactions and the Existence of Two Kinds of Neutrinos," *Phys. Rev. Lett.*, vol. 9, pp. 36–44, 1962.

[8] K. Kodama et al., "Observation of tau–neutrino interactions," *Phys. Lett.*, vol. B504, pp. 218–224, 2001.

[9] ALEPH, DELPHI, L3, OPAL, and SLD Collaborations, and LEP Electroweak Working Group, and SLD Electroweak Group, and SLD Heavy Flavour Group, "Precision Electroweak Measurements on the Z Resonance," *Phys. Rep.*, vol. 427, no. 257, 2006.

[10] S. L. Glashow, "Partial Symmetries of Weak Interactions," *Nucl. Phys.*, vol. 22, pp. 579–588, 1961.

[11] A. Salam and J. C. Ward, "Electromagnetic and weak interactions," *Phys. Lett.*, vol. 13, pp. 168–171, 1964.

[12] S. Weinberg, "A Model of Leptons," *Phys. Rev. Lett.*, vol. 19, pp. 1264–1266, 1967.

[13] F. J. Hasert et al., "Observation of Neutrino Like Interactions Without Muon or Electron in the Gargamelle Neutrino Experiment," *Phys. Lett.*, vol. B46, pp. 138–140, 1973.

[14] R. Davies, D. Harmer, and K. Hoffman, "Search for neutrinos from the Sun," *Phys. Rev. Lett.*, vol. 20, pp. 1205–1209, 1968.

[15] K. Hirata et al., "Real time, directional measurement of B-8 solar neutrinos in the Kamiokande-II detector," *Phys. Rev. D*, vol. 44, pp. 2241–2260, 1991.

[16] D. Abdurashitov et al., "The Russian–American gallium experiment (SAGE) Cr neutrino source measurement," *Phys. Rev. Lett.*, vol. 77, pp. 4708–4711, 1996.

[17] W. Hampel et al., "GALLEX solar neutrino observations: Results for GALLEX IV," *Phys. Lett.*, vol. B447, pp. 127–133, 1999.

[18] S. M. Bilenky, "Neutrino oscillations: brief history and present status," *arXiv*, vol. 1408.2864 [hep-ph], 2014.

[19] D. V. Forero, M. Tortola, and J. W. F. Valle, "Neutrino oscillations refitted," *Phys. Rev. D*, vol. 90, no. 9, p. 093006, 2014.

[20] X. Qian and W. Wang, "Reactor neutrino experiments: θ_{13} and beyond," *Mod. Phys. Lett.*, vol. A29, p. 1430016, 2014.

[21] G. Branco, R. G. Felipe, and F. Joaquim, "Leptonic CP Violation," *Rev. Mod. Phys.*, vol. 84, pp. 515–565, 2012.

[22] F. T. Avignone, S. R. Elliott, and J. Engel, "Double Beta Decay, Majorana Neutrinos, and Neutrino Mass," *Rev.Mod.Phys.*, vol. 80, pp. 481–516, 2008.

[23] C. Weinheimer and K. Zuber, "Neutrino masses," *Ann. der Phys.*, vol. 525, no. 8-9, pp. 565–575, 2013.

[24] T. Lasserre, "Light Sterile Neutrinos in Particle Physics: Experimental Status," *arXiv*, vol. 1404.7352 [hep-ex], 2014.

[25] A. de Gouvea, P. Vogel, "Lepton Flavor and Number Conservation, and Physics Beyond the Standard Model," *Prog. Part. Nucl. Phys.*, vol. 71, pp. 75–92, 2013.

[26] R. N. Cahn et al., "White Paper: Measuring the Neutrino Mass Hierarchy," *arXiv*, vol. 1307.5487 [hep-ex], 2013.

[27] B. Pritychenko, "Systematics of evaluated half-lives of double-beta decay," *Nucl. Data Sheets*, vol. 120, pp. 102–105, 2014.

[28] M. Agostini et al., "Results on Neutrinoless Double-β Decay of ^{76}Ge from Phase I of the GERDA Experiment," *Phys. Rev. Lett.*, vol. 111, p. 122503, 2013.

[29] H. V. Klapdor-Kleingrothaus, I. V. Krivosheina, and O. Chkvorets, "Search for neutrinoless double-beta decay with enriched ^{76}Ge in Gran Sasso 1990 - 2003," *Physics Letters B*, vol. 586, pp. 198–212, 2004.

[30] C. E. Aalseth et al., "The IGEX experiment revisited: A Response to the critique of Klapdor-Kleingrothaus, Dietz and Krivosheina," *Phys. Rev. D*, vol. 70, p. 078302, 2004.

[31] B. Schwingenheuer, "Status and prospects of searches for neutrinoless double beta decay," *Ann. der Phys.*, vol. 525, pp. 269–280, 2013.

[32] R. G. H. Robertson, "Empirical Survey of Neutrinoless Double Beta Decay Matrix Elements," *Mod. Phys. Lett. A*, vol. 28, p. 1350021, 2013.

[33] J. Barea, J. Kotila, and F. Iachello, "Nuclear matrix elements for double-beta decay," *Phys. Rev. C*, vol. 87, p. 014315, 2013.

[34] W. Maneschg, A. Merle and W. Rodejohann, "Statistical Analysis of future Neutrino Mass Experiments including Neutrino-less Double Beta Decay," *arXiv*, vol. 0812.0479v1, 2008.

[35] H.V. Klapdor-Kleingrothaus et al., "Latest results from the Heidelberg-Moscow double beta decay experiment," *Eur. Phys. J. A*, vol. 12, pp. 147–154, 2001.

[36] H. V. Klapdor-Kleingrothaus and I. V. Krivosheina, "The evidence for the observation of 0nu beta beta decay: The identification of 0nu beta beta events from the full spectra," *Mod. Phys. Lett. A*, vol. 21, pp. 1547–1566, 2006.

[37] S. Abe et al., "Production of Radioactive Isotopes through Cosmic Muon Spallation in KamLAND," *Phys. Rev. C*, vol. 81, p. 025807, 2010.

[38] A. Gando et al., "Limit on Neutrinoless $\beta\beta$ Decay of Xe-136 from the First Phase of KamLAND-Zen and Comparison with the Positive Claim in Ge-76," *Phys. Rev. Lett.*, vol. 110, no. 6, p. 062502, 2013.

[39] A. Shimizu, "Results from KamLAND-Zen," *XXVI Conference on Neutrino Physics and Astrophysics*, 2014.

[40] B. Berger, "KamLAND-Zen: Results, Status, and Prospects," *Presentation at CIPANP – Vail, Colorado*, May 21, 2015.

[41] M. Auger et al., "Search for Neutrinoless Double-Beta Decay in ^{136}Xe with EXO-200," *Phys. Rev. Lett.*, vol. 109, p. 032505, 2012.

[42] J. B. Albert et al., "Search for Majorana neutrinos with the first two years of EXO-200 data," *Nature*, vol. 510, p. 229–234, 2014.

[43] K. Alfonso et al., "Search for Neutrinoless Double-Beta Decay of ^{130}Te with CUORE-0," *Phys. Rev. Lett.*, vol. 115, p. 102502, Sep 2015.

[44] C. Bucci, "The CUORE and CUORE-0 experiments," *TAUP 2015, http://taup2015.to.infn.it/*, 20 Sep 2015.

[45] D. R. Artusa et al., "Searching for neutrinoless double-beta decay of ^{130}Te with CUORE," *arXiv*, vol. 1402.6072 [physics.ins-det], 2014.

[46] I. Ogawa et al., "Study of Ca-48 double beta decay by CANDLES," *J. Phys. Conf. Ser.*, vol. 375, p. 042018, 2012.

[47] J. Boger et al., "The Sudbury neutrino observatory," *Nucl. Instrum. Meth. A*, vol. 449, pp. 172–207, 2000.

[48] N. Abgrall et al., "The MAJORANA DEMONSTRATOR Neutrinoless Double-Beta Decay Experiment," *Adv. in H. En. Phys.*, vol. 2014, 2014.

[49] M. Green, "Current Status of The Majorana Demonstrator," *TAUP 2015, http://taup2015.to.infn.it/*, 20 Sep 2015.

[50] R. Arnold et al., "Probing New Physics Models of Neutrinoless Double Beta Decay with SuperNEMO," *Eur. Phys. J. C*, vol. 70, pp. 927–943, 2010.

[51] R. Arnold et al., "Technical design and performance of the NEMO 3 detector," *Nucl. Instrum. Meth. A*, vol. 536, pp. 79–122, 2005.

[52] A. Garfagnini, "Neutrinoless Double Beta Decay Experiments," *arXiv*, vol. 1408.2455 [hep-ex], 2014.

[53] L. Pandola, "Status of double beta decay experiments using isotopes other than ^{136}Xe," *Phys. Dark Univ.*, vol. 4, pp. 17–22, 2014.

[54] C. Giunti and M. Laveder, *http://www.nu.to.infn.it/*. 20 Sep 2015.

[55] M. Laubenstein and G. Heusser, "Cosmogenic radionuclides in metals as indicator for sea level exposure history," *Appl. Rad. and Isot.*, vol. 67, no. 5, pp. 750–754, 2009.

[56] M. Agostini et al., "The background in the $0\nu\beta\beta$ experiment Gerda," *Eur. Phys. J. C*, vol. 74, no. 2764, 2014.

[57] O. Chkvorets, "Search for double beta decay with HPGe detectors at the Gran Sasso underground laboratory," *arXiv*, vol. 0812.1206, 2008.

[58] F. Zwicky, "Die Rotverschiebung von extragalaktischen Nebeln," *Helv. Phys. Acta*, vol. 6, pp. 110–127, 1933.

[59] E. Corbelli and P. Salucci, "The extended rotation curve and the dark matter halo of M33," *arXiv*, vol. astro-ph/9909252, 2000.

[60] V. C. Rubin and W. K. Ford, "Rotation of the Andromeda Nebula from a spectroscopic survey of emission regions," *Astrophys. J.*, vol. 159, pp. 379–403, 1970.

[61] J. F. Navarro, C. S. Frenk, and S. D. M. White, "The structure of cold dark matter halos," *Astrophys. J.*, vol. 462, p. 563, 1996.

[62] NASA/CXC/M. Weiss, *Chandra X-Ray Observatory, 1E 0657-56.*

[63] D. N. Spergel et al., "First-year Wilkinson Microwave Anisotropy Probe (WMAP) observations: cosmological parameter results," *Astrophys. J. Suppl. Ser.*, vol. 1488, pp. 175–194, 2003.

[64] M. Tagmark et al., "Cosmological parameters from SDSS and WMAP," *Phys. Rev. D*, vol. 69, no. 103501, 2004.

[65] P. A. R. Ade et al., "Planck early results," *Astr. & Astrophys.*, vol. 536, no. A1, 2011.

[66] M. Smith et al., "The RAVE survey: constraining the local Galactic escape speed," *Month. Not. of the R. Astron. Soc.*, vol. 379, pp. 755–772, 2007.

[67] R. Bernabei et al., "Final model independent result of DAMA/LIBRA - phase 1," *Eur. Phys. J. C*, vol. 73, no. 2648, 2013.

[68] P. Agnes et al., "First results from the DarkSide-50 dark matter experiment at Laboratori Nazionali del Gran Sasso," *Phys. Lett. B*, vol. 743, pp. 456–466, 2015.

[69] E. Aprile et al., "Dark Matter Results from 225 Live Days of XENON100 Data," *Phys. Rev. Lett.*, vol. 109, p. 181301, 2012.

[70] D. S. Akrieb et al., "First results from the LUX dark matter experiment at the Sanford Underground Research Facility," *Phys. Rev. Lett.*, vol. 112, p. 091303, 2014.

[71] W. E. Schmidt, K. E. Volykhin, A. G. Khrapak, and E. Illenberger, "Structure and mobility of positive and negative ions in non-polar liquids," *J. Electrostat.*, vol. 47, pp. 83–95, 1999.

[72] S. C. Jeng, W. M. Fairbank Jr, and M. Miyajima, "Measurements of the mobility of alkaline earth ions in liquid xenon," *J. of Phys. D*, vol. 42, no. 3, p. 035302, 2009.

[73] K. Wamba et. al., "Mobility of thorium ions in liquid xenon," *Nucl. Instr. and Meth. in Phys. Res. A*, vol. 555, pp. 205–210, 2005.

[74] H. T. Davis, S. A. Rice, and L. Meyer, "On the Kinetic Theory of Simple Dense Fluids.," *J. of Chem. Phys.*, vol. 37, p. 947–956, 1962.

[75] T. H. Dey and T. J. Lewis, "Ion mobility and liquid motion in liquefied argon," *J. of Phys. D*, vol. 1, 1968.

[76] A. J. Walters and L. W. Mitchell, "Mobility and lifetime of 208-tl ions in liquid xenon," *J. of Phys. D*, vol. 36, no. 11, p. 1323, 2003.

[77] J. Lekner, "Motion of electrons in liquid argon," *Phys. Rev.*, vol. 158, pp. 130–137, 1967.

[78] B. Baibussinov et. al, "Free electron lifetime achievements in Liquid Argon Imaging TPC," *J. of Instr.*, vol. 5, p. 03005, 2010.

[79] T. GERDA Collaboration, "GERDA - The GERmanium Detector Array for the search of neutrinoless $\beta\beta$ decays of ^{76}Ge at LNGS. `http://www.mpi-hd.mpg.de/gerda/public`," 2004.

[80] V. Ashitkov et al., "Liquid argon ionization detector for double beta decay studies," *arXiv*, vol. nucl-ex/0309001, 2003.

[81] K. Pelczar et al., "Behaviour of ^{222}Rn and its daughters in liquid nitrogen," *GERDA Collaboration Meeting*, 2008.

[82] M. Wójcik and G. Zuzel, "Low–^{222}Rn nitrogen gas generator for ultra–low background counting systems," *Nucl. Instrum. Meth. A*, vol. 539, no. 1–2, pp. 427 – 432, 2005.

[83] J. Thomas and D. Imel, "Recombination of electron-ion pairs in liquid argon and liquid xenon," *Phys. Rev. A*, vol. 36, 1987.

[84] I. Lefkowitz, K. Kramer, M. A. Shields, and G. L. Pollack, "Dielectric and Optical Properties of Crystalline Argon," *J. of Appl. Phys.*, vol. 38, pp. 4867–4873, 1967.

[85] L. Moral and A. F. Pacheco, "Algebraic approach to the radioactive decay equations," *Am. J. of Phys.*, vol. 71, pp. 684–686, 2003.

[86] N. Frodyma, private communication.

[87] C. Geuzaine and J.-F. Remacle, "Gmsh: a three-dimensional finite element mesh generator with built-in pre- and post-processing facilities," *Int. J. for Num. Meth. in Eng.*, vol. 79, no. 11, pp. 1309–1331, 2009.

[88] P. Dular, C. Geuzaine, F. Henrotte, and W. Legros, "A general environment for the treatment of discrete problems and its application to the finite element method," *IEEE Trans. on Magn.*, vol. 34, no. 5, pp. 3395–3398, 1998.

[89] S. Pommé and B. C. Marroyo, "Improved peak shape fitting in alpha spectra," *Appl. Rad. and Isot.*, vol. 96, pp. 148–153, 2015.

[90] N. Frodyma, K. Pelczar*, and M. Wójcik, "Observation and modeling of ^{222}Rn daughters in liquid nitrogen," *Nucl. Instr. Meth. A*, vol. 744, pp. 21–29, 2014.

[91] K. Pelczar, "New slow control for LArGe," *GERDA Collaboration Meeting*, 2011.

[92] K. Pelczar, "Update to LArGe SC," *GERDA Collaboration Meeting*, 2012.

[93] A. S. Barabash, V. N. Kornoukhov, and V. E. Jants, "Estimate of the Ar-42 content in the earth's atmosphere," *Nucl. Instr. Meth. A*, vol. 385, pp. 530–534, 1997.

[94] D. Budjas, J. Janicsko, G. Korschinek, M. Laubenstein, K. Pelczar, S. Schönert, M. Wójcik, G. Zuzel, "Production of ^{42}Ar for high intensity ^{42}K background studies with LArGe," Gerda *Scientific/Technical Report*, vol. GSTR-12-011.

[95] M. Agostini, D. Budjas, C. Cattadori, A. Gangapshev, K. Gusev, M. Heisel, M. Junker, A. Klimenko, A. Lubashevsky, A. Machado, K. Pelczar, S. Schönert, A. Smolnikov and G. Zuzel, "Determination of the ^{42}Ar specific activity in argon by using the LArGe facility," Gerda *Scientific/Technical Report*, vol. GSTR-12-018.

[96] K. Pelczar et al., "Modelling of 42K behaviour in LArGe," *GERDA Collaboration Meeting*, 2011.

[97] OpenCFD Ltd., *http://www.openfoam.org/*. 21 Jul 2014.

[98] CAMPOS ASE, *https://wiki.fysik.dtu.dk/ase/*. 22 Apr 2015.

[99] A. Bettini et. al., "A study of the factors affecting the electron life time in ultra–pure liquid argon," *Nucl. Instr. Meth. A*, vol. 305, pp. 177–186, 1991.

[100] B. L. Henson, "Mobility of Positive Ions in Liquefied Argon and Nitrogen," *Phys. Rev.*, vol. 135, pp. A1002–A1008, 1964.

[101] L. Pandola, K. T. Knoepfle, S. Schoenert, B. Schwingenheuer, "Background from radon emanation in the GERDA cryostat," Gerda *Scientific/Technical Report*, vol. GSTR-09-001.

[102] K. Pelczar et al., "K42 drift calculations coupled with MaGe," *GERDA Collaboration Meeting*, 2012.

[103] C. M. Cattadori, "Selected Topics on FE Electronics for the GERDA Phase II Ge detector readout," *LRT 2015 – Low Radioactivity Techniques Workshop V, Seattle, WA, USA*, 18-20 Mar 2015.

[104] A. Fazzi and P. Rehak, "Performance of an X–ray spectroscopic system based on a double–gate double–feedback charge preamplifier," *Nucl. Instr. and Meth. in Phys. Res. A*, vol. 439, pp. 391–402, 2000.

[105] Z. Guzik, S. Borsuk, K. Traczyk, and M. Plominski, "TUKAN – An 8K pulse height analyzer and multi-channel scaler with a PCI or a USB interface," *IEEE Trans. on Nucl. Sci.*, vol. 53, 2006.